Magnetic Avalanches in Mn_{12}-acetate, "Magnetic Deflagration"

by

Yoko Suzuki

A dissertation submitted to the Graduate Faculty in Physics in partial fulfillment of the requirements for the degree of Doctor of Philosophy, The City University of New York.

2007

ProQuest Information and Learning Company
300 North Zeeb Road
P.O. Box 1346
Ann Arbor, MI 48106-1346

This manuscript has been read and accepted for the Graduate Faculty in Physics in satisfaction of the dissertation requirement for the degree of Doctor of Philosophy.

Date	Prof. Myriam P. Sarachik Chair of Examining Committee
Date	Executive Officer

Prof. Joseph L. Birman

Prof. Eugene M. Chudnovsky

Prof. Frederick W. Smith

Prof. Sergey Vitkalov

Supervisory Committee

THE CITY UNIVERSITY OF NEW YORK

Abstract

Magnetic Avalanches in Mn_{12}-acetate,

"Magnetic Deflagration"

by

Yoko Suzuki

Thesis Advisor: Distinguished Professor Myriam P. Sarachik

Mn_{12}-acetate, first synthesized in 1980 by Lis, is one example of a class of many molecules called single molecule magnets (SMMs) or molecular nanomagnets. These molecules have several atomic spins strongly coupled together within each molecule. They exhibit interesting quantum mechanical phenomena at low temperatures such as quantum tunneling of magnetization, which was first found with Mn_{12}-acetate in 1996 by Friedman, *et al.*, and Berry phase oscillations which were measured in Fe_8 (another SMM) in 1999 by Wernsdorfer, *et al.* In addition to possible application as memory storage and qubits for quantum computers, these systems provide the means for studies of mesoscopic physics as well as the interactions of the molecules with their environment, such as phonon, photon, nuclear spin, intermolecular dipole, and exchange interactions.

Mn_{12}-acetate has twelve Mn ions magnetically coupled in the center of the molecule yielding a giant spin of $S = 10$ at low temperature. It also has a large uniaxial anisotropy of 65 K. Below 3 K, magnetization curves show strong hysteresis due to the anisotropy barrier. At thesis temperatures, the spin relaxes through the barrier by quantum tunneling of magnetization, which produces regularly-spaced multiple resonant steps in the hysteresis curve. Magnetic avalanches, first detected by Paulsen *et al.*, also occur for some samples only at low temperature, leading to a very fast single-step reversal of the full magnetization, which clearly differs from

relaxation by tunneling.

In this thesis, I present the results of detailed experimental studies of two aspects of magnetic avalanche phenomenon: "conditions for the triggering of avalanches" and "propagation of the avalanche front". In the first study, we find the magnetic fields at which avalanches occur are stochastically distributed in a particular range of fields. For the second study, we conducted local time-resolved measurements. The results indicate the magnetization avalanches spread as a narrow interface that propagate through the crystal at a constant velocity which is roughly two orders of magnitude smaller than the speed of sound in solids. We argue this phenomenon is closely analogous to the propagation of a flame front (deflagration) through a flammable chemical substance.

DEDICATION
To the loving memory of
my mother-in-law,
Rosmarie E. O'Connor

Acknowledgments

First, I would like to thank my advisor, Myriam Sarachik for giving me this opportunity and experience which changed my life! She has been a great role model for me as a researcher and a woman. I would never have come this far without her. I am very thankful for her time and patience, and for the freedom which she also gave to me so that I could grow as an independent researcher.

I would also like to thank Eugene Chudnovsky for his constant theoretical support. He has been very generous spending time for discussions and sharing his ideas with us. His knowledge and insight guided us to obtain meaningful data which he linked to physical models. His enthusiasm of research is contagious and encouraged us to obtain more results. I also had a great time attending the nano-magnetism workshop which he and Javier Tejada organized at Coma-Ruga. I would like to thank them for that too. Dimitri Garanin also gave theoretical support for us. His ability and focus for various complicated physical parameters were phenomenal and enabled us to analyze our data. I also would like to thank Carles Calero Borrallo, a student of Eugene for his support and friendship. Jonathan Friedman is a former student of my advisor and is the ultimate good-example as a graduate student and a researcher for me and other students at CUNY. Jonathan is now a faculty at Amherst College, and there I had the honer to work in collaboration with him and Mustafa Bal. I learned a great deal from them and I am grateful for that.

I have always had a great time working in the Sarachik group, and I appreciate every member of the group who made it possible for me to have a lot of fun, learn new things and produce results at the same time. Sergey Vitkalov gave me training when I started to work in the group. He is now a faculty at CCNY. Through all the time, he has always been a great source of advice and help. His student, Jingqiao Zhang has also been very helpful. YiCheng Zhong and Heirong Zheng also gave me training in the beginning. I had a lot of fun working with Yejun Yang and Islam Hoxha. I am grateful for David Graybill who completed many difficult and cumbersome tasks for the lab. Ricardo Gonzalez Rubio, Yeekin Tsui, Kurt James and Ashik Idrisy all were very helpful. I admire Sean McHugh for always coming up with new ideas. I am thankful for Reem Jaafar for her friendship. I hope that everybody will have even more successful future.

I have been lucky to have many good collaborations at the Sarachik group. I am grateful for all the people who gave us support. Especially I would like to thank Hakan Altan for helping us with the optical setting. I am also very grateful for his friendship. Jiufeng Tu, Laszlo Mihaly and Larry Carr were very helpful for the experiment at the Brookhaven National Laboratory. The group of Eli Zeldov at the Weizmann Institute of Science provided us Hall sensors. I would like to thank him and the members of his group, Nurit Avraham, Yuri Myasoedov and Hadas Shtrikman for their great support. Nurit also worked at CCNY as a visiting student. I would like to thank her and Ady Stern for their collaborating work. I am also grateful to David Hendrickson at University of Calfolnia, San Diego and George Christou at University of Florida, Gainesville for providing the samples for us. I would like to thank Evan Rumberger, a student of David Hendrickson, who actually grew the samples and Nicole Chakov, a student of George Christou, who grew many beautiful samples for us and had many nice correspondences with me.

I would like to thank Russ Hinchliff and Linden Langhorne of the Machine Shop for their skilled and quick jobs of building many parts of equipment for us. I would also like to thank H. Feng Du of the Electronic Shop for his help. The people in Prof. Gunner's lab were very helpful and lent us some tools. I would like to thank Vladimir Petricevic for letting us borrow many digital scopes from the department. Sue Turner, Joan Meekins and Aiping Gao have been very helpful in the physics office of CCNY. Allida Gupton was helpful at the physics office of the Graduate Center. Douglas Ewing and other crews at the international student office of the Graduate Center have been giving me caring support which has kept me in legal visa status. I also would like to thank the security guards and janitors at CCNY, who said hello to me in the lab practically every late night, for their work of giving me protection and a clean environment.

I have taken many great physics courses at City College and the Graduate Center of CUNY. The knowledge I learned from them gave me the basis to grow as a researcher. I am very grateful for all the lecturers. I would like to thank Bonji Sakita for his classical mechanics course. I never had chance to thank him in person. V. Parameswaran Nair taught me many great lectures of quantum mechanics and field theory. I would like to thank Melvin Lax for his math course. I still often look at the E&M lecture notes of Timothy Boyer. Many students also have asked me for a copy. Later, I found statistical mechanics taught by Harold Falk really useful for my research. I am very

thankful for Joseph Birman for his group theory and advanced solid state physics lectures, and he also helped my preparation for the second qualifying exam when I was feeling unconfident. Frederick Smith gave great lectures of solid state physics, and he also gave me many good advices for the second qualifying exam. I am very grateful for Viraht Sahni for teaching me density-functional theory. Quantum theory of solids lectures given by Godfrey Gumbs were very interesting. Micha Tomkiewicz patiently taught me, a computer-simulation beginner, to the point of actually using it on research all the time. I also would like to thank Sultan Catto for constructing better and clear rules for the first qualifying examination. Victor Chung and Juan Pajuelo were very supportive when I worked as a TA.

I would like to thank everybody in the field of *Single Molecule Magnets*. I have met many great people in conferences. I learned so much from their work through the conversation, their presentations and papers. I feel very attached to it and feel very sad to leave this field. I hope I will have some connection to it in the future.

I am very grateful for National Science Foundation for its funding which covered the expense for research, my tuition and stipend. I appreciate its generous policy of accepting many foreign students and U.S. tax payers who actually provide the money.

I would also like to thank the members of my thesis committee, Joseph Birman, Eugene Chudnovsky, Frederick Smith and Sergey Vitkalov for agreeing to be on the committee and taking the time to read my thesis.

I would like to thank Demetrios Kalamidas and Dharanjit Singh for being great company while studying or chatting with me in J403 (the dirty graduate student study room) during the first two years of graduate school. Gelu Comanescu was a very faithful lunch buddy with me while he was at CCNY. Neo Valentin is a talented (amateur) motivational speaker who successfully helped me overcome fear before my departmental colloquium talk. I also would like to thank Anita Yan and Mila Susnjar for being supportive roommates.

My parents, Norio and Kyoko suzuki have always been supporting me from Japan financially and emotionally out of most selfless love and respect toward me. In spite of several years of my complete absence from them, they have always believed in me and never questioned my decisions, and at the same time they would always tell me, “You have done enough. Just come back home!” Natsuko Suzuki is my beautiful

little sister and the other half of my soul. She has been always supportive and worried about me more than her own illness. I truly wish, hope and pray that she will get better soon. My older brother, Hideya Suzuki, who is a chemist, gave me the idea of what graduate work is like; however I did not really live in the lab like he did. Most importantly I would like to thank Kotomi Suzuki, my sister-in-law for marring Hideya. My other brother, Fumihiko Suzuki was willing to come to New York from Japan as a nanny, if I become pregnant, so that I could complete my graduate work without any problem. It did not happen, but I am very thankful for his will, and I might count on that in the future. I also would like to thank my new family in Massachusetts, Rosmarie, Terry, Frank, Patti, Andrew, Luke, Leah, Melissa, Kim, Jill, Tina, Jason, Anne, Walter and more. They have been very supportive.

Lastly and mostly, I would like to thank my husband, Kevin Mertes. He was a senior student when I started working in the lab. I have learned a great deal from him including a nice attitude toward coworkers and a humble attitude toward research. Professionally and personally, he has been always supportive. Most importantly for me and most painfully for him, he has been always there to listen to me getting my ideas and crazy speculations, or frustrations and complaints out of my otherwise-cannot-function mind. Thank you!

Table of Contents

List of Figures

1 Introduction

During the past two decades, the field of single molecule magnets (SMMs) [1, 2], has grown dramatically within chemistry and physics; and extensive research has led to many wonderful discoveries in fundamental studies of physics together with the possibility of applications for new technology. The first SMM, Mn_{12}-acetate was synthesized in 1980 by Lis [3]. However, it did not received much attention until its unique magnetic properties were measured in the early 1990's by Caneschi, *et al.* [4], Sessoli, *et al.* [5, 6]. While there are now hundreds of different compounds of SMMs that have been synthesized over years by chemists (a few examples are Fe_8 [7,8], Mn_3 [9], Mn_4 [10,11], Mn_6 [12], Mn-[3×3] [13–15], $[Mn_{18}]^{2+}$ [16], Mn_{30} [17], $[Mn_4]_2$ dimer [18], V_{15} [19, 20], Ni_4 [21–23], Mo_{154} [24], Mo_{176} [25], Fe_{30} [26, 27] and Mn_{84} [28, 29]), Mn_{12}-acetate still remains the most studied SMM to date.

SMMs have several atomic spins strongly coupled together, within each molecule, yielding a total spin that is larger than the electronic spin but small enough [30–33] to exhibit quantum mechanical phenomena. In a typical SMM, each molecule consists of hundreds of atoms and ions, and the magnetic cluster in the middle is surrounded by non-magnetic solvents. As a result, the distance between magnetic clusters is large, and each tiny (nano-)magnet acts more-or-less independently. Avogadro's number of identical molecules are contained in a single crystal, and measuring the response generated by the entire crystal provides ample signal strength. Since the molecules are identical and independent of each other, we are still probing the behavior of the individual molecular spins; and by measuring many of them at once, we obtain the probability distribution for the behavior of an individual spin. (It is equivalent to measuring one molecule Avogadro number of times). At low temperature, quantum tunneling of magnetization was observed with Mn_{12}-acetate by Fried man, *et al.* in 1996 [34–36] and later in other SMMs [8, 10, 16, 20, 37]. Berry phase oscillations were

observed with Fe_8 the other prototypical SMM by Wernsdorfer, *et al.* in 1999 [38,39]. The molecules are in solid form and interact with their environment (such as phonon, photon, hyperfine, intermolecular dipolar and exchange interactions) [30,31,33,40–50]. The interactions with the spin and its decoherence process are also very interesting subjects to study in SMMs.

Many measurements and studies have been made on SMMs (review articles, [51–56]), especially Mn_{12}-acetate [57–61] and Fe_8 [62–66]. The magnetic properties have been measured in different conditions at different temperatures and magnetic fields. Inelastic neutron scattering [67–70], HF-EPR [71–75], MNR [76–83], μ-SR [84, 85], magnetic circular dichroism measurements [86–88] and many optical measurements [89–95] have netted a precise description of these materials. Many successful theoretical [42, 96–104] and computational [105–109] studies have led to a better understanding of the behavior of SMMs. The field has been fueled by chemists who have persistently created new SMMs with made-to-order symmetries and cluster-spin sizes [110], as well as crystals with fewer defects [111–113]. One of the aims is to create SMMs with larger anisotropy energies to improve the possibility of using them for memory storage. Also there has been tremendous effort to deposit or fabricate two-dimensional arrays of these molecules without losing their magnetic properties [114–118] in order to explore the possibility of using them for memory storage and/or as qubits in quantum computing [119, 120]. The most recent studies were focused on population manipulation of the spin states by electromagnetic radiation [121–125].

In this thesis, I will describe detailed measurements of one of the interesting and possibly unique properties of SMMs, namely magnetic avalanches [126,127]. The thesis is organized in the following way: The basic properties of Mn_{12}-acetate are described in Section 2. Section 3 presents the detailed experimental results, and proposes and discusses a simple theoretical interpretation in terms of magnetic "de-

flagration". In Section 4, some of experimental techniques used for the measurements are shown. And finally in Section 5, a summary of the research and a list of conclusion of the experimental results are presented along with some suggestions for future research.

2 Mn_{12}-acetate

2.1 Chemical Structure and Spin Hamiltonian

Mn_{12}-acetate is the most studied SMM (the other is Fe_8). Its chemical formula is given by: $[Mn_{12}O_{12}(CH_3COO)_{16}(H_2O)_4]\cdot 2CH_3COOH\cdot 4H_2O$. The magnetic properties derive from twelve Mn ions that are located near the center of the molecule. As shown in Fig. 1 the magnetic core consists of eight Mn^{3+} ($S = 2$) ions located on an outer ring that surrounds four inner Mn^{4+} ($S = 3/2$) ions symmetrically arranged on the corners of a cubane. The four inner Mn ions couple antiferromagnetically via superexchange through oxygen bridges to the eight outer Mn ions. As determined by ac-susceptibility measurements [4, 6, 71] and EPR measurements [4, 6, 72–74], the molecule has an $S = (8 \times 2) - (4 \times 3/2) = 10$ ground state. The molecular symmetry gives the molecules its large anisotropy. The net result is that the SMM, Mn_{12}-acetate, acts like a giant $S = 10$ spin particle with large uniaxial anisotropy of 65 K forming a double well potential (see Fig. 2).

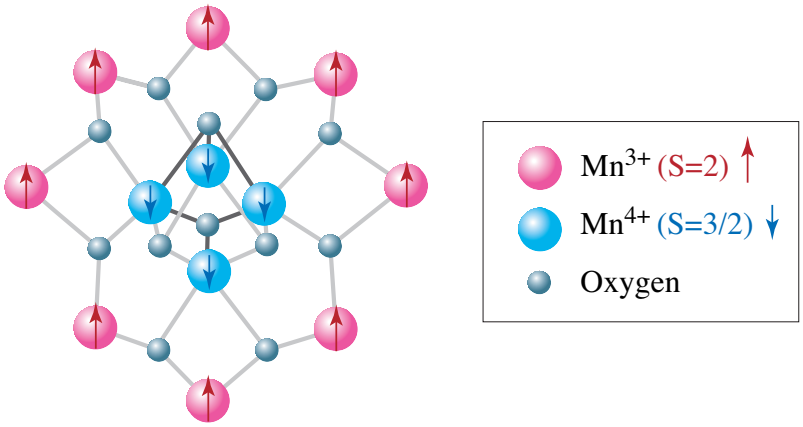

Figure 1: The magnetic core of the $S = 10$ ground state in Mn_{12}-acetate. The four inner Mn ions couple anti-ferromagnetically via superexchange through oxygen bridges to the eight outer Mn ions.

The crystalline form of Mn_{12}-acetate has a tetragonal body centered lattice with lattice spacings of $a = b = 17.3$ Å and $c = 12.1$ Å [3]. The inter-molecule distance

is sufficiently large in the crystalline form of Mn_{12}-acetate so that the exchange interaction is negligible [5, 128] and the dipole field due to a neighboring molecule is rather small ($\approx 0.01\,\mathrm{T} - 0.05\,\mathrm{T}$) [5, 128, 129]. This means that each molecule acts nearly independently and the entire crystal can be considered an ensemble of weakly interacting, nearly identical $S = 10$ spin particles. X-ray diffraction measurements have determined that Mn_{12}-acetate has $I\bar{4}$ (S_4) space group symmetry [3].

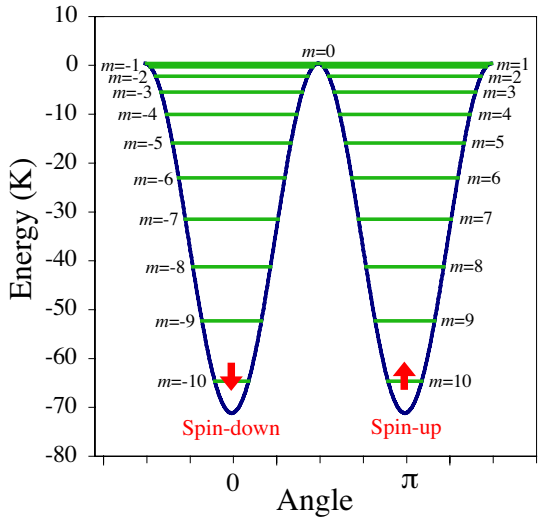

Figure 2: The 21-energy levels for $S = 10$ were calculated for $\mu_0 H = 0\,\mathrm{T}$ and $\hat{V}_T = 0$ using Eq. 1. Due to the uniaxial anisotropy turms, it forms a double well potential with the energy barrier of 65 K. Therefore, at low temperate, the spin orients either up or down along z-axis.

Neutron scattering experiments [67–69] as well EPR measurements [72, 73] have determined Mn_{12}-acetate can be modeled by the effective spin-Hamiltonian:

$$\hat{\mathcal{H}} = -D\hat{S}_z^2 - A\hat{S}_z^4 - g_z\mu_B H_z \hat{S}_z + \hat{V}_T\,, \tag{1}$$

where $D = 0.5477\,\mathrm{K}$ is the second order anisotropy constant, $A = 1.173 \times 10^{-3}\,\mathrm{K}$ is the fourth order anisotropy constant and $g_z \approx 1.94$ is the g-factor. The last term, $\hat{V}_T$, is the symmetry breaking term. $\hat{V}_T$ may include terms such as transverse field, $g_x\mu_B H_x$, fourth order transverse anisotropy, $C(\hat{S}_+^4 + \hat{S}_-^4)$, or other terms. Second order transverse anisotropy, $E(\hat{S}_x^2 - \hat{S}_y^2)$ is forbidden by the tetragonal symmetry for

perfect Mn_{12}-acetate crystals. However, it was found that due to solvent disorder [130] and other defects [131, 132], there is a distributed (not single valued) second order transverse anisotropy, and also that this is the main symmetry breaking that drives the tunneling process in Mn_{12}-acetate [133–135].

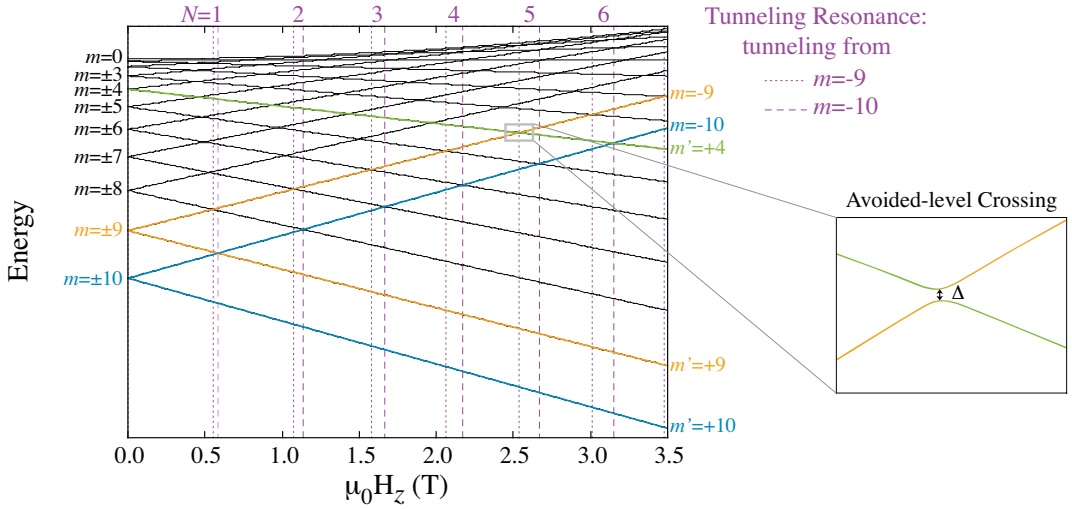

Figure 3: Energy eigenvalues for Eq. 1 (which includes the presence of a small symmetry breaking term, $\hat{V}_T = g_x \mu_B H_x \hat{S}_x$) determined by numerically diagonalizing the Hamiltonian. The presence of the symmetry-breaking term means the eigenvalues do not cross. The inset shows a close-up view of one of the crossings appearing in the rectangle. Δ also can be calculated by the high order perturbation theory for small $\hat{V}_T$.

In Fig. 3, the dependence of the 21-energy levels on $\mu_0 H_z$ during magnetic field sweep along z-axis. At $\mu_0 H_z = 0\,\mathrm{T}$, the degenerate levels split as $\mu_0 H_z$ increases due to the Zeeman interaction. Eq. 1 with small $\hat{V}_T$ was used for the calculation. Due to the presence of the symmetry breaking term, the energy levels have avoided-level crossing as shown in the inset. For small $\hat{V}_T$, the energy eigenvalues are given to good approximation by:

$$E_m = -Dm^2 - Am^4 - g_z \mu_B H_z m\,. \tag{2}$$

The fields at which the energy level resonances between m (the left well) and m' (the right well) occur are given by:

$$H_z = N\frac{D}{g_z\mu_B}\left[1+\frac{A}{D}\left(m^2+m'^2\right)\right], \tag{3}$$

where $N=-(m+m')$ is the "step number". The resonant fields for $m=-9$ and $m=-10$ are indicated by dotted red lines in Fig. 3. Inclusion of the second order longitudinal anisotropy, $A\hat{S}_z^4$, has the effect of shifting the energy levels so that the energy eigenvalues no longer come into resonance simultaneously for different ms at the same N resonant number. Rather, each step N now represents a family of energy resonances that occur at slightly different magnetic fields.

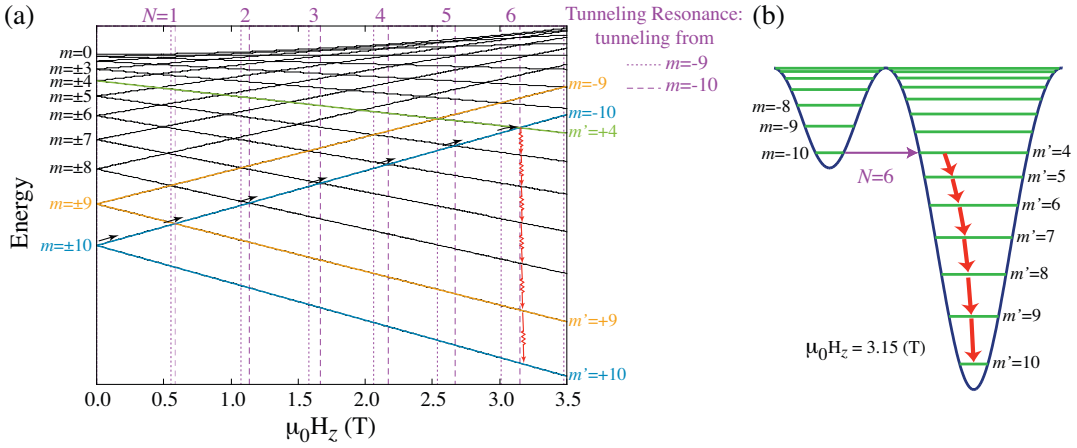

Figure 4: The ground state tunneling at the resonance, $N=6$ is shown with arrows. In part (a), spin is originally at $m=-10$ and stays there until $\mu_0 H_z = 3.15\,\mathrm{T}$. At very low temperatures, spin can relax only through ground state tunneling. At $\mu_0 H_z = 3.15\,\mathrm{T}$, the spin tunnels from $m=-10$ to $m'=4$ and relaxes to $m'=10$ immediately by releasing phonons. In part (b), the double-well potential at the resonant magnetic field is shown.

At very low temperature ($<0.5\,\mathrm{K}$), only ground state tunneling proceeds (the example shown in Fig. 4) and the relaxation rate does not depend on temperature as will be shown later. (see Fig. 9). Above $\sim 0.5\,\mathrm{K}$, thermally assisted tunneling also can proceed as the spin gets excited to higher states once in a while by phonons more and more often at higher temperature as example shown in Fig. 5. Thermally

assisted tunneling can proceed from any of the excited states. The strength of the relaxation at each level depends on the temperature and the tunnel splittings. At even higher temperature ($> 3.0\,\mathrm{K}$), over-the-barrier hopping also occurs as example shown in Fig. 6.

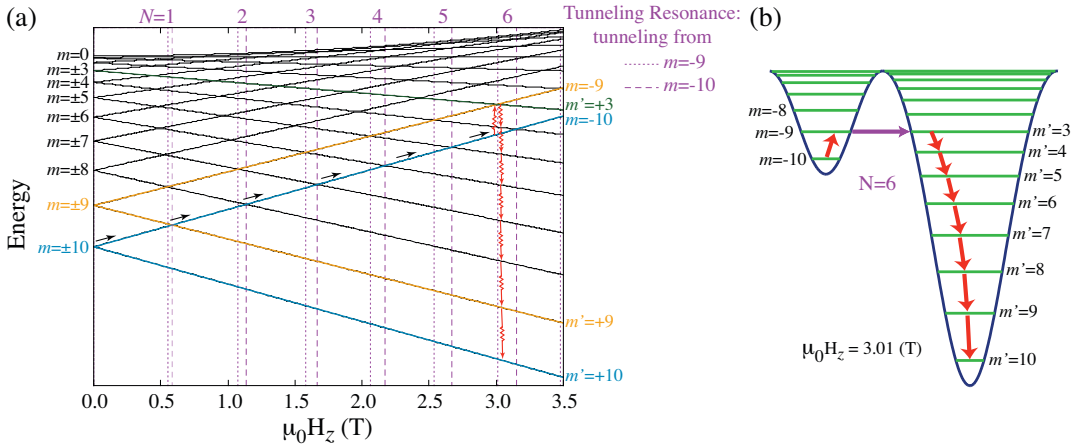

Figure 5: The thermally assisted tunneling from $m = -9$ at the resonance, $N = 6$ is shown with arrows. The resonance for $m = -9$ occurs at a slightly smaller magnet field than the one for $m = -10$ shown in Fig. 4. In part (a), the spin is originally at $m = -10$ and stays there right before $\mu_0 H_z = 3.01\,\mathrm{T}$. At low temperature, spin stays at the ground state for most of the time, but can get excited for a short time every once in a while. Right before $\mu_0 H_z = 3.01\,\mathrm{T}$, the spin gets excited to $m = 9$, tunnels to $m = 3$ and relaxes to $m = 10$ immediately by releasing phonons. In part (b), the double-well potential at the resonant magnetic field is shown. Tunneling is easer at higher excited states since the tunnel splitting is larger.

The tunneling probability is described by the Landau-Zener-Stueckelberg (LZS) formula [136–138], the exact solution to the Schrödinger equation for a two-level system with diagonal terms that change linearly with time and off-diagonal symmetry-breaking terms that are constant (see Fig. 7). The probability of remaining at the initial state is given as:

$$P_{LZS} = \exp(-\pi\Delta^2/v\hbar)\,, \tag{4}$$

where Δ is the tunnel splitting and v is the energy sweep rate. Δ is the size of the gap formed at the anti-crossing. v is the rate at which the energy levels approach each other (in the absence of any symmetry breaking terms) and in our case is proportional

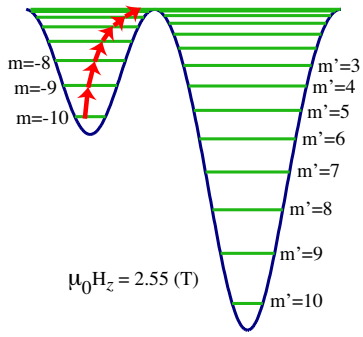

Figure 6: When not on resonance, spin can relax only at high temperature via over-the-barrier hopping.

to the magnetic field sweep rate, dH_z/dt. From Eq. 4, it is clear that the *slower* the magnetic field is swept, the *greater* the probability of tunneling to occur. Also, the probability of tunneling *increases* with *increasing* tunnel splitting.

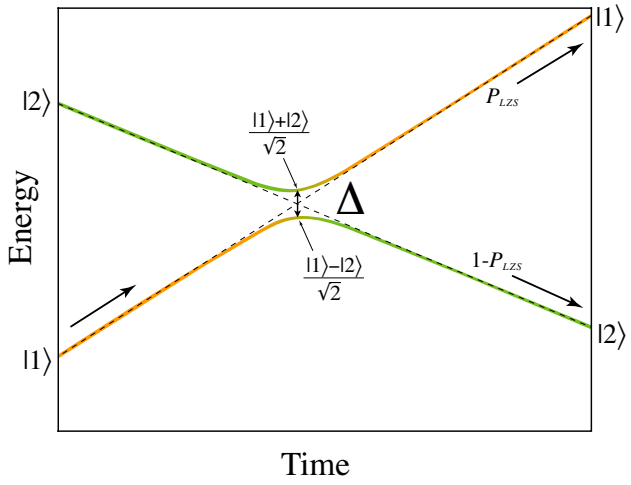

Figure 7: The two level system of coherent LZS process at an anti-crossing is shown. At far away from the crossing, $t = -\infty$, $|1\rangle$ and $|2\rangle$ are the eigenstates. At the crossing, due to the symmetry breaking term, the two state will not cross, and symmetric and anti-symmetric terms of $|1\rangle$ and $|2\rangle$ become the eigenstates at the middle of the crossing. P_{LZS} is the probability to stay in the initial state at $t = \text{inf}$ after a linear energy sweep.

Eq. 4 was derived for coherent tunneling in a two-level system. In our case, it may not be applicable. Due to the short de-coherence time, especially at higher excited states, the line-widths of the energy levels easily exceed the size of tunnel splittings even at very low temperatures. Furthermore, there are more than two states. As

seen in Fig. 4, at $\mu_0 H_z \neq 0$, in the stable well, spins would relax down to the ground state in the stable well due to the short life time of the higher excited states during the LZS crossing. Interestingly, though, when all these complications are taken into account, exactly the same formula as Eq. 4 was derived [46, 97, 139].

2.2 Magnetization Measurements

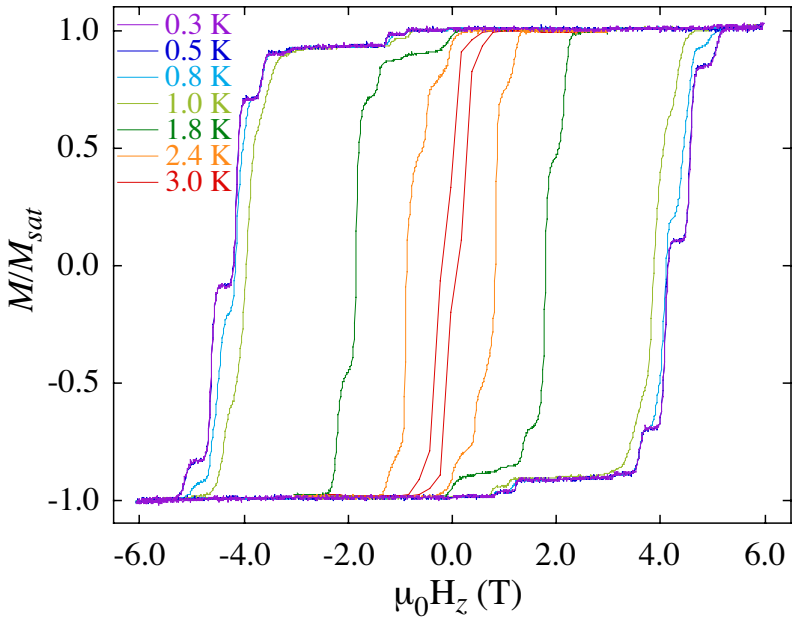

Figure 8: The magnetization curves between 3.0 K and 0.3 K with a magnetic field sweep rate of 10 mT/s are shown.

Fig. 8 shows the magnetization measurements for the case where the magnetic field is swept along the easy axis between 3.0 K and 0.3 K. The steps in the magnetization curves are indications that the magnetization is relaxing faster at certain fields than at others. Friedman *et al.* were the first to observe and interpret these steps [34, 140] as evidence of quantum tunneling of magnetization. This was later confirmed by others [35, 36, 141–144]. From Fig. 8, it is clear that at higher temperatures the magnetization relaxes at lower fields. This is because at higher temperatures, the spins can relax through thermally assisted tunneling in addition to ground state

tunneling. Above 3.0 K, the behavior is no longer hysteretic and the steps disappear. This is due to the fact that equilibrium is established via over-the-barrier hopping on time scales shorter than the magnetic field sweep rates used in these experiments.

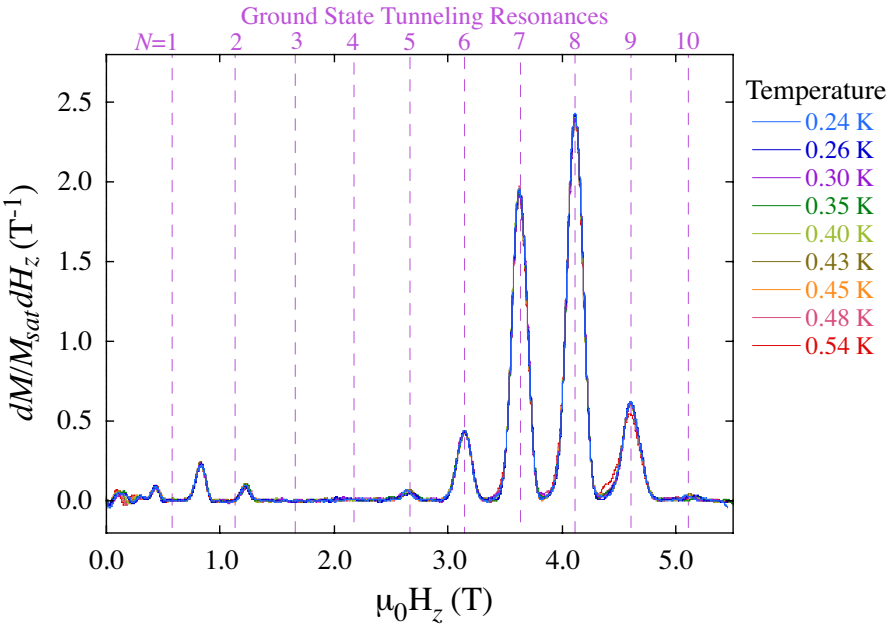

Figure 9: The derivative of the normalized magnetization curves with respect to applied field of Mn_{12}-acetate for temperatures between 0.54 K and 0.24 K at a magnetic field sweep rate of 1.85 mT/s. The curves overlap indicating that the tunneling process has become independent of temperature. The position of the peaks indicate the transition fields. The vertical dashed purple lines are the calculated transition fields corresponding to ground state tunneling.

An important observation to make is that the magnetization curves become independent of temperature below $T_G = 0.5$ K [57,59,60]. Fig. 9 is a plot of $dM/M_{sat}dH_z$ (derivative of normalized magnetization curves) between 0.54 K and 0.24 K as a function of magnetic field. All the curves overlap, indicating that the tunneling process has become independent of temperature. Plotting $dM/M_{sat}dH_z$ is a simple way of determining the fields at which tunneling occurs. Also plotted in Fig. 9 are the fields at which energy resonances are expected to occur for ground state tunneling ($m' = -10$) (shown by the vertical dashed purple lines). The fact that the magnetization curves are independent of temperature, as well as the fact that the peaks occur at fields

corresponding to energy resonances of the ground state, are strong evidence that the system is tunneling from the ground state.

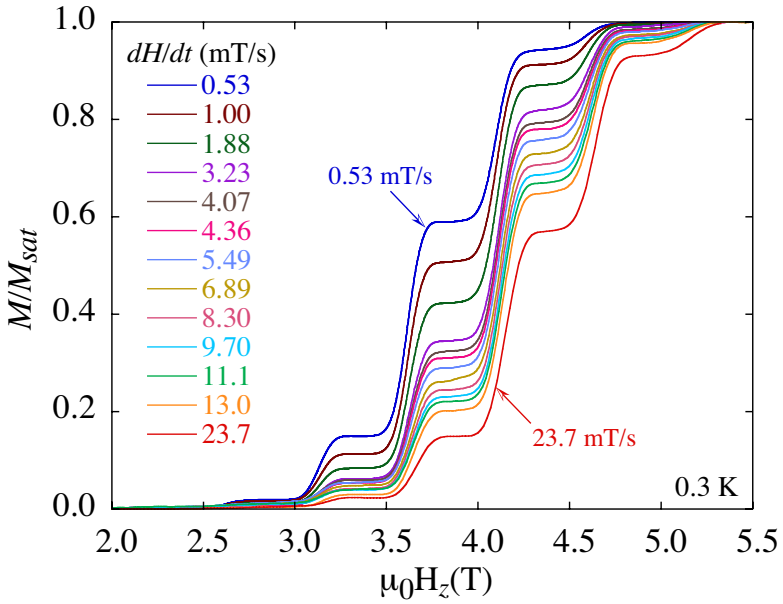

Figure 10: Ground state tunneling rate dependence on the magnetic field sweep rates is shown. Each curve depicts the normalized magnetization for a different sweep rate at 0.3 K.[1]

Also visible in Fig. 9 are several peaks that appear at fields below $\sim 1.2\,\mathrm{T}$. These peaks are due to a second species of Mn_{12}-acetate which present $\sim 5\,\%$ of molecules in all Mn_{12}-acetate crystals [11, 145]. They have the same $S = 10$, but the anisotropy energy is smaller. Therefore, they relax at smaller magnetic fields before any of the molecules of the main species of Mn_{12}-acetate relax. As a result we are always able to separate them easily. Although several isomeric forms [4, 5, 130, 141, 146, 147] of Mn_{12}-acetate have been chemically identified, only one minority species is present in the samples studied here with sufficient concentration to produce measurable effects.

Fig. 10 shows the magnetization of zero-field-cooled samples for various sweep rates. Each curve represents one sweep of the external field and each sweep was

[1]The magnetization due to the second species has been removed from the data by first determining the saturation level for the second species, then subtracting this amount from the magnetization curves and then normalizing.

performed at a different sweep rate. All these field sweeps were taken at 0.3 K so that only ground state tunneling occurs. This makes analyzing the data significantly easier since only one tunneling channel is available. For thermally assisted tunneling, the energy resonances are sufficiently close to one another and the widths of the peaks sufficiently broad that it is difficult to resolve the energy resonances. From these curves it is clear that the sweep rate plays an important role in determining how many molecules tunnel at each energy resonance. For all the samples the magnetization relaxes at lower fields when the field is swept more slowly. This is in agreement with the predictions of the LZS formalism, since the tunneling probability increases with decrease energy sweep rate.

3 Magnetic Avalanches in Mn_{12}-acetate

In Section 2, it was shown that the magnetization in Mn_{12}-acetate relaxes by thermal excitation, quantum tunneling, or both. At very low temperatures, the spin can reverse only by tunneling from the ground state of the metastable well. This purely quantum mechanical process yields a constant relaxation rate regardless of the temperature. The hysteresis curves have step-like behavior at fields corresponding

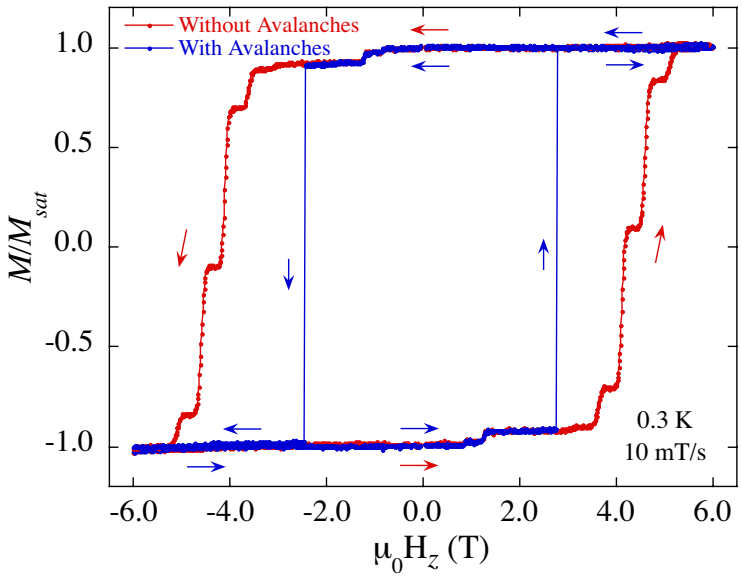

Figure 11: Hysteresis curves of a single crystal of Mn_{12}-acetate were measured at 0.3 K with a magnetic field sweep rate of 10 mT/s. With the same sample and same conditions, sometimes an avalanche occurred and sometimes an avalanche did not occur. Without avalanches, the hysteresis curves were reproducible showing beautiful step-like relaxation at the ground state tunneling resonance fields (red trace). With this sample at around 0.3 K, an avalanche occurred about 50 % of the time at various magnetic fields. The blue curve shows one such example of an avalanche. The full magnetization was reversed in a short time. The time resolution for this measurement was $\sim$1 s. With this slow sampling rate, no data points were captured during an avalanche.

to the calculated tunneling resonances, as shown by the red curve in Fig. 11. At intermediate temperatures, the population of phonons with sufficient energy to excite the spin over the barrier is too low; however there is sufficient population of phonons with enough energy to excite the spins to some of the low lying excited states from

which they can tunnel more easily. At higher temperatures, over-the-barrier hopping dominates.

These relaxation mechanisms have been carefully studied in Mn_{12}-acetate under controlled conditions. However, much faster relaxation by way of an avalanche [126] is also known to frequently occur at low temperatures in relatively larger samples. When this happens, the whole magnetization is reversed in one step in a very short time with a relatively small reversing magnetic field as demonstrated by the blue curve in Fig. 11. In this section, detailed studies of the phenomenon of magnetic avalanches are presented.

Section 3.1.1 provides an overview of our understanding of the avalanche phenomenon and other related subjects at the time when we began our investigation, as well as the motivation for our investigations of avalanches. In order to consider only the intrinsic properties of the material and also to simplify the list of possible mechanisms leading to avalanches, only single crystals of Mn_{12}-acetate were used in our measurements. The measurements were performed mainly at low temperatures since avalanches occurred only at low temperatures in high quality single crystals. Our studies focussed mainly on two aspects of avalanches which may or may not have a close relationship to each other. The first was to determine the conditions for avalanches to occur naturally (conditions for self-triggering) while sweeping a magnetic field back and forth. The second was to determine how avalanches proceed once they are triggered. The first of these did not require any additional experimental preparation so our early measurements were focused on studying the conditions for triggering avalanches and the distribution of magnetic fields for which avalanches were triggered during field sweeps. These results are presented in Section 3.2. We then prepared measurements with higher time resolution and spatial resolution using an array of Hall sensors monitored by fast recording devices in order to study the propagation of avalanches, as described in Section 3.3. A thermometer was also installed

close to the samples and its response during avalanches is presented in Section 3.4.

3.1 Background of Avalanches

3.1.1 Overview in Avalanches

A magnetic avalanche is a runaway process during which energy that has gradually accumulated is suddenly released. In the case of magnetic avalanches in Mn_{12}-acetate the energy is stored as Zeeman energy of the spins. To understand this more concretely, recall that the spin state in Mn_{12}-acetate resides in a double well potential with a barrier of 65 K. At very low temperature (< 3 K), the probability that the spin will tunnel or become thermally excited over the barrier is so low that the spin stays frozen in one of the wells for a long time. When an external magnetic field is applied along the easy axis, the double well potential is asymmetric; the energy of one well (stable well) is lower than the other (metastable well) due to Zeeman splitting (see Fig. 12). To observe avalanches samples are prepared with all the molecules magnetized in one of the wells by either cooling the sample in the presence of a magnetic

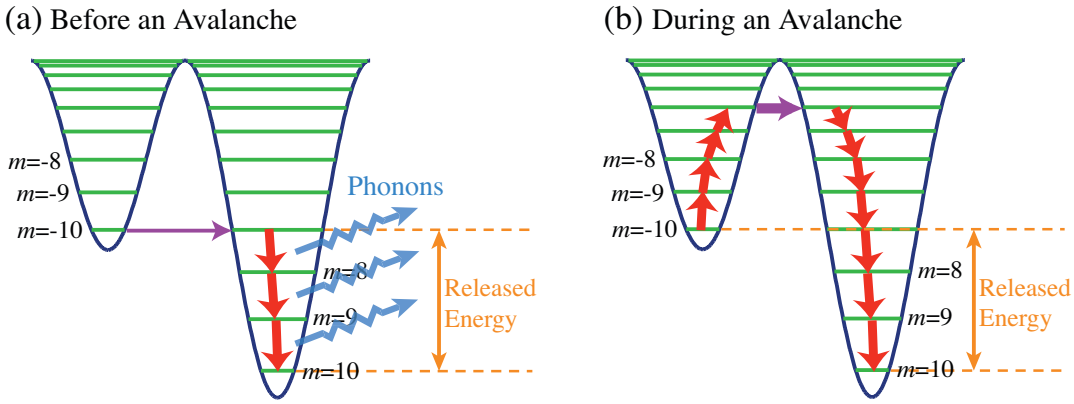

Figure 12: **(a)** At very low temperatures, the spin can reverse only through ground-state tunneling (the thin purple arrow) from the metastable well (left side well) to stable well (right side well). As soon as it tunnels, it decays to the ground state in the stable well by emitting phonons. Consequently, the released phonons increase the temperature of the neighboring molecules. **(b)** If the temperature rises, the spin of the remaining molecules can tunnel more easily from the excited state (thick purple arrow) and release more phonons. As a result, an avalanche occurs.

field or by applying a large magnetic field at low temperature. Either technique leads to a sample with the spins of all the molecules aligned with the magnetic field and in one of the wells.[2] To increase the potential energy of the system and to place the system in a metastable state, the magnetic field is swept in a direction opposite to the sample magnetization. All the molecules now have their spin in the metastable well (left hand well of Fig. 12 (a)). At low temperature, the spin can reverse only through ground-state tunneling. When the spin reverses, the difference in the energy between metastable well and stable well (the Zeeman splitting) can be released through the emission of phonons (Fig. 12 (a)). Consequently, the released phonons increase the temperature of neighboring molecules. For the controlled release of the magnetic potential energy, the temperature of the sample should remain constant; this can happen when the rate at which energy is released due to tunneling events is lower than the rate at which heat diffuses away. However, if the process depicted in Fig. 12 (a) happens to many molecules in a localized region of the sample and during a sufficiently short amount of time, then the temperature increases and the magnetic relaxation process becomes uncontrolled. In this case, when the temperature of the sample increases, the spin of the remaining molecules can tunnel more easily from excited states which in turn releases more phonons (Fig. 12 (b)). This process continues until all the molecules rapidly release their magnetic potential energy by flipping their spin. When this happens, an avalanche is said to have occurred.

3.1.2 Historical Background

Prior to the discovery in 1996 by Friedman, *et al.* [34,140] and then by others [35,148] of regularly-spaced multiple steps in the hysteresis loops due to resonant spin tunneling in Mn_{12}-acetate, early experiments by Paulsen, *et al.* [126,149] found sharp single-

[2]For some samples an avalanche occurred, even when the sample was prepared with 50 % of the molecules in one well and the other 50 % in the other well by cooling it in the absence of a magnetic field (zero-field cooling).

step reversals of the magnetization in 1995. They measured hysteresis curves for a cluster of several crystals of Mn_{12}-acetate using a magnetic sweep rate of 0.3 mT/s at various temperatures down to 175 mK. The magnetic field was applied at various angles with respect to the easy axis. Avalanches were found to always occur at temperatures below 1.5 K at reversing magnetic fields between 0.5 T to 1.5 T. A superconducting pick-up coil was used with a sampling rate of 516 Hz for detection. The duration of an avalanche was roughly estimated to be at most 10 ms for the samples in the 2-3 mm length range; from these values they estimated the speed of the heat pulse to be at least 0.3 m/s (5×10^{-9} sec/molecular length) and they discussed this in comparison with the spin-phonon relaxation time of $\tau_0 = 10^{-6}$ s. The temperature measured near the samples increased up to 1.5 K. The magnetic fields at which an avalanche occurred varied in a somewhat stochastic way within some distribution. The distribution was also found to be sample-dependent.

Paulsen and Park [126] suggested that these avalanches are *"a kind of chain reaction or thermal runaway; when one spin flips, it heats its neighbors above the blocking temperature, greatly increasing the probability that they will flip and in turn heat their neighbors and so on until all spins have turned over."* Using the measured specific heat from Ref. [150] and the calculated total released energy, they estimated the rise in sample temperature as 12 K for an avalanche which occurred at 1 T on the assumption that no heat escaped from the sample. The origin of the avalanches was unclear, but it was suggested that there was a resemblance to a system of self-organized criticality [151].

Fominaya, *et al.* [152] observed heat emissions caused by magnetization relaxation. Del Barco, *et al.* [127] numerically confirmed the enhancement of magnetization relaxation due to heating caused by magnetization relaxation for a zero-field-cooled oriented powder sample of Mn_{12}-acetate at temperatures above 1.9 K in a pulsed magnetic field with a slew rate of 140 T/s.

For many years, in order to study the behavior of SMMs under controlled conditions at fixed temperatures, a great deal of effort was directed at avoiding uncontrolled magnetic avalanches rather than investigating them further. Luckily avalanches tend to occur only at low temperatures in larger samples. Stimulated by a suggestion by Chudnovsky and Garanin in 2002 [153], recent studies of Mn_{12}-acetate have focused on the possible observation of superradiance triggered by magnetization avalanches [154–156]. Superradiance was originally predicted by Dicke in 1954 [157] and later observed in a number of atomic and molecular gasses [158, 159]. A particle prepared in its excited state has a certain probability to decay by the spontaneous emission of light. However, if there are other identical particles within the wavelength of the light emitted, the light can not be emitted independently. For a system with N identical particles, this results in a cooperative spontaneous emission which has N times larger probability of an emission than that of an individual particle. Moreover, the emitted radiation is coherent with power $\propto N^2$.

SMMs are very suitable for the emission of superradiance since Avogadro's number of nearly identical molecular spin systems acting nearly independently (with only magnetic dipolar inter-molecular interactions) are located within the wavelengths corresponding to the energy spacings between the levels in Mn_{12}-acetate [153]. Ordinarily, the spin decays from the excited states by emitting a phonon since phonons have a larger number of modes than photons in the sample. However, when a very large number of molecules are prepared simultaneously in their excited state (in other words, when a population inversion happens), Chudnovsky and Garanin suggested there is a high probability for emission of superradiance.

During an avalanche in Mn_{12}-acetate, the sample experiences rapid heating. A large number of molecules are promoted to the excited states from which the electronic spin tunnels very easily to the stable well due to the larger tunnel splittings of the excited states. After tunneling to the stable well, the spin finds itself in a highly

excited state as seen in the right hand well in Fig. 12 (b). If a large number of molecules undergo the same process in a short time during an avalanche, a population inversion is created resulting in the possible emission of superradiance [154].

In an experimental search for superradiance during avalanches in a cluster of Mn_{12}-acetate crystals, Tejada, *et al.* reported in 2004 that the magnetization reversal occurs in a time on the order of 0.1 s at temperatures above 1.8 K [154]. They also detected a short burst of electromagnetic radiation from the sample using an InSb bolometer. The hysteresis curves and the position and amplitude of the radiation bursts associated with an avalanche were totally reproducible at a fixed temperature and magnetic field sweep rate.

Later measurements by Bal, *et al.* indicated faster switching times of avalanches on the order of milliseconds [155]. They also found that the magnetization was not reversed uniformly throughout the sample during an avalanche. They used a Josephson junction to extract spectral information of the radiation associated with avalanches. However, they did not detect any significant radiation at well-defined frequencies, as might be expected for superradiance. In their case, above 1.8 K for a large cluster of crystals, avalanches occurred at magnetic fields corresponding to tunneling resonances, and they occurred at the same, reproducible, magnetic field for a given fixed temperature, which is consistent with Ref. [154]. The magnetic field at which an avalanche occurred increased as the temperature was raised. With the magnetic field sweep rate of 5.5 mT/s which they used, avalanches did not occur above ~ 3 K. In more recent measurements, the group of Tejada, *et al.* [156] reported avalanches in a large single crystal above 1.8 K. The magnetization switching time was on the order of milliseconds, which is more consistent with Ref. [155].

Chudnovsky and Garanin [153] also suggested that under certain conditions using a very fast magnetic field sweep, magnetization reversal of SMMs can occur collectively through the emission of superradiance rather than by Landau-Zener tunneling

for individual spins [160]. These experimental conditions were realized in experiments performed in Fe_8 by Jordi, *et al.* in 2004 [161]. They applied magnetic field sweep rates between 10^3 T/s and 10^{-4} T/s to oriented microcrystals of Fe_8 at a temperature below 1 K. With the fast field sweep, the magnetization relaxed away from the ground-state tunneling resonance fields in a short time of 30 μs to 60 μs. The magnetic relaxation agreed remarkably well at different magnetic field sweep rates with the model for superradiance. Subsequently, Vanacken, *et al.* reported similar results for Mn_{12}-acetate [162]. A magnetic field sweep rate of 1×10^3 T/s (3×10^3 T/s) was used at temperature down to 670 mK, and the magnetization relaxed in 180 μs (100 μs) between 1.4 T and 1.6 T (1.5 T and 1.8 T). The value of the magnetic field at which the magnetization relaxed increased as the magnetic sweep rate was increased.

Wernsdorfer suggested that the fast magnetization relaxation in Ref. [162] was due instead to thermal avalanches triggered by the faster relaxing species (the second species discussed in Section 2.2) [163]. He applied magnetic field sweep rates of 0.3 mT/s to 680 mT/s to a small crystal ($20 \times 6 \times 5\,\mu m^3$) of Mn_{12}-acetate at 60 mK. Avalanches occurred reproducibly at the ground-state tunneling resonance around 4 T. The entire magnetization was reversed on a time scale faster than a millisecond. The value of the magnetic field at which avalanches occurred decreased as the magnetic field sweep rate was increased.

In 2003, we performed preliminary experiments to detect radiation from Mn_{12}-acetate at Brookhaven National Laboratories in collaboration with Jiufeng Tu, Laszlo Mihaly and Larry Carr [164]. A 1.6 K Si bolometer was used to monitor the emission of radiation by a Mn_{12}-acetate sample in a swept magnetic field. The bolometer was located 1.5 m away form the sample in a separate cooling system. The samples were prepared in the form of three cylinders of 5.3 mm diameter and 5 mm height. The cylinders were filled with many crystals of typical dimensions $0.7 \times 0.7 \times 2.0\,mm^3$. The crystals in one cylinder were randomly oriented. The crystals in the other two

cylinders were oriented by setting in 1266AB stycast in a field of 3.0 T at room temperature for six hours. One of the oriented cylinders was placed along the magnetic field and the other was placed about 30° with respect to the magnetic field.

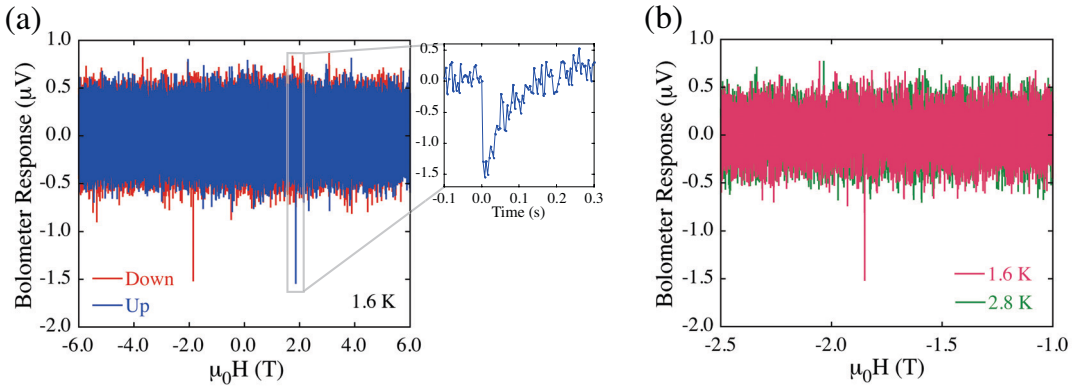

Figure 13: **(a)** The bolometer responses plotted as a function of magnetic field while it was swept upward from -6.0 T to 6.0 T (blue trace) and downward from 6.0 T to -6.0 T (red trace) using a sweep rate of 17 mT/s at 1.6 K. In the inset, one of the pulses is plotted as a function of time. **(b)** The bolometer response plotted as a function of magnetic field with magnetic field sweeping downward at a sweep rate of 17 mT/s at 1.6 K and 2.8 K.

The bolometer responses are plotted in Fig. 13 (a). The magnetic field was swept upward from -6.0 T to 6.0 T (blue trace) and down from 6.0 T to -6.0 T (red trace) with a sweep rate of 17 mT/s at 1.6 K. The bolometer response decreases when it absorbs radiation. One pulse was observed for each sweep and these are symmetric with respect to each other in magnetic field position and shape. In the inset of Fig. 13, one of the pulses is plotted as a function of time with 4 ms resolution. In Fig. 13 (b), the bolometer responses with magnetic field sweeping downward are plotted for 1.6 K and 2.8 K. Consistent with our expectations, no pulse was observed at 2.8 K, which is near or above the blocking temperature. Even though the magnetization was not monitored, we strongly believe that the spike of radiation was associated with an avalanche. Spectral information was not obtained in these experiments. Therefore, we do not know whether it was coherent radiation associated with superradiance or thermal radiation associated with heating of the sample.

3.2 Triggering of Avalanches

The triggering mechanism leading to magnetic avalanches in Mn_{12}-acetate is still not known. Once an avalanche is triggered, it proceeds very fast and lasts only for a short time, which makes measuring the time evolution of an avalanche very challenging. However, it is simple to detect that an avalanche has occurred, as it results in the complete reversal of the magnetization. It is therefore possible to study the conditions (temperature, magnetic field, other variables) for which avalanches occur. This section reports the various conditions under which avalanches were observed.

In previous measurements, a number of experiments have reported avalanches at relatively high temperatures above 1.8 K in a pumped ^{4}He cryostat. For a fixed temperature and magnetic field sweep rate, these avalanches occurred at the same, reproducible field [154–156]. Moreover, the avalanches occurred in the middle of a tunneling resonance where there was some relaxation by tunneling prior to the avalanche. However, this is not the case for Ref. [126] or what we found in our experiments. The most significant difference in these experiments is temperature. In the experiments reported in Ref. [126], a dilution refrigerator operating down to 50 mK was used. All avalanches occurred below 1.5 K, and the magnetic fields at which they occurred varied stochastically within a non-uniform distribution. The reversing field was too small at those temperatures to cause any relaxation prior to the avalanche, and avalanches occurred without any precursors[3].

The avalanches above 1.8 K, were observed in an assembly of many crystals (later also in a very large single crystal [156]) and at a relatively fast thermally-assisted tunneling resonance.[4] During the tunneling resonance, the spin relaxes from

[3]There were a few exceptions in Ref. [126].

[4]Reproducible avalanches also occurred in a very small crystal of $20 \times 6 \times 5\ \mu m^3$ at 60 mK with sweep rates above 68 mT/s [163]. In this case the temperature is low, but the behavior of these avalanches is similar to those observed at the higher temperatures, as they were reproducible and occurred at the tunneling resonance. The conditions for triggering avalanches depend on various factors such as magnetic sweep rate, temperature, sample size & quality and cooling environments.

the metastable well to the stable well, and the biased Zeeman energy in the double well potential is released (see Fig. 12 (a)). The sample temperature naturally rises and an avalanche is triggered. However, in our experiments, this simple explanation can not be applied since many avalanches occurred off-resonance at magnetic fields where there was very little (or no) relaxation via tunneling. In this section, the conditions for triggering avalanches for the latter case will be investigated further with different single crystals at low temperatures. Paulsen, *et al.* showed a plot of the distribution of magnetic fields at which avalanches were triggered for one sample at 0.17 K [126]. However, no comparison was possible of the conditions for magnetization relaxation with and without avalanches since avalanches always occurred and the resonant steps of quantum tunneling of magnetization in Mn_{12}-acetate had at that time not yet been discovered.

3.2.1 Measurements in Avalanche Fields and Temperatures

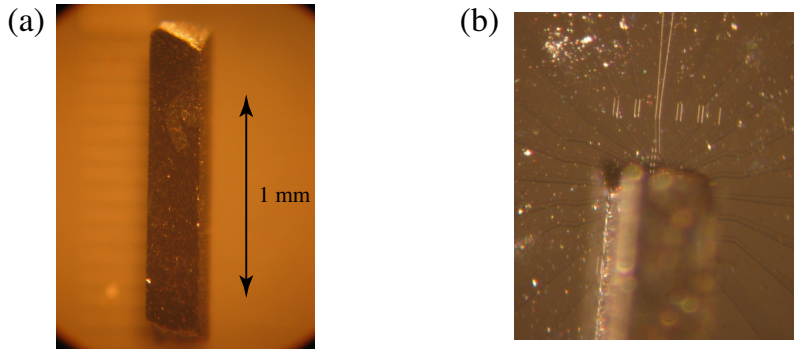

Figure 14: **(a)** A relatively large crystal of Mn_{12}-acetate, sample A. The long axis is the magnetic easy axis. **(b)** Sample A mounted on a array of Hall sensors. The sample looks different because the camera was not focused on the sample but on the surface of the Hall-sensor chip instead.

The magnetization of single crystals of Mn_{12}-acetate was measured using a $10\times10\ \mu m^2$ Hall sensor composed of a two-dimensional electron gas in a GaAs/AlGaAs heterostructure (see Section 4.2) using excitation currents as small as $1\,\mu$A at temper-

atures down to 0.3 K.[5] For illustrative purposes, sample A is shown mounted on a calibrated slide in Fig. 14 (a) and on a Hall sensor in Fig. 14 (b). A longitudinal magnetic field, swept at a constant rate, was applied along the easy axis. Good thermal contact was provided by direct immersion in ^{3}He liquid (see Section 4.1). Data were obtained for seven single crystal samples of Mn_{12}-acetate of dimensions $0.27\times0.27\times1.4$ mm^3 (sample A), $0.4\times0.4\times1.8$ mm^3 (sample B), $0.15\times0.15\times0.2$ mm^3 (sample C), $\sim$0.4 mm length in c-axis (sample D), $0.29 \times 0.29 \times 0.64$ mm^3 (sample #1), $0.28 \times 0.28 \times 1.44$ mm^3(sample #2) and $0.24 \times 0.24 \times 1.02$ mm^3 (sample #3).

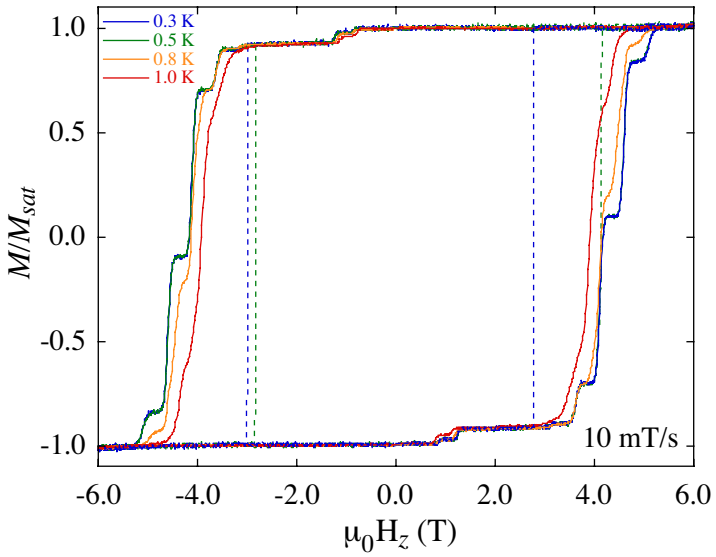

Figure 15: Magnetization versus magnetic field applied along the easy axis of Mn_{12}-acetate at four different temperatures as labeled. Data is shown for sample A using a magnetic field sweep rate of 10 mT/s. Avalanches (dashed lines), which occur about 50 % of the time at random magnetic fields, are shown at 0.3 K and 0.5 K. In the absence of an avalanche, the magnetization relaxed by ground-state tunneling for 0.3 K and 0.5 K (blue and green solid lines). No avalanches were observed above 0.8 K under these conditions. The magnetization also relaxed by thermally-assisted tunneling in addition to ground-state tunneling for 0.8 K and 1.0 K (orange and red solid lines).

The magnetization is shown as a function of magnetic field in Fig. 15 at four different temperatures between 0.3 K and 1.0 K for a magnetic field sweep rate of 10 mT/s. In agreement with earlier measurements, the hysteresis curves at 0.3 K

[5] An excitation current of 1 μA was used for sample A, 50 μA was used for samples B and C, 10 μA was used for sample D, and 2 μA was used for sample #1, sample #2 and sample #3.

and 0.5 K (blue and green solid lines) coincide, indicating that the magnetic relaxation is completely dominated by ground state tunneling. Small changes are observed at the two higher temperatures (orange and red solid lines), indicating that thermally-assisted tunneling is playing a measurable role. Also shown in Fig. 15 are four avalanche events, at 0.3 K and 0.5 K (blue and green dashed lines). Please note that the change in magnetization below 1.5 T is known to be the magnetization relaxation of the second species (see Section 2.2).

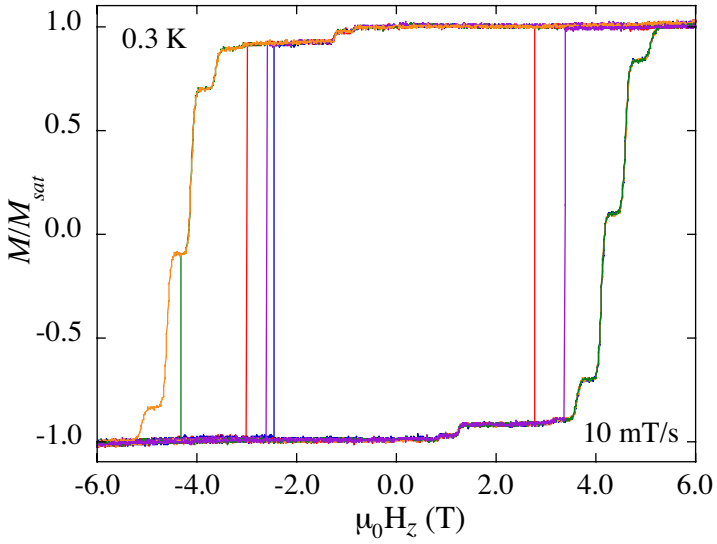

Figure 16: Magnetization versus magnetic field applied along the easy axis of Mn_{12}-acetate at ~ 0.3 K using a magnetic field sweep rate of 10 mT/s for sample A, showing several hysteresis curves with and without avalanches. The fields at which avalanches occurred were distributed as shown in Fig. 17.

Fig. 16 shows the stochastic nature of the magnetic fields associated with the triggering of avalanches. There are five full hysteresis curves (ten magnetic reversals) obtained under the same conditions at ~ 0.3 K using a field sweep rate of 10 mT/s. Six magnetic avalanches occurring at six different magnetic fields are shown, as well as four reversals which occurred without an avalanche. The probability of an avalanche was different for different samples. In the temperature range between 0.3 K and 0.6 K, avalanches occurred roughly 50 % of the time for sample A and 100% of the time for

sample B. This difference may be associated with different sample size, sample quality or some other factor.

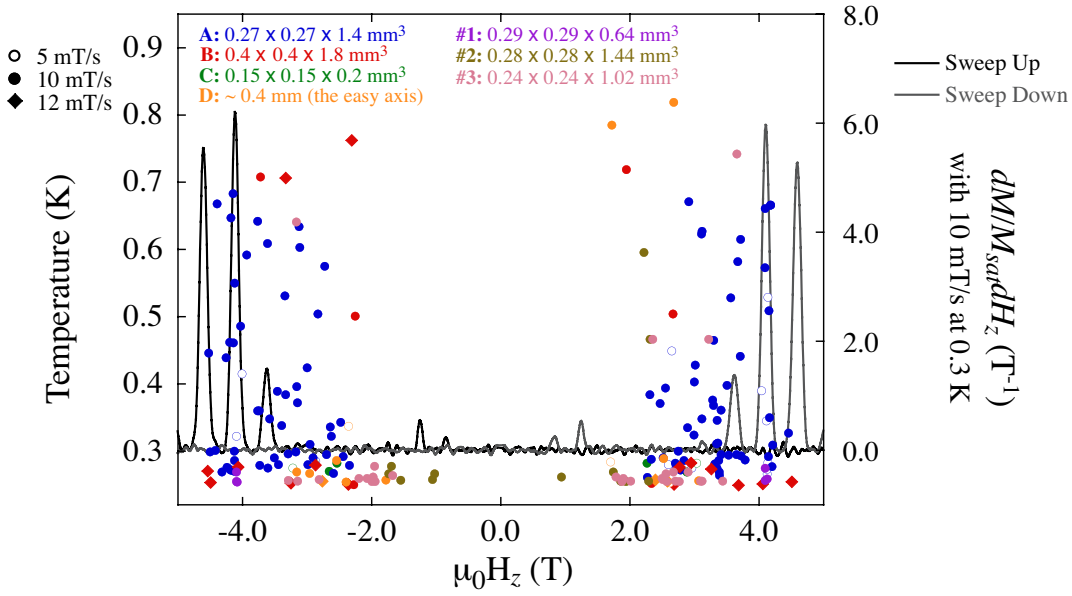

Figure 17: Magnetic fields at which avalanches occurred at different temperatures above 0.3 K for seven samples. The absence of data points above 0.82 K reflects the fact that no avalanches were observed above this temperature.[6] Note that points at positive and negative fields represent different data, and are not simply reflections about the horizontal axis. Closed and open circle marks represent sweep rates of 10 mT/s and 5 mT/s, respectively. Closed diamond marks represent sweep rates of 12 mT/s. To indicate the resonant magnetic fields for ground state tunneling, the first derivative of an avalanche free M versus H_z curve for sample A at 0.3 K (blue curve of Fig. 15) is shown by the solid black curve for the upward sweep and by the gray curve for the downward sweep.

For seven single crystals of Mn_{12}-acetate of different dimensions, Fig. 17 shows the distribution of magnetic fields at which magnetic avalanches occurred at different temperatures above 0.3 K for field sweep rates of 5, 10 and 12 mT/s. No avalanches were recorded at temperatures above 0.82 K with the magnetic field along the easy axis. There appears to be no dependence on temperature for the number of data points accumulated, except for their apparent disappearance above 0.82 K.[6] This threshold

[6]More data were obtained in some temperature intervals than others, and the density of points does not therefore reflect the probability of obtaining an avalanche. Although preliminary results do indicate that the probability of avalanches decreases as the temperature is raised from 0.30 K to 0.82 K, additional measurements are needed to establish this rigorously.

temperature depends on the sample. For most small single crystals (below 0.5 mm in length) of good quality, which we used for the measurements to study quantum tunneling of magnetization in the past, avalanches never occurred in our temperature range (≥ 0.3 K).

The threshold temperature for each sample was not investigated carefully. There were many attempts to trigger an avalanche in a single crystal at higher temperatures (close to the temperatures for pumped ^{4}He), but they were not successful. This should be compared (but is not inconsistent) with Ref. [154–156] where avalanches occurred above 1.8 K only for an assembly of many crystals or one very large crystal and they did not occur for a small crystals. In our experiments, the apparent temperature cutoff for avalanches was the same regardless of the cooling environments.[7]

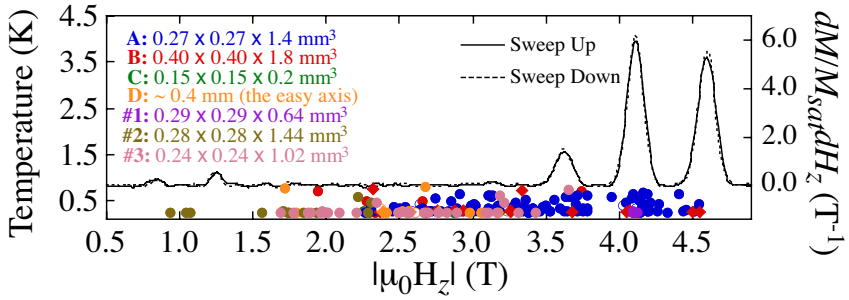

Figure 18: The same data in Fig. 17 is plotted as a function of $|\mu_0 H|$. To indicate the resonant magnetic fields for ground state tunneling, the first derivative of the M versus H_z curves (blue curve of Fig. 15) with sample A at 0.3 K without an avalanche is shown by the black solid and dashed curves.[8] The plot scale of the temperature has been compressed so that it reveals the absence of avalanches occurring at ~3.85 T and ~4.35 T which are between ground-state tunneling resonances above 3.5 T. There is also a gap between 1.0 T and 1.5 T.

In Fig. 17, for temperatures below 0.82 K, the magnetic fields at which avalanches occurred were distributed almost randomly between 1.5 T and 4.5 T. More than half

[7]The hysteresis measurements were repeated in the following order: in ^{3}He liquid at 0.4 K, in ^{3}He liquid at 0.9 K, in ^{3}He vapor at 0.4 K, and in ^{3}He vapor at 0.9K. The dependence of temperature remained the same (i.e. avalanches dissapeared at higher temperatures) regardless of whether the sample is immersed in ^{3}He liquid or ^{3}He gas.

[8]$dM/M_{sat}dH_z$ with only the positive values of $\mu_0 H_z$ for "Sweep Up" and the negative values of $\mu_0 H_z$ for "Sweep Down" are plotted as a function of $|\mu_0 H_z|$.

the avalanches occurred below 3.5 T above which appreciable relaxation proceeds by ground state tunneling under controlled conditions. In Fig. 18, the same data in Fig. 17 is plotted as a function of $|\mu_0 H_z|$ on a compressed temperature scale so that it is easier to see the distribution of fields at which avalanches occurred. From Fig. 18, we see the avalanches occur stochastically with a non-uniform distribution of fields. Above 3.5 T, there is a suppression in the number of avalanches occurring around 3.85 T and around 4.35 T, in the interval between ground-state tunneling resonances. This suggests that above $\sim$3.5 T, the relaxation through ground-state tunneling plays a role in triggering avalanches. There is also a gap between 1.0 T and 1.5 T. The magnetization due to the second species saturates around 1.5 T. The avalanches which occurred around 1.0 T may have been triggered by the relaxation of this second species [163].

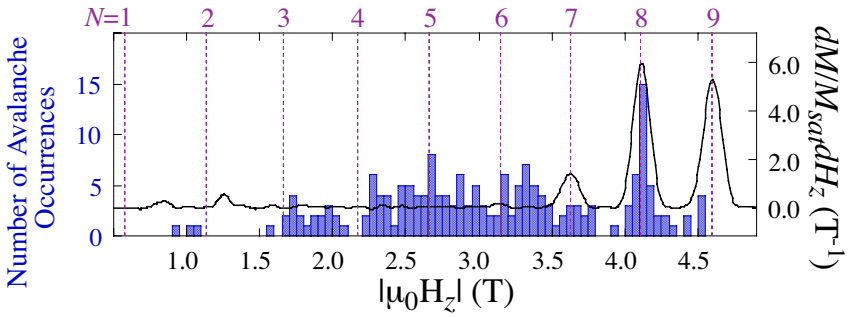

Figure 19: The number of occurrences of avalanches are plotted (blue bars) as a function of $|\mu_0 H_z|$.[9] Different samples had a different distribution of magnetic fields at which avalanches occurred. $dM/M_{sat}dH$ at 0.3 K, at which the magnetization relaxes predominantly through ground-state tunneling, is shown by the black curve. The absence of avalanches above 4.5 T derives from the fact that all the magnetization has already reversed at these fields, either by avalanches or by steps via controlled tunneling. The dashed purple lines indicate the magnetic fields for the ground-state tunneling resonances which were calculated using the Hamiltonian in Eq. 1 (see Section 2.2).

[9]The histogram indicates the number of avalanche occurrences and does not represent a probability distribution. For a probability distribution, the number of occurrences needs to be divided by number of attempts. In this case, smaller fields had a larger number of attempts since once an avalanche occurred at a smaller field, no more attempts were possible for higher fields. Different samples had a different probability (0 to 100 %) of magnetic reversal without an avalanche which depends mostly on sample size. These probabilities are not indicated in the histogram. The number of accumulated data points is not large enough to properly determine a probability distribution.

The number of occurrences for avalanches are plotted (blue bars) in Fig. 19 as a function of $|\mu_0 H_z|$. The number of avalanches which occurred in intervals of 0.05 T for all the samples for the temperatures below 0.6 K in Fig. 17 were simply summed and plotted in each bar.[10] As noted earlier, there is almost no temperature dependence in the hysteresis curves below 0.6 K indicating the magnetic relaxation proceeds predominantly through ground-state tunneling. The black curve represents the derivative of the magnetization curve (i.e. the tunneling rate) for sample A at 0.3 K. The dashed purple lines indicate the magnetic fields for the ground-state tunneling resonances. More than the half of avalanches occurred between 1.5 T to 3.5 T where there is almost no discernible magnetic relaxation by tunneling detected. Therefore we suggest that small defects, which consist of small number of molecules, with lower energy barriers (higher symmetry breaking for tunneling) are responsible for triggering these avalanches. Naturally, the molecules on the surface of the crystal suffer with high symmetry breaking. The dislocations are also possible source of defects [132, 153]. The details for other possible defects are discussed in Section 3.2.3.

As seen in Fig. 18 above 3.5 T, the probability for avalanches to occur is relatively larger on the tunneling resonances. The magnetic fields at which avalanches occurred are nevertheless still distributed in a stochastic way near the tunneling resonances, in contrast with the reproducible magnetic fields at which avalanches occurred in Ref. [154–156, 163].[11] This is discussed further in the next section.

3.2.2 Analysis of Triggering Conditions

As mentioned earlier, there are two aspects of a magnetic avalanche event: the conditions for triggering an avalanche, and what happens after it is triggered. In Section 3.3 we will learn from the local time-resolved measurements that magnetic avalanches are

[10] Different samples had a different distribution of magnetic fields at which avalanches occurred.

[11] For sample #1, avalanches repeatedly occurred at the the $N = 8$ ground-state tunneling resonance around 4.2 T.

trigged locally in one region of the sample, and after they are triggered, the avalanche front propagates with a constant speed through the sample. We also argue that this behavior is closely analogous to the propagation of a flame front (deflagration) through a flammable chemical substance. In other words, once they are triggered, the observed behavior is very close to the way nonexplosive fuel burns. Since we have made an analogy between magnetic avalanches and chemical deflagration regarding the propagation of the front, in this section, we will extend the analogy by considering the triggering conditions.

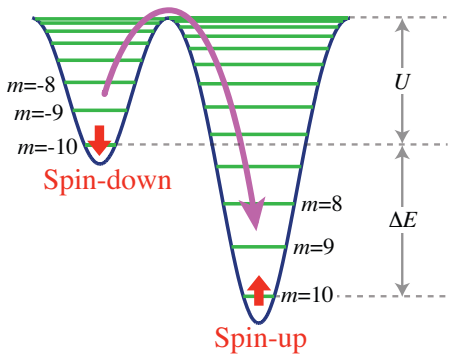

Figure 20: During magnetic field sweeps, the molecule relaxes from metastable state (left well) to the stable well (the right well) and releases the Zeeman energy, ΔE. This Zeeman energy is stored until the molecule relaxes, and once it relaxes, it is released through phonons that heat neighboring molecules. U is the anisotropy energy barrier. It becomes smaller as the magnetic field increases and the metastability goes down.

There are three necessary factors for the triggering of deflagration. First, there has to be some stored energy, i.e. "fuel" to be burned in the substance. For the case of magnetic avalanches, the "fuel" is the Zeeman energy $\Delta E = 2g_z\mu_B SH_z$ (see Fig. 20). This energy is stored in each molecule which is remaining in the metastable state. On average through the sample, the stored energy per molecule, $E_{stored} = \Delta E \times$(fraction of remaining molecules), can be expressed as,

$$E_{stored} = 2g_z\mu_B SH_z(M_{sat} - M)/2M_{sat}\,. \tag{5}$$

In Fig. 21, E_{stored} is plotted in brown. The values were obtained using the measured magnetization curve (solid blue curve in Fig. 15) which was taken at 0.3 K with a

sweep rate of 10 mT/s. The magnetization curve without an avalanche was used because we are investigating the condition before avalanches occur.

The second condition requires that the metastability not be too large. In other words, the energy barrier from the metastable state to the lower energy state should not be too high. For the case of magnetic avalanches, the anisotropy barrier, U in Fig. 20, corresponds to this metastability. Using the simplified spin Hamiltonian for $S = 10$,[12]

$$\mathcal{H} = -DS_z^2 - g_z\mu_B S_z H_z \,, \tag{6}$$

where $D = 0.65\,\mathrm{K}$ and $g_z = 1.94$. $U(H_z)$ (see Fig. 20), the classical energy barrier [165] can be calculated[13] as

$$U(H_z) = DS^2\left(1 - \frac{g_z\mu_B H_z}{2SD}\right)^2 . \tag{7}$$

In Fig. 21, U is plotted as a function of H_z (blue curve).

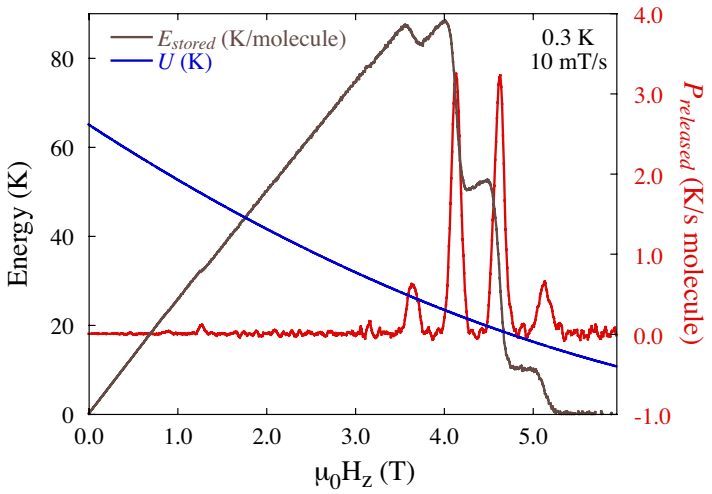

Figure 21: Three factors for triggering condition for avalanches are plotted for the magnetization curve which was taken at 0.3 K and 10 mT/s. E_{stored} (brown curve) indicates the average stored Zeeman energy per molecule and corresponds to the "fuel" in a flammable chemical substance. U (blue curve) is the calculated values of the anisotropy energy barrier and indicates the metastability of the flammable chemical substance. $P_{released}$ (red curve) is the power of heating accompanied by tunneling relaxation that can be used for "ignition" of avalanches.

[12]The results using the Hamiltonian with the higher order, AS_z^4 yielded only small differences in the result.

[13]The energy barrier can be reduced by tunneling at tunneling resonances.

The third condition is an ignition. There has to be some heat or other kind of energy released into the substance to initiate the burning process. For the case of magnetic avalanches, the only energy released in the samples during the magnetic field sweeps is the Zeeman energy which is released through phonons following the spin relaxation through tunneling (see Fig. 12). The average power of heating per molecule, which can be calculated from the measured tunneling rate using the derivative of the magnetization curve, is $\Delta E \times$(fraction of tunneling molecules per second).

$$P_{released} = 2 g_z \mu_B S H_z \frac{1}{2M_{sat}} \frac{dM}{dH_z} \frac{dH_z}{dt} \,. \tag{8}$$

$P_{released}$ is plotted (red curve) in Fig. 21 for the data taken at 0.3 K and 10 mT/s (solid blue curve in Fig. 15).

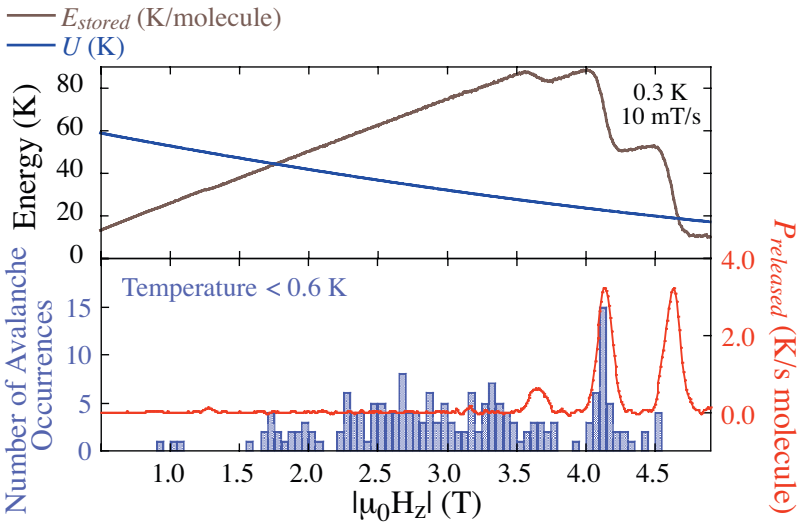

Figure 22: Three factors for triggering conditions for avalanches are plotted with the measured number of avalanche occurrences. This analysis captures the character of the actual avalanche occurrence well only above 3.5 T. The occurrences of avalanches below 3.5 T cannot be explained with this analysis since there is not enough heating ($P_{released}$ is near zero below 3.5 T). Also, the overall stochastic behavior of avalanche occurrences can not be explained.

In Fig. 21, the three factors are plotted together. The best triggering conditions are when E_{stored} is large, U is smaller, and $P_{released}$ is large. For the data used, the more likely magnetic fields for avalanches to occur are 3.6 T at the tunneling resonance

of $N = 7$ or 4.1 T at the tunneling resonance of $N = 8$. Above 4.5 T the avalanches are not likely to occur since only a small fraction of "fuel" remains. In Fig. 22, the same three factors are plotted and compared with the actual measured number of occurrences of avalanches at low temperature. Only above 3.5 T, this analysis consistents with the actual occurrences of avalanches. The occurrences of avalanches below 3.5 T cannot be explained with this analysis since there is not enough heating. In other words, $P_{released}$ is near zero below 3.5 T. We suggest that the avalanches triggered below 3.5 T must originate from defects with lower energy barriers (smaller metastability due to higher symmetry breaking for tunneling). Also the number of molecules with the defects must be small so that their magnetic relaxation is too small to be detected for the magnetization measurements. The overall stochastic nature of avalanche occurrences cannot be explained well with this analysis. Defects which are small enough might give some uncertainty for an ignition.

In Section 3.2.1, we also found that avalanches tend to occur only at lower temperatures and no avalanches were observed above 0.82 K for all samples measured. In Fig. 23, the three triggering factors during the magnetic field sweep are shown at several different temperatures. Frame (a) shows the amount of "fuel" which can be used during an avalanche for different temperatures. As expected, when the temperature is lower, a larger fraction of molecules remain at higher magnetic field. Therefore, above a certain magnetic field, avalanches are more likely to occur at lower temperature due to the large amount of "fuel" available for the burning process.

Fig. 23 (b) shows the relaxation rates of the metastable state for different temperatures. The anisotropy energy barrier, U which is plotted in Fig. 21 is temperature independent. The stability of the metastable state at different temperature can be inferred from relaxation rates. The relaxation rates were obtained using the Arrhenius' law,

$$\Gamma = \frac{1}{\tau_0} e^{-\frac{U}{K_B T}} , \tag{9}$$

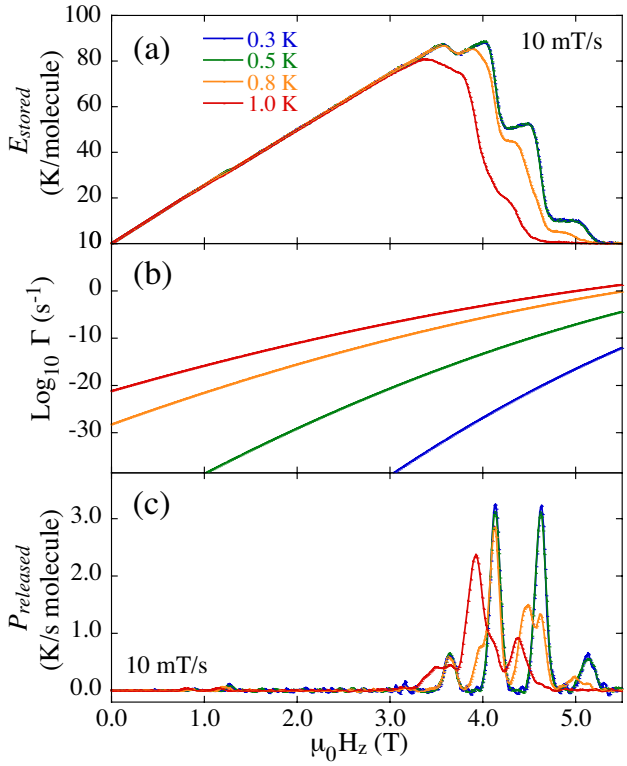

Figure 23: Three factors (a)-(c) for triggering conditions of avalanches are plotted for different temepatures. (a) shows the amount of "fuel" which can be used during an avalanche. (b) shows the relaxation rates of the metastable state. (c) shows the power of heating accompanied with tunneling relaxation. Considering all three aspects together shows that avalanches are more likely to occur at low temperature.

where τ_0 is an attempt time which we set to an approximate value of 10^{-7} s. When Γ is larger, the metastability is small; therefore, avalanches are more likely to occur. In Fig. 23 (b), Γ is much larger at higher temperature since more phonons are available to overcome the energy barrier. Therefore, avalanches are more likely to occur at higher temperature regarding "metastability". However, this effect is minimal since a small amount of energy can increase the temperature from 0.3 K to 1.0 K due to the small heat capacity in this range of temperature. Later in Section 3.3.4, the temperature of the avalanche front is estimated and it is shown that it can be as high as 27 K. In this case, the difference in the initial temperature between 0.3 K and 1.0 K is negligible.

Avalanches occur when the value of $P_{released}$ exceeds the speed of energy diffusing out of the sample, which depends on thermal diffusivity of the sample, thermal coupling between the sample & its environments, and the cooling power of the cryostat. Also, it should be mentioned that the cooling power of the cryostat is normally larger at lower temperature in our cryostat. Fig. 23 (c) shows the power of heating accompanied with tunneling relaxation for different temperatures. Large values of $P_{released}$ should ignite avalanches. At lower temperature, $P_{releaed}$ reaches higher values. Therefore, avalanches are more likely to occur at low temperature regarding "ignition". When taking all three aspects together, Fig. 23 shows that avalanches are more likely to occur at low temperature. This might explain the reason that no avalanches were observed above 0.9 K as shown in Fig. 17.

One of the reasons for smaller maximum values of $P_{released}$ at higher temperature is that there are more tunneling resonances (including many thermally excited tunneling resonances) through which the spin can relax. Therefore, the relaxation is distributed over larger number of resonances.[14] Consequently, the tunneling rate for each resonance is smaller. On the other hand, for low temperature the spin can only tunnel from the ground state, and when it does, it relaxes a large amount of magnetization at resonance. For example, in the case of Fig. 23 (c), the highest tunneling resonances are located between $\mu_0 H_z$ =3.8 and 4.3 T where the $N = 8$ resonances are. For low temperature, the spin can relax only from $m = -10$ around 4.2 T. However, as the temperature is increased, some of the molecules can also relax from $m = -9$ around 3.9 T. Consequently each of the two peaks ($m = -10$ and $m = -9$) is smaller.

The temperature dependence of the maximum value of $P_{released}$ in the previous paragraph is not always true for different temperature ranges or different sweep rates.

[14]The other reason, which has a relatively smaller effect and is always true, is that spin relaxes at smaller magnetic fields through thermally excited tunneling during a magnetic field sweep for higher temperature and $P_{released}$ is proportional to magnetic field so it is smaller for smaller magnetic fields. U is larger for smaller magnetic fields and larger U prevents avalanches from occurring.

This happens when a large amount of magnetization relaxes at one thermally assisted tunneling resonance during a magnetic field sweep. The tunneling probability at the Nth resonance from state m at the temperature, T is expressed as [46],

$$P_{N,m} = 1 - \exp\left[-\frac{\pi \Delta_{N,m}^2 e^{-\Delta\varepsilon_{N,m}/T}}{v_{N,m}\hbar}\right], \tag{10}$$

where $\Delta_{N,m}$ is the tunnel splitting, $\Delta\varepsilon_{N,m}$ is the excitation energy to state m, and $v_{N,m}$ is the energy sweep rate. Then the tunneling rate is, $R_{tunneling} = P_{N,m} M_{remaining}$ where $M_{remaining}$ is the fraction of molecules which have not yet tunneled. In order to have a resonance with large $R_{tunneling}$, both $P_{N,m}$ and $M_{remaining}$ have to be large. $M_{remaining}$ is history dependent during a magnetic field sweep. In order to have large $M_{remaining}$ at the (N, m) resonance, all the value of $P_{N',m'}$ before the (N, m) resonance have to be small. Despite a very complicated competition among all the resonances during a magnetic field sweep, the temperature dependence of $P_{released}$ as shown in Fig. 23 (c) captures the way avalanches disappear above 0.82 K well.

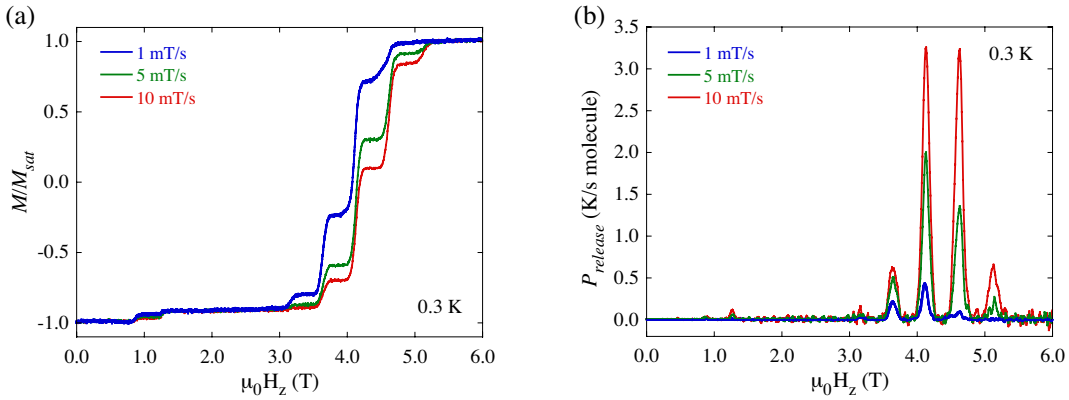

Figure 24: (b) shows magnetic sweep rate dependence of $P_{released}$. (a) shows the magnetization curves which were used to obtain $P_{released}$. As can be seen, larger sweep rates cause $P_{released}$ to reach higher values. This analysis shows that avalanches are more likely to occur during a magnetic field sweep with larger sweep rate.

In Fig. 24 (b), magnetic sweep rate dependence in $P_{released}$ is shown. (a) shows the magnetization curves which were used to obtain $P_{released}$. As can be seen, larger

sweep rates cause $P_{released}$ to reach higher values. This is partially due to the history dependence of the magnetization. The tunneling rate is determined from the product of the fraction of remaining molecules and the tunneling probability. With smaller sweep rates, some magnetization relaxes at the lower resonance with smaller tunneling probability before it reaches the higher resonance with larger tunneling probability, while with higher sweep rates, only a small fraction of magnetization relaxes at the lower resonances and ample magnetization is left to relax at the higher resonance with larger tunneling probability and also higher Zeeman energy. A distribution of tunnel splittings (see Section 2.2) also causes $P_{released}$ to reach higher values for higher sweep rates. Unlike the relaxation with a single value of the tunnel splitting, a distribution of tunnel splitting makes relaxation slower than exponential as time goes on. This analysis shows that avalanches are more likely to occur during a magnetic field sweep with a larger sweep rate. Not enough data for sweep rate dependence has been accumulated to prove this. More measurements on avalanches with different magnetic field sweeps are shown Section 3.2.4. In Ref. [163], reproducible avalanches occurred, and with faster magnetic field sweeps avalanches occurred at smaller magnetic fields at the beginning of the tunneling resonance.

3.2.3 Sweep Measurements at Different Angle

All the data in Fig. 17 were taken with a constant magnetic field sweep rate along the easy axis ($\theta = 0$ in Fig. 25). This section describes the effect on threshold temperature for sample B when the angle between the magnetic field and the easy axis of the crystal is varied . No avalanches occurred above 0.82 K when the magnetic field was swept along the easy axis with sample B as shown in Fig. 17. Whether avalanches could occur at temperatures higher than 0.82 K when $\theta > 0$ in Fig. 25 during a magnetic field sweep is the main topic of this investigation.

These measurements were preliminary experiments for the bolometer measurements shown Fig. 13 for which we did not monitor the magnetization but rather only monitored the response of the bolometer.[15] The bolometer measurements were possible only above 1.6 K. Therefore, we only needed to determine the optimal configuration for avalanches at high temperatures. These angled magnetic field sweep measurements were not performed at lower temperatures. Fig. 26 shows hysteresis curves with the magnetic field swept at the angles of 0°, 20°, 30°, 40° and 60° with respect to the easy axis with the magnetic field sweep rate of 12 mT/s at temperatures around 1.1 to 1.2 K.[16] Please note that the temperatures at 0° and 60° were slightly higher than the other angles. In Fig. 26 (a), the hysteresis curves are plotted as a function of the total magnetic field, $\mu_0 H$ while in (b), the same hysteresis curves are plotted as a function of the component of the magnetic field along the easy axis, $\mu_0 H_z$.

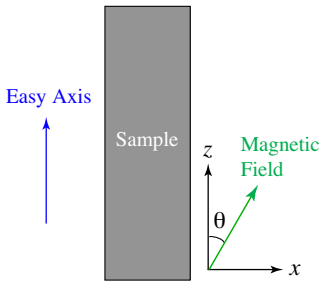

Figure 25: The magnetic field was swept at different angles, θ with respect to the easy axis. In this experiment, $dH/dt = 12\,\mathrm{mT/s}$; yielding $dH_z/dt = \cos\theta \cdot 12\,\mathrm{mT/s}$ and $dH_x/dt = \sin\theta \cdot 12\,\mathrm{mT/s}$.

Fig. 26 (a) shows complicated crossings in the magnetization curves at different angles. This is because magnetization relaxation depends both on the longitudinal

[15]Sample B is a single crystal. Many crystals which were glued together were used for the measurements in Fig. 13 and also used in Ref. [154–156] for avalanche measurements which occurred above 1.6 K.

[16]The setup for the angle measurements use in section is shown in Fig. 81 (b) in which ϕ indicates the rotating angle. Please also note that the signal came mainly from the M_z component (the magnetization along the easy axis), but a small M_x component (magnetization in hard plane) might present in the signal. The signal from M_x should be almost proportional to $\mu_0 H_x$. In Fig. 26 and the others, the linear components have been subtracted.

magnetic field, $\mu_0 H_z$ and the transverse magnetic field, $\mu_0 H_x$. In this range of magnetic field, $\mu_0 H_z$ would bring the anisotropy energy barrier lower (the Zeeman energy difference between the stable well and metastable well as seen in Fig. 12), and $\mu_0 H_x$ increases the symmetry breaking which makes tunneling faster (the strength of the tunneling, the thickness of the purple arrows in Fig. 12) [165–167]. When sweeping the field at an angle, both components $\mu_0 H_z$ and $\mu_0 H_x$, are swept; our experimental conditions did not allow their independent control. Fig. 26 (b) shows the hysteresis curves plotted as a function of $\mu_0 H_z$ at different angels. For angle, θ=0, there is no transverse field[17]. In this temperature range, mainly thermally-assisted tunneling proceeded. For $\theta = 20°$ to 60°, the transverse field, $\mu_0 H_x = \mu_0 H \sin\theta$ was also present and gave faster magnetic relaxations. Therefore, for larger θ, the magnetization relaxed and saturated at the smaller $\mu_0 H_z$.

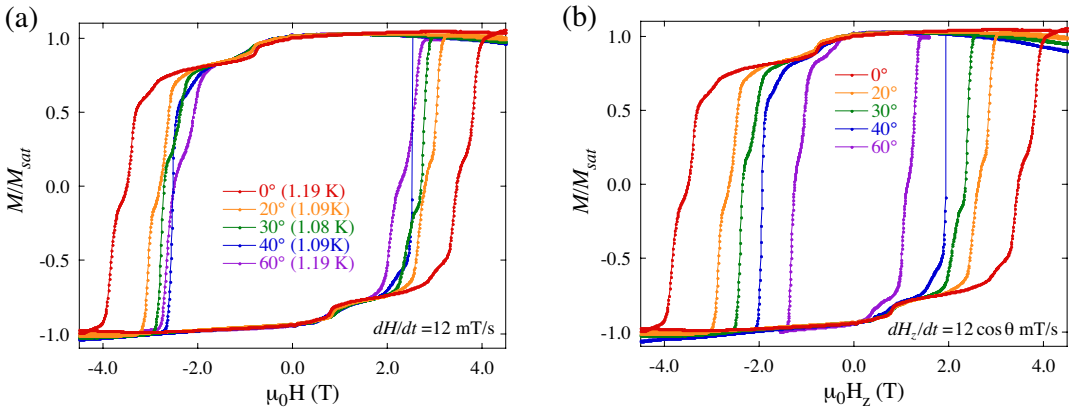

Figure 26: The magnetic field was swept at $\theta = 0°$, 20°, 30°, 40° and 60° with respect to the easy axis at temperatures around 1.1 K.[18] Please note that at these temperatures thermally-assisted tunneling rather than ground-state tunneling dominates the spin relaxation at the different resonant magnetic fields. The magnetic field was swept at 12 mT/s. **(a)** The hysteresis curves are plotted as a function of the total magnetic field, $\mu_0 H$. **(b)** The same hysteresis curves are plotted as a function of the component of the magnetic field along the easy axis, $\mu_0 H_z$. Sample B is a large single crystal and apparently contains a somewhat larger amount of the second species as is often true for larger crystals.

[17]The internal fields ($\leq$ 1000 Gauss) and small external magnetic field from misalignment ($\leq 3° \rightarrow \leq$ 2000 Gauss at $\mu_0 H = 4$ T) were always present for the transverse magnetic field.

[18]The temperatures at 0° and 60° were slightly higher than the other angles.

In Fig. 26 (b), an avalanche occurred around $\mu_0 H_z$=1.9 T when the sample was oriented at 40°. In Fig. 27, hysteresis curves with the magnetic field sweep at 40° were plotted for different temperatures. Fig. 27 (a) shows the full hysteresis, and Fig. 27 (b) shows enlargement of the data near an avalanche for $\mu_0 H$ >1.8 T where avalanches occurred for the two lowest temperatures of 0.98 K and 1.09 K at the fixed magnetic field in the middle of tunneling resonance. This behavior resembles avalanches above 1.6 K in Ref. [154–156]. In Fig. (1) of Ref. [155], the magnetic field at which an avalanche occurred also increased as the temperature was raised.

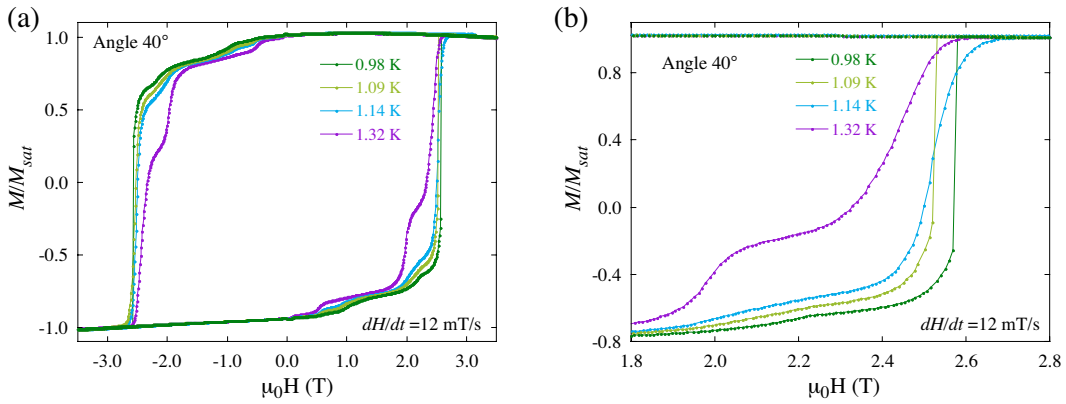

Figure 27: The magnetic field at an angle of 40° with a respect to the easy axis was swept for different temperatures. **(a)** The full hysteresis curves. **(b)** The enlargement of the data for $\mu_0 H$ >1.8 T. Avalanches occurred for the two lowest temperatures of 0.98 K and 1.09 K at the middle of tunneling resonance.

In Fig. 28, hysteresis curves with the magnetic field sweep at 20° and 30° were plotted for different temperatures. As can be seen in Fig. 28 (a), at 20°, stochastic behavior remained with avalanches occurring at various magnetic fields on and off resonance. The threshold temperature for 20° is between 0.8 K and 1.09 K. In (b), at 30°, avalanches occurred only on the tunneling resonance, and this behavior is similar to the one at 40°. The threshold temperature for 30° is between 0.98 K and 1.08 K. Unfortunately we did not take data at lower temperatures so we do not know whether it is stochastic as the temperature is reduced down to 0.3 K at $\theta = 30°$ and 40°.

From the data which we obtained so far, the threshold temperatures were estimated as ∼0.8 K for 0°, 1.03 K for 30° and 1.09 K for 40° with a magnetic sweep rate of 12 mT/s (see Fig. 29). In Fig. 26, avalanches did not occur at 60°. This suggests that there is a maximum for the threshold temperature near or between 40° and 60° (dashed line in Fig. 29). Higher threshold temperatures should result from the better conditions for avalanches. In Fig. 30, $P_{released}$ in Eq. 8 was calculated for different angles using the magnetization curves shown in Fig. 26. $P_{released}$ indicates the energy release rate caused by relaxation through tunneling. When this is high, there is a higher probability for avalanches to be triggered. The magnetic field sweep at 40° reaches the highest value. This is consistent with the result in Fig. 29.

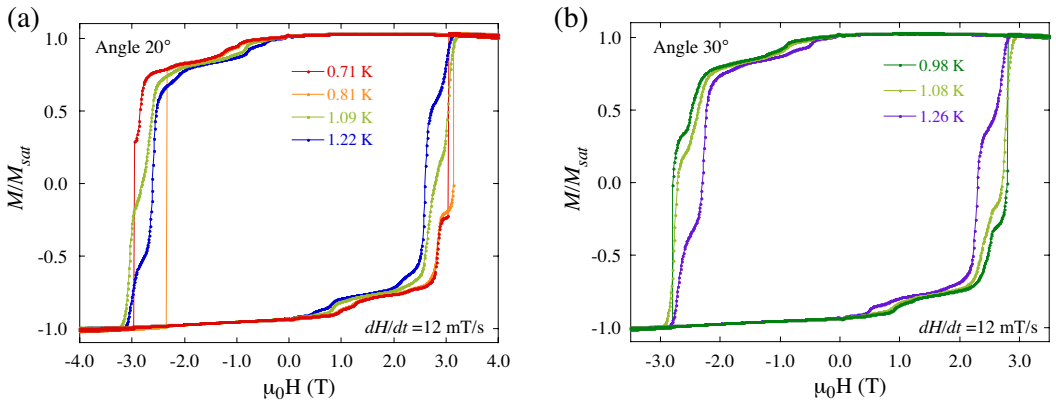

Figure 28: **(a)** The magnetic field was swept at an angle of 20° with respect to the easy axis for different temperatures. **(b)** The magnetic field was swept at an angle of 30°

The avalanches around the threshold temperature at 30° and 40° occurred only at the tunneling resonance and they were quite reproducible.[19] On the other hand, at 0° and 20° below the corresponding threshold temperatures, avalanches occurred in a stochastic way; i.e. the magnetic field at which an avalanche occurred was different every time and it was not at a tunneling resonance. In the previous chapter,

[19]Please note that this measurement was performed only on sample B once and has not been confirmed with other samples. This is just a speculation for future studies which might lead to more understanding on the mechanisms of self-triggering of avalanches with Mn_{12}-acetate.

Section 3.2.1, it was suggested that avalanches below 3.5 T in Fig. 18 may be due to defects in the crystal.

For example, consider that a small part (as small as of few hundred molecules for example) of the sample crystallized so that its easy axis is tilted by some angle relative to remaining molecules (see Fig. 31). The magnetic field is then applied along the crystal c-axis which is the easy axis of the majority of the molecules. Therefore, the magnetic field is at some angle (for example, $\theta = 30°$ to $40°$) relative to the easy axis of the small part. The molecules in the tilted part would have magnetization relaxation through tunneling at smaller magnetic fields. This can be seen by examining the data shown in Fig. 26 which clearly shows that the magnetization relaxes at smaller fields as the tilt angle inreases. In this case, a small part of the magnetization of the sample relaxes at a smaller field leading to avalanches occurring below 3.5 T.[20]

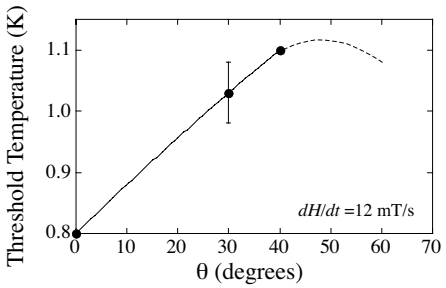

Figure 29: The estimated threshold temperatures were plotted for $\theta = 0°$, $30°$ and $40°$. As seen in Fig. 26, avalanches did not occur at $60°$. This suggests that there is a maximum for the threshold temperature near or between $40°$ and $60°$ (dashed line).

Moreover, the reason that sweeping magnetic field at some angle is favorable for triggering avalanches is following. The probability of an avalanche event increases as the size of the nucleation event increases. To maximize the size of the nucleation event, the number of molecules participating must be maximal – which corresponds to reducing the amount of tunneling that occurs during lower field resonances. This is easily achieved by using a small transverse field at at low longitudinal fields and

[20]Please note that the measurement was done around 1.1 K which is higher temperature than the ones in Fig. 18.

large transverse field at large longitudinal field. An increasing transverse field occurs naturally when the field is swept for a sample held at an angle relative to the sweeping field. For fixed total field sweep rates, as the angle between the field and the easy axis of the crystal increases, the longitudinal sweep rate is reduced and the transverse sweep rate increases. Increasing the transverse field significantly increases the probability of tunneling between the resonances.

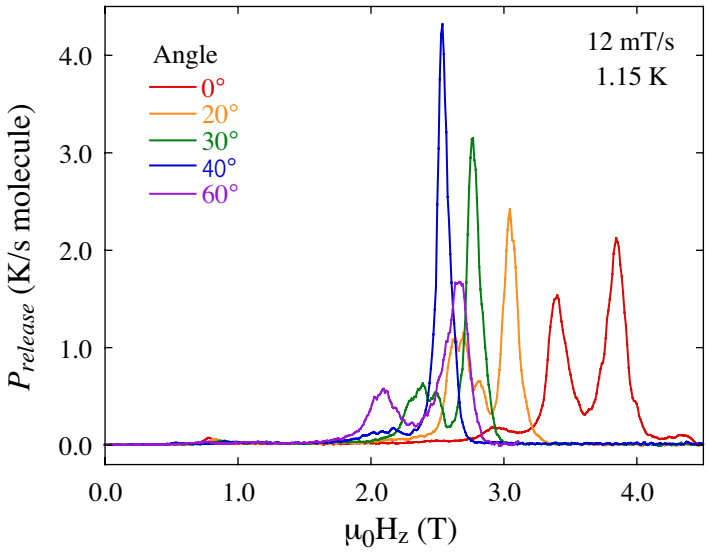

Figure 30: $P_{released}$ in Eq. 8 was calculated for different angles using the magnetization curves shown in Fig. 26. $P_{released}$ indicates the energy release rate caused by relaxation through tunneling. When this is high, there is a higher probability for avalanches to be triggered. The magnetic field sweep at 40° reaches the highest value. This is consistent with the result in Fig. 29.

The probability of tunneling, $P_N = 1 - \exp\left(-\pi\Delta_N^2/v\hbar\right)$, where Δ_N is the tunneling splitting, N is the resonance number and v is the energy sweep rate. For a field swept at an angle, $v \sim dH_z/dt$ and $\Delta_N \sim (g_x\mu_B H_x/2D)^{2S-N}$, where D is the anisotropy constant and $S = 10$. Normally, $g_x\mu_B H_x \ll 2D$. The tunneling probability is a strong function of the tunnel splitting where the tunnel splitting itself grows as the power of N. Therefore, the tunnel splitting increases by a large amount from Δ_n to Δ_{n+1}, between the resonance, $N = n$ to the adjacent resonance, $N = n + 1$.

With the magnetic field swept at the angle, $\theta \neq 0$, H_x (which is the base of the exponential dependence of Δ) also increases as N increases. Consequently Δ_N has an even stronger dependence on N for larger θ. While the value of dH_z/dt decreases at larger angles for constant dH/dt, P_N has much weaker dependence on dH_z/dt which is also independent of θ.

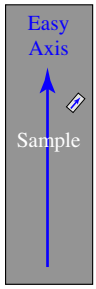

Figure 31: A small part of the sample (light gray) which is tilted relative to the easy axis could be the source of a locally large $P_{released}$. This part of the sample can trigger avalanches below 3.5 T. From the stochastic nature of the avalanche occurrences, the defects have to be small enough to give some uncertainty for triggering and there have to be many of them.

With the magnetic field swept at 40° in Fig. 27, avalanches probably tend to nucleate in the normal molecules rather than defects which are tilted away from the normal molecules. Therefore the process should be more reproducible and occur at the tunneling resonance measured in the data for the bulk measurements as seen in Fig. 27. This needs to be confirmed by measurements down to lower temperatures on other samples. Please again note that this measurement was performed only on sample B once and has not been confirmed with other samples. This is just a speculation for future studies which might lead to a better understanding of the mechanisms of self-triggering of avalanches with Mn_{12}-acetate.

3.2.4 Measurements in Non-linear Sweeps

So far, the magnetic field has been swept at (different) constant rates. The effect of sweeping the field at different (constant) rates on triggering avalanches was not clear within the statistics which we have accumulated. In this section, non-linear

sweeps were applied to sample D.[21]. Sample D was about 0.4 mm in length along the easy axis. It contained a somewhat larger (∼10 %) than usual amount (∼5 %) of the second species.

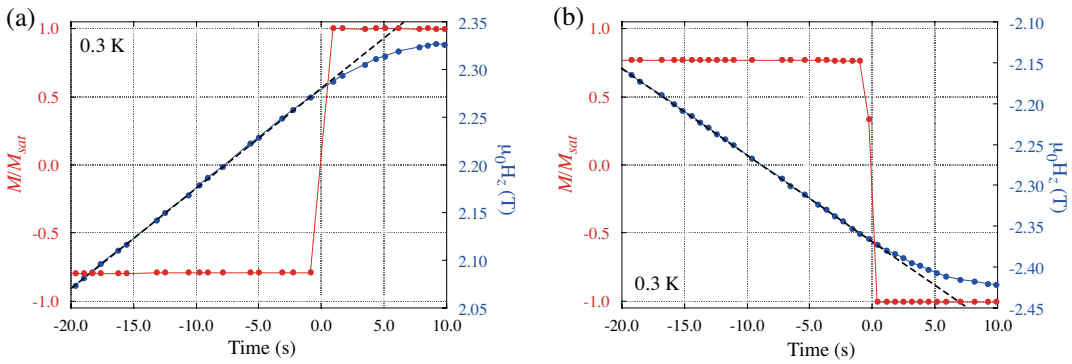

Figure 32: **(a)** Normalized magnetization, M/M_{sat} (red curve) and the external magnetic field, $\mu_0 H$ (blue curve) are plotted as a function of time. Here sample D was prepared to have magnetization at negative saturation, and the magnetic field was swept upward along the easy axis at 10 mT/s. Around $\mu_0 H_z = 2.27$ T, the rate of change of the magnetic field was reduced (decelerated). An avalanche occurred as soon as the magnetic field sweep started to slow down. **(b)** Sample D was prepared to have magnetization at negative saturation, and the magnetic field was swept upward along the easy axis at 10 mT/s. Around $\mu_0 H_z = -2.37$ T, the rate of change of the magnetic field was reduced (decelerated). An avalanche also occurred as soon as the magnetic field sweep started to slow down. The temperature of the sample place was kept at 0.3 K. The sampling rate of the measurements was about 1 Hz.

In Fig. 32, at 0.3 K, sample D was first magnetized by ramping the field along the easy axis to -6 T in part (a) and 6 T in part (b). The magnetic field was then swept in the opposite direction at a rate of 10 mT/s down to $\mu_0 H_z = 2.27$ T in part (a) and up to $\mu_0 H_z = -2.37$ T in part (b). In both cases after the field reached the set magnetic fields, the rate of change of the magnetic field was reduced (decelerated). As evidenced in Fig. 32, an avalanche occurred as soon as the magnetic field sweep started to slow down.

In Fig. 33, an avalanche also occurred with a constant magnetic field of -2.29 T. At 0.3 K sample D was magnetized to positive saturation, and the magnetic field was

[21]Please note that these measurements were not performed on other samples. These results can be sample dependent.

swept along the easy axis with a time dependence shown by the blue curve in Fig. 33 (a), whereby the sample underwent periods of linear magnetic field sweeps followed by periods of fixed fields.[22] About one minute after stopping the field sweep at -2.29 T, an avalanche occurred. An enlargement of the data is shown in (b). Another attempt was made at 2.30 T, but after waiting one hour an avalanche still had not occurred.

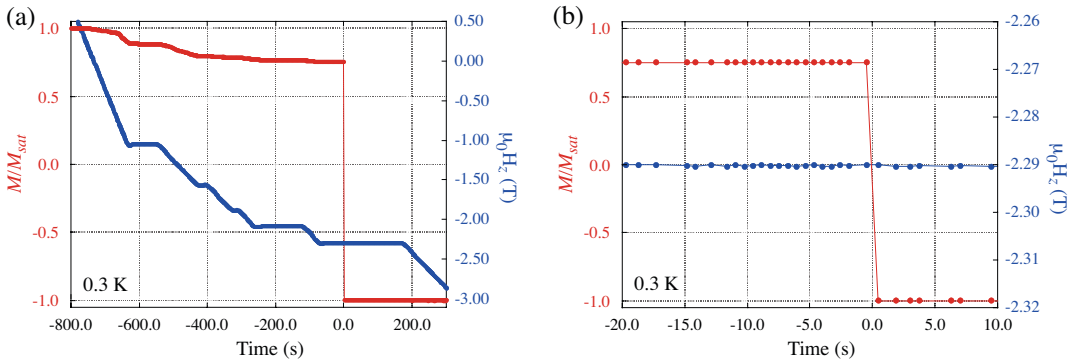

Figure 33: **(a)** Normalized magnetization, M/M_{sat} (red curve) and the external magnetic field, $\mu_0 H_z$ (blue curve) are plotted as a function of time. First, sample D was prepared to have magnetization at positive saturation, and the magnetic field was swept downward along the easy axis little by little with many sets of linear sweeps (10 and 5 mT/s were used for the sweep rates) and breaks. Around -70 s in time for x-axis, the magnetic field was kept at the constant value of -2.29 T for a while. About one minute later, at 0 s in x-axis, an avalanche occurred. **(b)** The enlargement of the avalanche event in constant magnetic field is shown. The temperature of the sample was kept at 0.3 K. The sampling rate of the measurements was about 1 Hz.

Changing the sweep rate appears to affect the probability for triggering avalanches. Aside from effects associated with changing the rate at which the field is swept, there are consequences that derive fom sweeping slowly rather than fast. If one assumes that avalanches are triggered thermally and the heat derives from the magnetization relaxation via tunneling, the best condition for triggering an avalanche would be sud-

[22]The reason that the magnetic field was swept downward little by little was to avoid an avalanche triggered by deceleration as occurred in Fig. 32. Actually the behavior in Fig. 32 was discovered trying to conduct the measurements in Fig. 33. If the magnetic field was swept with 10 mT/s (or 5 mT/s) in one step and decelerated to achieve a constant magnetic field above 2 T, an avalanche always occurred as soon as the magnetic field was slowed down as seen in Fig. 32. It is unknown why sweeping the magnetic field little by little, as for the blue curve in Fig. 33 (a), prevented an avalanche from being triggered immediately by deceleration of the magnetic field.

den heat release by relaxation, while much of the magnetization is still remaining to be relaxed. As in Fig. 10, the larger the magnetic sweep rates, the larger the fraction of molecules that remain without relaxing by tunneling. According to Fig. 24, the heat release rate, $P_{released}$ is also larger when the sweep rate is larger. Fast magnetic field sweep is good for both sudden heat release (large $P_{released}$) and many remaining molecules. Therefore, reducing the magnetic field sweep rate is not favorable for triggering avalanches.

In Fig. 32, the deceleration of magnetic field sweep clearly triggered an avalanche. This happened repeatedly above 2 T with sample D. The cause of this remains unknown."

It is also very interesting that deceleration of the magnetic field sweep did not trigger an avalanche when the magnetic field was swept slowly with many breaks in smaller fields prior to the deceleration above 2 T, as seen in Fig. 33. An avalanche occurred also in a constant magnetic field after some time. This would give us further evidence for the stochastic nature of the nucleation process of the avalanches. In any case, more investigation is needed before for any conclusion can be drawn.

3.2.5 Discussion

If avalanches are simply thermally triggered and if the heat comes from the magnetization relaxation via tunneling, then the best condition leading to an avalanche would be the sudden relaxation of a locally concentrated set of molecules (nucleation event) while much of the magnetization is still remaining to be relaxed. In other words, a local "spark" (point heat source) with a lot of "fuel" to burn. In this case, magnetization relaxation through tunneling would provide a "spark" since the tunneling events are always followed by the release of the Zeeman energy, while the remaining magnetization is the "fuel". Therefore avalanches are expected to occur at the tunneling resonances.

The most puzzling part, as can be seen in Fig. 18, is that below 3.5 T a large number of avalanches did not occur during any of the tunneling resonances, but rather occurred where there was almost no relaxation by tunneling. One possible explanation for these avalanches may be the presence of small defects in the crystal structure. Small defects may exist even though they can not been seen in the measurements for the bulk magnetization. Any kind of defect in the molecules, in most cases, would bring additional symmetry breaking and increase the tunneling probability. Therefore, the spin can flip much more easily at smaller magnetic fields (an example is shown in Section 3.2.3).

If there is a localized concentration of defects, then the process should be reproducible since there will be a strong probability that the phonons will be released during tunneling from these particular molecules which will subsequently trigger an avalanche. However, for most of the samples reported here, the fields at which avalanches are observed occur stochastically with a non-uniform distribution density. This could be because these defects are very small (consisting of few hundred molecules for example), but there are many defects distributed in the sample. Our time-resolved studies presented in Section 3.3 indicate that the avalanches propagate with speeds well below the speed of sound, and are analogous to chemical burning, or "deflagration". One can imagine a scenario in which there are many small sparks from these defects during the field sweep, and an avalanche occurs when one or a bunch of them probabilistically ignites a fire.

This distributed microdefect model is consistent with the absence of avalanches above 3.5 T in the range between the tunneling resonances; because above 3.5 T the molecules with defects will have already tunneled, leaving only the normal molecules available to trigger an avalanche. However, avalanches were still not reproducible and they are distributed probabilistically over the tunneling resonances above 3.5 T. We still do not know what causes this kind of uncertainty. This must originate from some

kind of a self-organized critical phenomenon as Paulsen, *et al.* originally suggested [126]. This needs to be investigated further and compared to other self-organized critical behaviors such as the "sandpile" model [168] or "forest-fire" model [169].

In this section, self-triggering conditions with (or without) a swept magnetic field were studied and possible involvement of defects for stochastic triggering was speculated. As described in Section 3.2.2, "fuel" and "ignition", two of the factors necessary for triggering avalanches, do not necessarily come from the same parts of the samples. For the most effective way to trigger avalanches, the large part of the samples with a large metastable barrier[23] should play a role of "fuel", and only a very small fraction of the sample, which has lower metastability, is needed for "ignition".

Normally, in explosive materials, the defects (so-called "hot spots") play essential roles [170–172]. Energetic materials (propellants and explosives) are useful and less dangerous, if they are stable before an intentional ignition. However, if they are too stable, ignition itself could be very difficult. For example, if an explosive solid is compressed, in a perfect crystal, adiabatic compression occurs, and it will not explode until it is compressed further. With defects, during compression, energy is released in a form of friction and it heats up the region (therefore they are called "hot spots"). If enough heat is released, it will trigger combustion. Therefore, the size and density of "hot spots" determine the stability of the materials. Too many "hot spots" will result in unstable explosives. On the other hand, if the "hot spots" are too small, the temperature of "hot spots" would not become high enough to activate the rest of the material.

Regarding the "ignition" condition, magnetic field sweeps applied to Mn_{12}-acetate can be analogous to a compression of energetic materials.[24] Mn_{12}-acetate would release heat through magnetic relaxation, while energetic materials released heat

[23] it needs to be stable so that it would remain the energy until the ignition is applied.

[24] Other aspects are not analogous. Mn_{12}-acetate stores energy only from the magnetic field, while energetic materials already have chemical energy stored before compression.

through friction or chemical decomposition. Heat is first released from the defects, but if it is compressed too slowly (or with slow magnetic field sweep), there is enough time for the heat to escape without raising the temperature, and it will not ignite. It is, therefore, interesting to study the relationship between size and density of defects for the triggering of avalanches.

3.3 Propagation of Avalanches

In the measurements presented in Section 3.2, the magnetization of the bulk sample was measured with a slow sampling rate. It was fast enough to obtain the magnetic field values and the temperatures at which avalanches were triggered. In order to further investigate the avalanches, we needed to acquire higher time and spatial resolution for the measurements. If avalanches originate locally, local time-resolved measurements would give us information about where they are triggered and how they propagate. In Section 3.3.1, the experimental setups for these measurements are shown. In Section 3.3.2, calculations are presented for a uniformly magnetized sample that relate the transverse magnetic fields detected by the Hall bars placed at different positions along the easy axis, to the longitudinal, easy-axis magnetization that generates these fields; good fits can be obtained with the measured data by adjusting geometric parameters and assumptions concerning discontinuities at the ends. When avalanches occur, the magnetization is no longer uniform in the samples as will be described in Section 3.3.3. The data are analyzed further in Section 3.3.4. Some

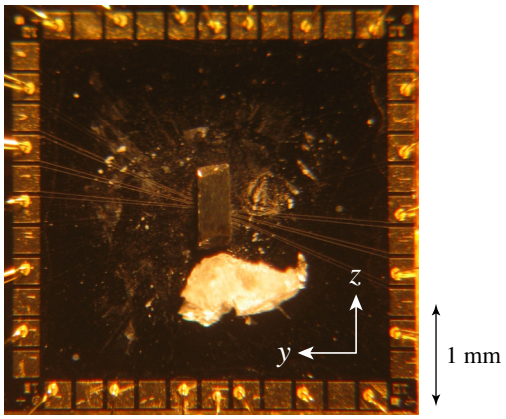

Figure 34: Sample #1 is mounted on a array of eleven Hall sensors with the easy axis along the z-axis. The sensors are evenly spaced along the z-axis. The active surface is in the yz plane with a current of $2\,\mu$A along the z-axis. The Hall voltage along the y-axis was measured for each sensor. The white chunk below the sample is "Eicosane" wax. It was later melted at a temperature just above room temperature to glue and seal the sample on the Hall sensor chip surface (see Section 4.3.1).

of these results were published in Ref. [173].

3.3.1 Experimental Setups

Microscopic arrays of Hall bars (shown it Fig. 34) provided by Zeldov's group at the Weizmann Institute (see Section 4.2) were used to measure the magnetization of three single crystals of Mn_{12}-ac of dimensions: $0.29 \times 0.29 \times 0.64\,\mathrm{mm}^3$ (sample #1), $0.28 \times 0.28 \times 1.44\,\mathrm{mm}^3$ (sample #2), $0.24 \times 0.24 \times 1.02\,\mathrm{mm}^3$ (sample #3). These crystals were provided by the group of G. Christou of UFL and the group of D. N. Hendrickson of UCSD (see Section 4.3.1). Eleven Hall bars of dimensions $10 \times 10\,\mu\mathrm{m}^2$ with $30\,\mu$m intervals were used for sample #1, and $30 \times 30\,\mu\,\mathrm{m}^2$ with $130\,\mu$m intervals for samples #2 and #3. Fig. 35 shows sample #1 mounted on the Hall sensor chip.

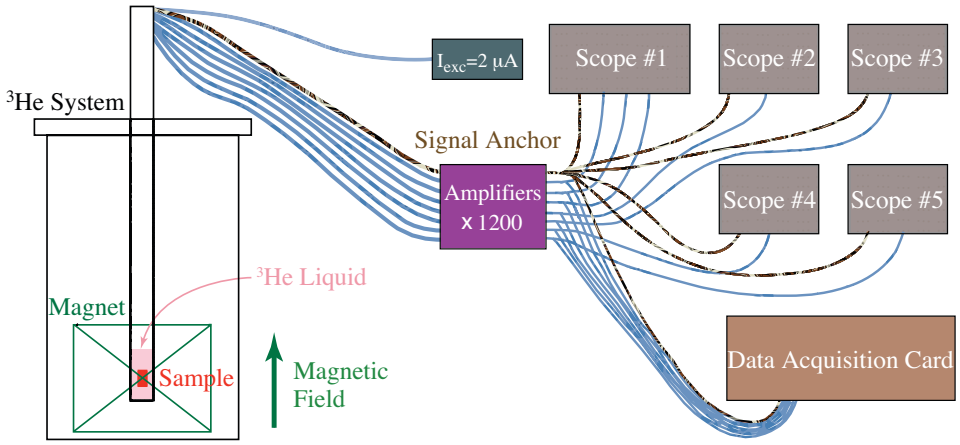

Figure 35: The samples were immersed in liquid ^{3}He (see Section 4.1). The signal was amplified by a factor of 1200, and detected and recorded by several digital scopes and a data acquisition card. In order to ensure proper synchronization, one channel of each scope was anchored to the same signal.

Using an excitation current of $2\,\mu$A, the Hall bar signal was amplified by a factor of 1200 (see Section 4.3.3), and detected and recorded by several digital scopes and a data acquisition card (see Section 4.3.4). In order to ensure proper synchronization, one channel of each scope was anchored to the same signal, as shown in Fig. 35. The Hall sensor and amplifier introduced combined delays of up to $2\,\mu$s. A magnetic

field was applied in the z-direction along the crystal easy axis. The Hall sensors were aligned to detect the magnetic induction of the sample in the x-direction. More details regarding the Hall sensor signals will be described in the next section. The samples were immersed in liquid ^{3}He (see Section 4.1); most of the data were obtained at the base temperature of 0.3 K.

3.3.2 Local Magnetization Measurements

First, without tedious calculation, let us consider what kind of information we can glean from the Hall sensor signals. The easy axis of the sample is always placed along the z-axis. Due to the high anisotropy energy barrier (without a large external magnetic field in the xy plane), the spin is forced to point either up or down along the z-axis. Fig. 36 (a) shows a schematic diagram of the approximate magnetic dipole field lines (red arrows) for a uniformly magnetized sample.[25]

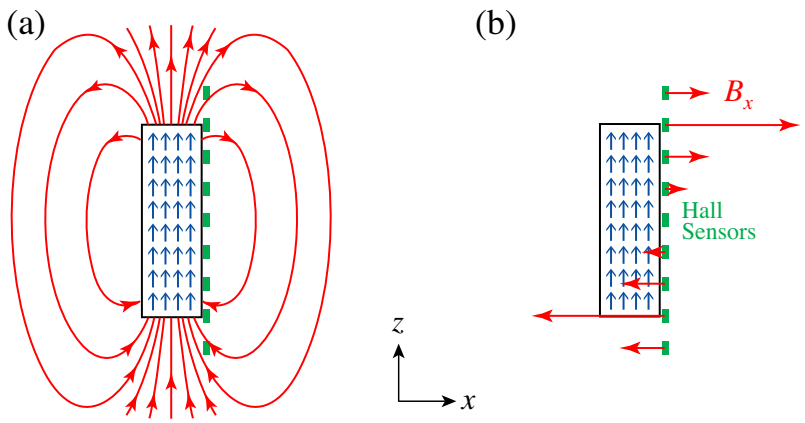

Figure 36: **(a)** In this schematic diagram, magnetic dipole field lines (red lines) are drawn around a sample that is uniformly magnetized along the z-axis. **(b)** B_x is the x component of the magnetic field at the different positions where the Hall sensors are located. The Hall sensors are oriented to pick up only B_x. B_x is antisymmetric about the middle of the sample along the z-axis and is largest at the ends of the sample.

The Hall sensors were placed along the z-axis and the active surface lies in the yz plane. Therefore, the Hall sensors are only sensitive to the magnetic field in the

[25] Crystals of Mn_{12}-acetate have one long axis which is also the easy axis, and have almost rectangular cross section except at the ends (see Section 4.3.1).

x direction, and the signal is proportional to B_x (see more details in Section 4.2). In Fig. 36 (b), the x-component of the dipole field is shown for each Hall sensor. B_x is largest at the ends and antisymmetric about the middle of the sample along the z-axis. Therefore, when changes in uniform magnetization were probed, a Hall sensor was placed close to the end of the sample for maximum sensitivity.

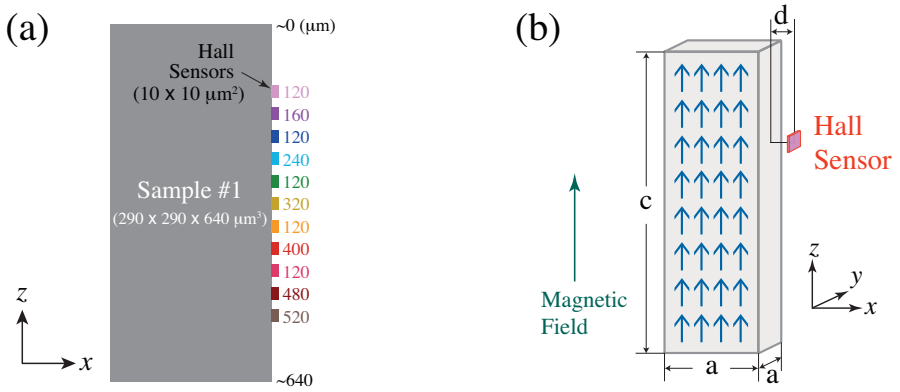

Figure 37: **(a)** Schematic diagram of sample #1 mounted on an array of Hall sensors used to detect B_x. The sensors are labeled by the approximate distance from the top of the sample. **(b)** The parameters used in Eq. 12, where c is the sample length, a is sample thickness, d is the distance between sample and Hall sensor, and z is the Hall sensor position along z-axis, for a perfectly rectangular shaped sample.

Fig. 37 (a) shows a schematic diagram of sample #1 mounted on an array of Hall sensors used to detect B_x. As can be seen in Fig. 34, the sample did not have square ends at the top and bottom. Using the mean of each of the end points, the sample length was determined to be 640 μm. The sensors are labeled by the approximate distance from the top of the sample to the center of each sensor. The hysteresis curves at seven positions measured at a temperature of 0.3 K and an external magnetic field sweep rate of 10 mT/s are plotted in Fig. 38. An avalanche did not occur during either the upward or downward sweep of the magnetic field. Therefore, the spin relaxed through controlled tunneling at constant temperature of 0.3 K. The position dependence of B_x was as we expected for the geometry shown in Fig. 36 (b). The flat response of the sensor at 320 μm indicates that it was located at the middle

of the sample. The magnetization is approximately uniform for quasi-equilibrium conditions.

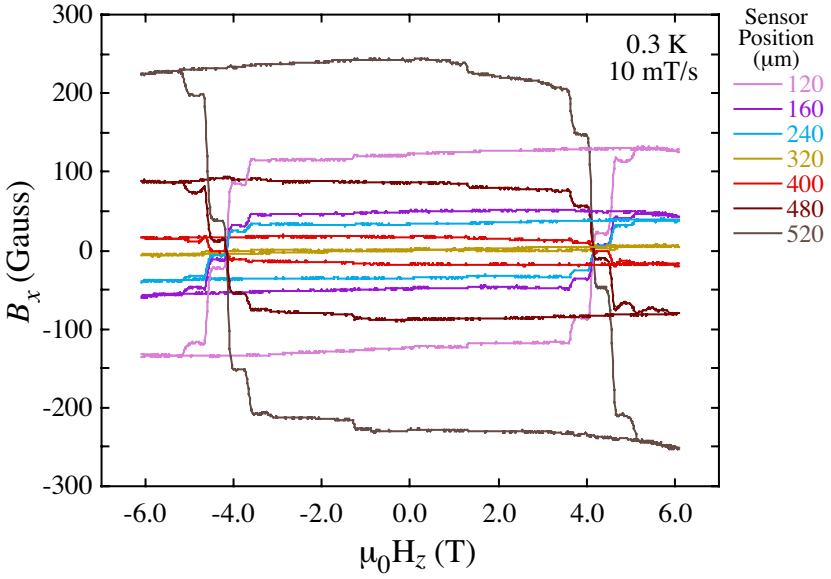

Figure 38: The hysteresis curves measured by seven sensors at the positions between 120 and 520 μm.[26] Sample #1 was mounted on an array of Hall sensors as in Fig. 37 (a), and at 0.3 K a magnetic field was swept at 10 mT/s along the z-axis .

In Fig. 39, the hysteresis curves for all the sensors (except 320 and 400 μm) in Fig. 38 were scaled with B_x/B_{sat} where B_{sat} is the saturation values for the hysteresis curves for each sensor position. Small deviations of B_x/B_{sat} from exact superposition for the sensors at the middle of the sample (160 μm and 240 μm) are within the error and sensitivity of the Hall sensors; the measured values of B_x were small and divided by small values of B_{sat} for these sensors, leading to large uncertainties. Small non-monotonicity in B_x (it might look large in B_x/B_{sat}) at the beginning and end of tunneling resonances indicates small non-uniformity during the resonances due to slightly different tunneling resonant fields [174].

[26]The measured (sensitivity of) Hall voltages were smaller here than the previous sections because all the sensors were further away from the ends.

B_x also can be calculated easily for a sample with a perfect rectangular shape for uniform magnetization [174]. In Mn_{12}-acetate crystals, the magnetization is oriented along the z-axis. Assume M_z has a finite value within the sample while $M_z = 0$ outside of the sample and $M_x = M_y = 0$ everywhere. In general, the magnetic dipole field in x due to the magnetization along the z-axis can be determined regardless of sample shape, and is expressed as:

$$B_x(\vec{r}) = -\int \frac{3(z-z')(x-x')}{|r-r'|^5} M_z(\vec{r}) d^3r' \,. \tag{11}$$

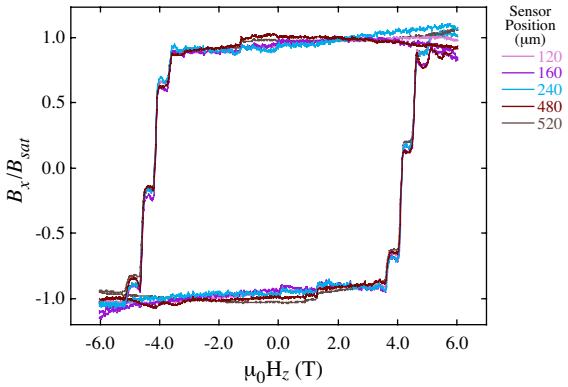

Figure 39: The hysteresis curves for all the sensors (except for the sensors, which were located too close the middle of the sample, at 320 and 400 μm) in Fig. 38 were scaled with B_x/B_{sat}, where B_{sat} is the saturation values for the hysteresis curves for each sensor position. Small deviations B_x/B_{sat} for the sensors near the middle of the sample (160 μm and 240 μm) are within the error and sensitivity of the Hall sensors; the measured values of B_x were small and divided by small values of B_{sat} for these sensors, leading to large uncertainties. Small non-monotonicity in B_x (it might look large in B_x/B_{sat}) at the beginning and end of tunneling resonances indicates small non-uniformity during the resonances due to slightly different tunneling resonant fields [174].

Assuming a perfectly rectangular shaped sample without magnetization dependence in the x-y plane within the sample and using the parameters in Fig. 37 (b), this volume integral can be reduced to:

$$B_x(z) = \int F(z-z') \frac{\partial M_z(z')}{\partial z} dz', \tag{12}$$

where

$$F(z-z') = \log \frac{(a-\sqrt{a^2+d^2+(z-z')^2})(a+\sqrt{a^2+(a+d)^2+(z-z')^2})}{(a+\sqrt{a^2+d^2+(z-z')^2})(a-\sqrt{a^2+(a+d)^2+(z-z')^2})}\,. \quad (13)$$

$B_x(z)$ indicates the x-component of the magnetic filed at $(x, y, z) = (a/2 + d, a/2, z)$ with the origin of coordinates in the middle of the sample in Fig. 37 (b).

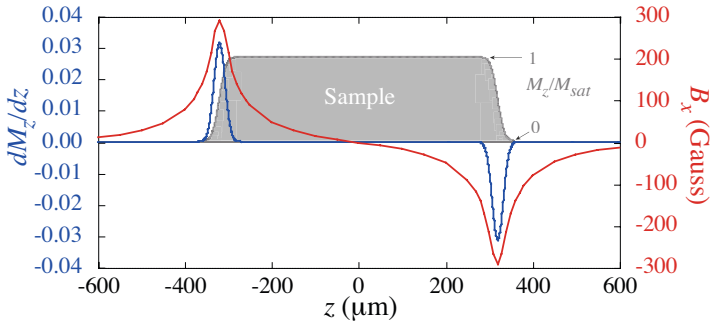

Figure 40: Using Eq. 12, values of B_x at different Hall sensor positions were calculated for the case of uniform magnetization at different Hall sensor positions (red trace). $d = 0.1\,\mu$m and the approximate dimensions of sample #1, $a = 290\,\mu$m and $c = 640\,\mu$m (i.e. the sample's ends were located at $z = \pm\ 320\,\mu$m) were used. $4\pi M_z$ for the full magnetization of Mn_{12}-acetate can be calculated as 1.29×10^3 Gauss (see Section 4.4.1). The end(s) of the sample on the z-axis was simulated using a Gaussian function for $\partial M_z/\partial z$ (blue trace), resulting in an error function for M_z (gray shade). A large value of $30\,\mu$m for the Gaussian function was chosen for the full width at half maximum (FWHM) for illustrative purposes.

Fig. 40 shows an example of the calculated B_x profile along the z-axis for the case of full magnetization for Mn_{12}-acetate. Using Eq. 12, values of B_x at different Hall sensor positions were calculated for the case of uniform magnetization at different Hall sensor positions (red trace). The approximate dimensions of sample #1, $a = 290\,\mu$m and $c = 640\,\mu$m (i.e. the sample's ends were located at $z = \pm\ 320\,\mu$m) were used. The thickness assumed for the insulation layer on the array of Hall sensors was $d = 0.1\,\mu$m. $4\pi M_z$ for the full magnetization of Mn_{12}-acetate can be calculated as $4\pi M_{sat} = 1.29 \times 10^3$ Gauss (see Section 4.4.1). The end of the sample on the z-axis was simulated using a Gaussian function for dM_z/dz (blue trace); this yields the error function for M_z(gray shade). A large value of $30\,\mu$m was chosen for the full

width at half maximum (FWHM) for the Gaussian function for illustrative purposes.[27] In Eq. 12, $\partial M_z(z')/\partial z$ (blue trace) is integrated with a function $F(z-z')$ over z'. Therefore, the width of $B_x(z)$ (red trace) is widened by $F(z-z')$ which mostly depends on the parameter, a (see also Fig. 42).

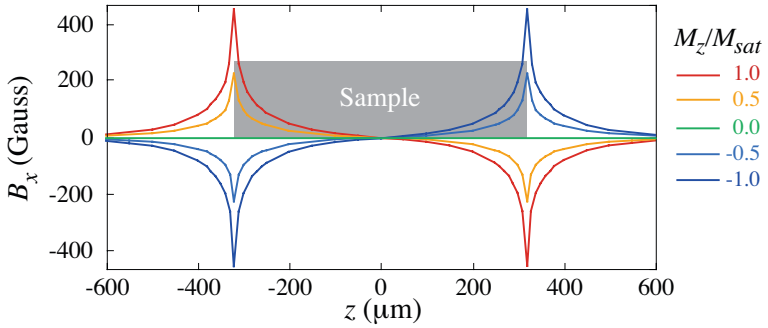

Figure 41: The same values for the parameters, a, c and d for Fig. 40 were used, but the FWHM of the Gaussian function for $\partial M_z/\partial z$ at the ends of the sample was changed to the more realistic value of 5 μm. The uniform magnetization value of M_z/M_{sat} was varied from 1.0 at positive saturation to -1.0 at negative saturation.

In Fig. 41, the same values for the parameters, a, c and d for Fig. 40 were used, but the FWHM of the Gaussian function for dM_z/dz at the ends of the sample was

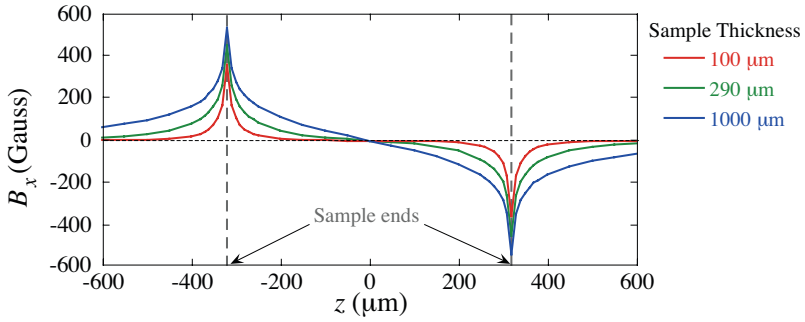

Figure 42: The value of a was varied to 100, 290 and 1000 μm, while the same values for the parameters, c and d for Fig. 40 were used; 5 μm was used for the FWHM of the Gaussian function for $\partial M_z/\partial z$ at the ends of the sample with the uniform magnetization value of $M_z/M_{sat}=1$.

[27]Since the magnetization is assumed to be uniform within the sample, dM_z/dz rather describes the molecular density in the space. In reality, the sample ends should be much sharper. In Fig. 40, a large width was used dM_z/dz only for demonstration purpose for Eq. 12 and Eq. 13.

changed to the more realistic value of 5 μm so that dM_z would have step function-like ends.[28] The uniform magnetization value of M_z/M_{sat} was varied from 1.0 (corresponding to positive saturation) to -1.0 (corresponding to negative saturation). As clearly seen in Eq. 11, at each position in z, the value of B_x is proportional to M_z/M_{sat}. This is true regardless of the sample shape [174].

B_x is shown in Fig. 42 for a =100, 290 and 1000 μm, while the same values for the parameters, c and d for Fig. 40 were used, and 5 μm was used for the FWHM of the Gaussian function for $\partial M_z/\partial z$ at the ends of the sample with the uniform magnetization value of $M_z/M_{sat} = 1$ in the sample. This dependence comes from the function, $F(z - z')$ in Eq. 13. As the sample thickness, a is reduced, $F(z - z')$ becomes a shorter range function in z.

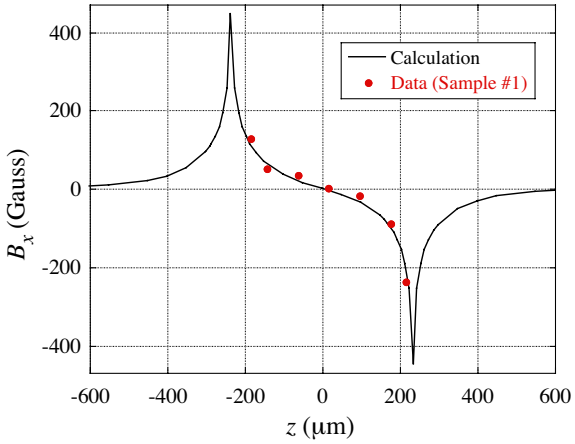

Figure 43: The measured values of B_x at positive saturation in Fig. 38 for sample #1 are shown (red dots). The black line is the best fit by calculation with Eq. 12 using the following parameters: a=470 μm, c=290 μm and d=0.1 μm. A Gaussian function with 5 μm for the FWHM was used for $\partial M_z/\partial z$ at the ends of the sample.

The measured values of B_x at positive saturation in Fig. 38 for sample #1 (the values of B_{sat} for each sensor position are the same as those used in Fig. 39) are plotted in Fig. 43 (red dots). The black line is the best fit by calculation with Eq. 12 using the following parameters: the width of sample #1 was estimated by a microscope

[28]It doesn't make sense to use smaller values since the spatial resolution of the Hall sensor (the dimension of the Hall sensor) is 10 μm.

to be $c = 290\,\mu$m. A thickness $d = 0.1\,\mu$m was used for the insulating layer of the array of Hall sensors, on which the sample was directly mounted. As seen in Fig. 34, sample #1 did not have square ends along the z-axis. Therefore, the calculation using Eq. 12 is not appropriate. In order to fit the data using step-function like square ends with an integral of a Gaussian function (5 μm for the FWHM), $a = 470\,\mu$m was used, which is 25 % smaller than the estimated mean length of sample #1 as determined by using a microscope and a calibrated slide.[29]

3.3.3 Fast Measurements

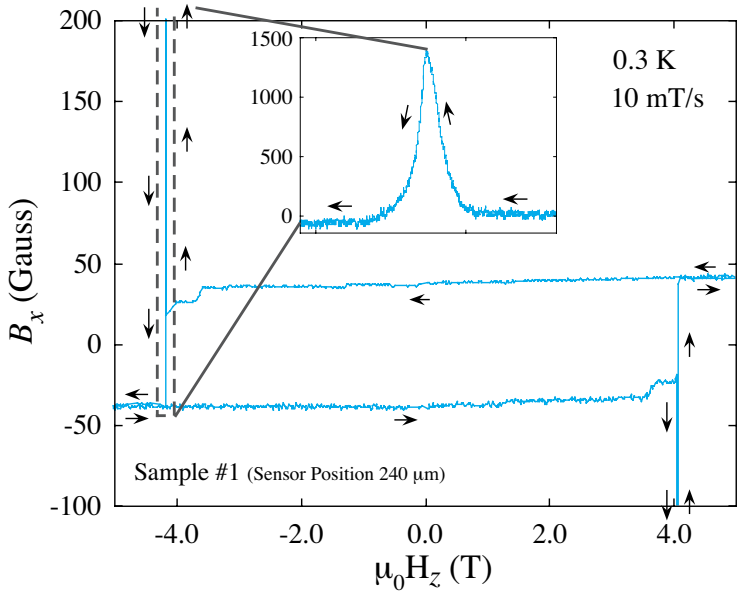

Figure 44: Hysteresis loops with avalanches in sample #1 are plotted. B_x was recorded by a Hall sensor situated about 80 μm above the middle of the sample (labeled as 240 μm in Fig. 37 (a) and Fig. 38). Steps due to quantum tunneling of the magnetization are observed, followed by a sharp spike in B_x associated with an avalanche at $\pm$ 4.1 T, shown in the inset for -4.1 T.

Fig. 44 shows avalanches for sample #1. The magnetic field was swept upward and downward at 10 mT/s at a temperature of 0.3 K. Steps due to quantum tunneling

[29]These calculations are not expected to be accurate; the main purpose of this analysis is to examine the overall behavior and dependence on various parameters. Real samples don't have square ends so that accurate calculation is impossible with this model which requires samples with perfect rectangular shape. A reliable numerical calculation is possible only by integrating over the actual sample shape.

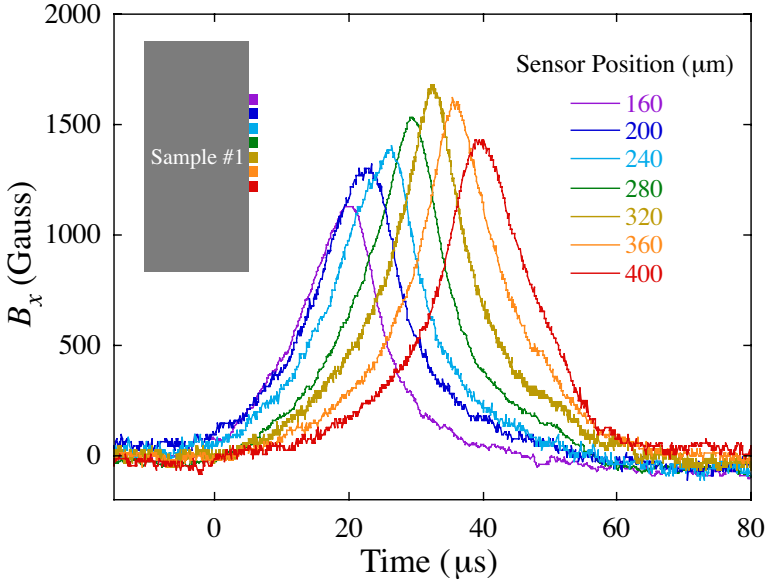

Figure 45: Signals recorded by seven equally spaced Hall sensors situated near the center of sample #1 during an avalanche triggered at $-4.1\,\mathrm{T}$. The left (right) trace corresponds to the top (bottom) sensor (see the inset). Sensor positions are measured relative to the top of the sample, with the center at $\approx 320\,\mu\mathrm{m}$.

of the magnetization were observed, with a magnetization that was almost uniform throughout the sample, until an avalanche occured at $\pm 4.1\,\mathrm{T}$, as shown in the inset (for -4.1 T only). throughout the sample, until an avalanche occured at $\pm 4.1\,\mathrm{T}$, as

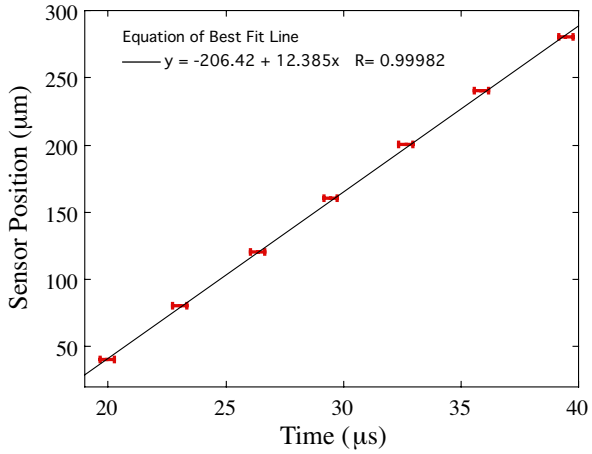

Figure 46: The sensor position versus the time at which the sensor recorded peak amplitude in Fig. 45 are plotted. A straight line fit yields a constant velocity of propagation of $12\,\mathrm{m/s}$.

shown in the inset (for -4.1 T only). During the avalanche the Hall sensor recorded a large peak in B_x, signaling the abrupt onset of a highly non-uniform magnetization.

For the avalanche at -4.1 T, Fig. 45 shows the response of seven Hall sensors (out of the eleven sensors) placed in sequential positions near the center of the sample. The avalanche was triggered above the top-most sensor and traveled downward (see the inset). B_x displays the largest peak at the center. Fig. 46 shows the sensor position as a function of the time at which the sensor registered the peak amplitude. The slope of the straight line drawn through these points yields a constant velocity of 12 m/s for this avalanche.

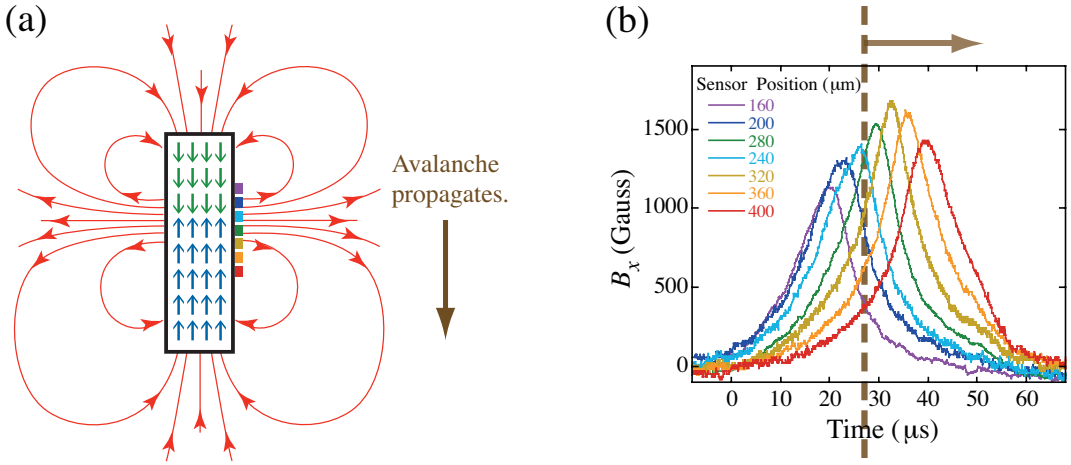

Figure 47: **(a)** A simple illustration of the propagation of an avalanche interface is shown. A magnetic quadrupole-like field is created giving a large B_x value at the interface. **(b)** The top sensor at 160 μm registered the peak in B_x first and the other sensors registered similar peaks sequentially from top to bottom. The avalanche is inferred to have originated somewhere above the top sensor with an interface that propagated downward. The dark dashed line indicates the approximate time when the interface of the avalanche just passed the Hall sensor at 240 μm.

A model of the propagating avalanche front can be inferred from the measured B_x with a simple diagram shown in Fig. 47 (a).[30] A magnetic quadrupole-like field is created giving a large B_x value at the interface between regions of opposing magnetization. Therefore the Hall sensor closest to the interface registers a peak at the

[30]The calculation using Eq. 12 is also shown later in Section 3.3.4.

time the interface is passing. As shown in Fig. 47 (b), the top sensor at 160 μm registered the peak in B_x first and the other sensors register similar peaks in sequential order from top to bottom. The avalanche was inferred to have originated somewhere above the top sensor with an interface front propagating downward. As can be seen in Fig. 46, the avalanche front propagated with a constant velocity of 12 m/s which is two orders of magnitude smaller than the typical speed of sound in solids.

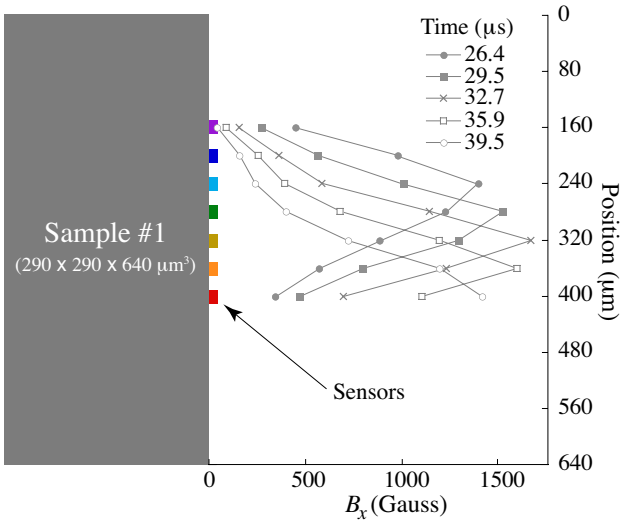

Figure 48: The data in Fig. 45 are re-plotted as a function of position for different times.

In Fig. 48, the data in Fig. 45 are re-plotted as a function of position at different times. As can be seen, spatial resolution is lower than time resolution having fewer data points on each curve. At times 16.4, 29.5, 32.7, 35.9 and 39.5 μs, used for the plot, one of the sensors registered a peak in B_x in Fig. 45. Therefore, the data point at the peak on each curve can safely be considered as the real peak position in Fig. 48. The width of the curves can not be inferred directly as the width of the avalanche interface, $\partial M_z/\partial z$. $B_x(z)$ gains additional thickness from the function $F(z-z')$ (see Eq. 13) which depends mainly on the thickness of the sample. Fig. 49 also shows the same data as a contour pot which maps B_x as a function of time and position.

Avalanches of three single crystals of Mn_{12}-acetate with dimensions: $0.29 \times 0.29 \times 0.64\,mm^3$ (sample #1), $0.28 \times 0.28 \times 1.44\,mm^3$ (sample #2), $0.24 \times 0.24 \times 1.02\,mm^3$ (sample #3) were measured. Most of the data were obtained at the base temperature of 0.3 K. The few points measured at 0.4 and 0.7 K were found to lie on the same curve within the scatter of the data, indicating that the temperature dependence is weak. A longitudinal magnetic field (parallel to the easy axis) was swept back and forth through the hysteresis loop to ± 6 T until an avalanche was triggered.[31] Avalanches were also found for sample #2 for zero field-cooled conditions, where the sample starts from zero magnetization (instead of full saturation). The velocity of propagation for each avalanche was obtained in the same way as in Fig. 46.[32] Fig. 50 shows velocity of propagation of avalanches versus longitudinal magnetic field at which the avalanches occurred for those three samples. Further analysis on these data is presented in the next section.

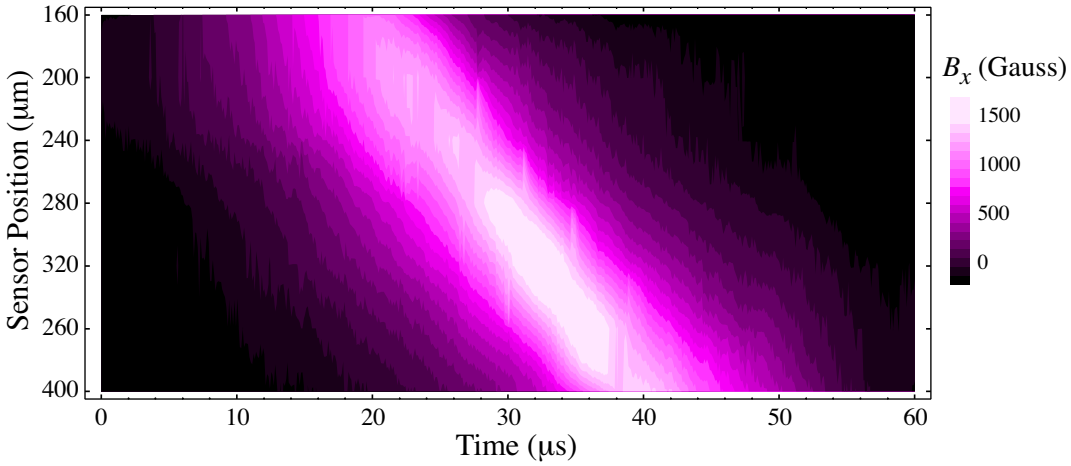

Figure 49: The data in Fig. 45 shown as a contour plot for B_x mapped as a function of time and sensor position.[33]

[31] As seen in Fig. 17, avalanches occur in a stochastic way at 0.3 K both at tunneling resonant magnetic fields (where energy levels on opposite side of the barrier match) and away from tunneling resonance.

[32] The sensors away from the ends of the sample were used for determinations of the propagation velocity in order to avoid edge effects.

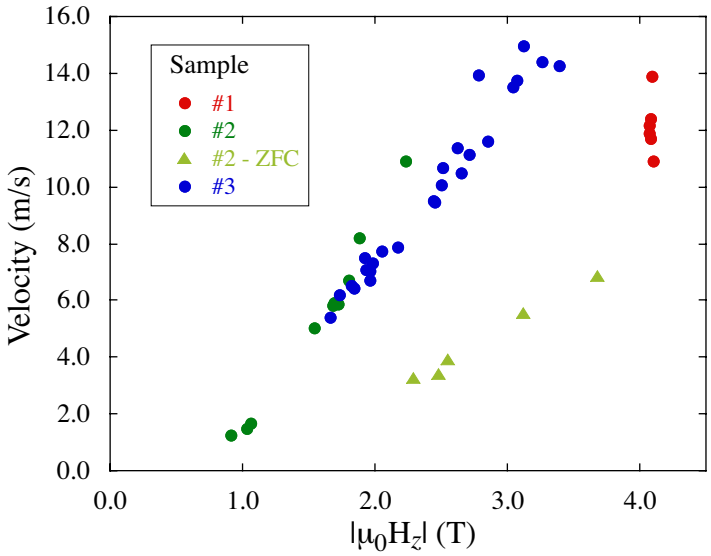

Figure 50: Velocity of propagation of avalanches versus longitudinal magnetic field at which the avalanches occured. ZFC denotes data obtained for sample #2 cooled in zero field, thus starting from zero magnetization and ending in full magnetization.

In Fig. 55, approximate values of σ_z (widths of $B_x(z)$ in z) for each avalanche are plotted as a function of the magnetic fields at which the avalanches occurred for the three samples. Since the resolution in space was small with a limited number of sensors as seen in Fig. 48, the values were obtained in the following way. Curves of B_x vs time for the sensor located at the center of each sample were used to estimate σ_t (the widths of B_x in time) at the half maximun of the peak (such as the curve at 320 μm in Fig. 45). To approximate σ_z, σ_t was multiplied by the propagation velocity v, which was obtained by the method in Fig. 46. $\sigma_z = \sigma_t \times v$ is valid when the avalanche interface becomes self-sustaining and the shape of the interface does not change in time while traveling along the z-axis. As mentioned before in Fig. 48, σ_z does not directly indicate the width of the avalanche interface of $\partial M_z/\partial z$, since $B_x(z)$ gains additional thickness from the function $F(z - z')$ (see Eq. 13) which depends mainly on the thickness of the sample.

[33]The low resolution of position (or the large difference in the resolution between position and time) has introduced additional noise in the contour lines.

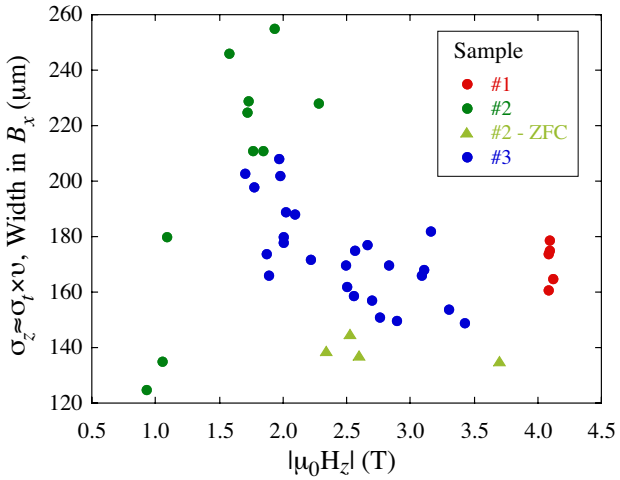

Figure 51: Approximate values of σ_z (widths of $B_x(z)$) for each avalanche plotted as a function of magnetic fields at which the avalanches occurred for the three samples. σ_z does not represent the width of the avalanche interface, $\partial M_z/\partial z$, as B_x gains additional thickness from the function $F(z-z')$ (see Eq. 13) which depends mainly on the thickness of the sample.

3.3.4 Analysis

Fig. 50 summarizes the data obtained for the velocity of propagation of avalanches recorded in different longitudinal magnetic fields for all three samples. For avalanches relaxing from full magnetization in one direction to the other ($\Delta M = 2M_{sat}$), the data for samples #2 and #3 lie on approximately the same curve. The velocity decreases with decreasing longitudinal magnetic field and goes to zero at about 0.6 T, below which no avalanches occur. Smaller velocities are obtained for avalanches in sample #2 when starting from the zero-field-cooled condition ($\Delta M = M_{sat}$). Avalanches for sample #1 were obtained only at relatively high magnetic fields in the vicinity of 4.1 T; the velocities for this sample range in value and do not appear to be consistent with data for the other two samples. In all cases the velocity increases with increasing magnetic field.

The change in magnetization, ΔM, during an avalanche is an important parameter. This parameter indicates how many molecules had their spins reversed during the avalanche, and $\Delta M/2M_{sat}$ represents the ratio of relaxed magnetization rela-

tive to maximum magnetization reversal (from full magnetization in one direction to the other). Before the avalanches, the magnetization is relatively uniform with quasi-equilibrium conditions, as explained in Section 3.3.2. After the avalanches, the magnetization normally reaches saturation in the opposite direction and is again uniform. In these cases, the Hall sensor signals can be interpreted as being proportional to the magnetization.

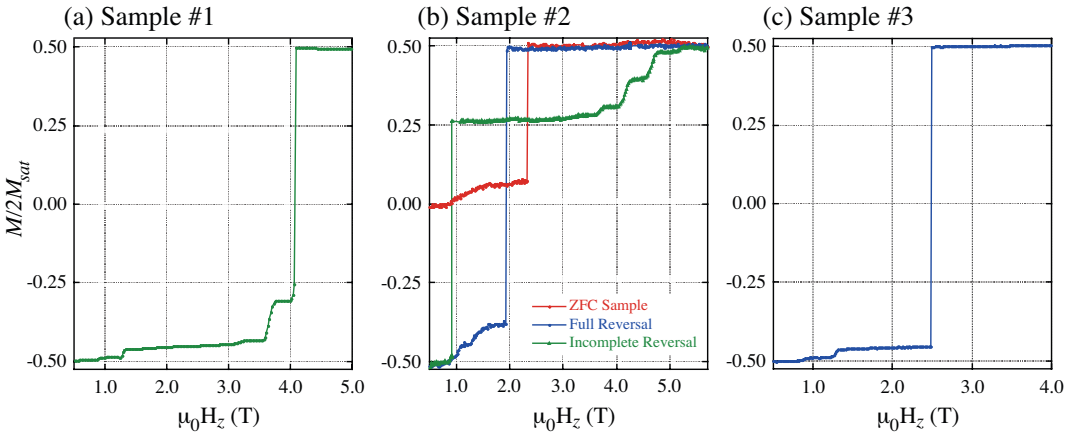

Figure 52: **(a)** A typical magnetization curve is shown for sample #1 for an avalanche at ±4.1 T. About 25 % of the magnetization relaxed by tunneling before the avalanche occurred. Therefore, the relaxed magnetization fraction during the avalanche is $\Delta M/2M_{sat} \approx 0.75$. **(b)** Magnetization curves are shown for three cases for sample #2; the field cooled sample had almost full reversal with $\Delta M/2M_{sat} \approx 1$ (blue curve), the ZFC sample had almost half of the full reversal with $\Delta M/2M_{sat} \approx 0.5$ (red curve), and the avalanche at lower magnetic field below 1.5 T had an incomplete reversal with $\Delta M/2M_{sat} \approx 0.75$ (green curve). In Fig. 52 (c), sample #3 had almost full reversal giving $\Delta M/2M_{sat} \approx 1$.

In Fig. 52 the normalized magnetization curves, $M/2M_{sat}$, are plotted for the three samples.[34] Slow sampling rates were chosen with a longer integration time to reduce the noise when there was no rapid change in the signal. The signal changed rapidly only during avalanches. For clarity, the data (the spikes as seen in Fig. 44) during the avalanches were omitted, and only the data before and after the avalanches

[34] About 5 % of the magnetization, which relaxed below 1.5 T for sample #1 and #3, was associated with the second species (see Section 2.2). Sample #2 contained a larger amount ($\sim$ 10 %) of the second species. In all cases, relaxation by the second species was disregarded. This might give an error of up to 5-10 %.

were potted. Therefore occurrences of avalanches appear as straight vertical lines (rather than spikes) in Fig. 52.

Fig. 52 (a) shows a typical magnetization curve for sample #1 for which avalanches occurred around $\pm 4.1\,\mathrm{T}$. The sample was magnetized first, and the magnetic field was reversed. Before the avalanche, about 25 % of the magnetization relaxed at the large tunneling resonances $N = 7, 8$ (see Section 2.2). This relaxation rate was much smaller as seen in the relatively flat part of the curves near $t = 0$ in Fig. 45 (i.e. just before the faster changes recorded during the avalanche). The relaxed magnetization during the avalanche is $\Delta M/2M_{sat} \approx 0.75$. Fig. 52 (b) shows magnetization curves for three cases for sample #2; the field cooled sample had almost full reversal with $\Delta M/2M_{sat} \approx 1$ (blue curve), the ZFC sample had almost half of the full reversal with $\Delta M/2M_{sat} \approx 0.5$ (red curve), and the avalanche at lower magnetic field below 1.5 T had an incomplete reversal with $\Delta M/2M_{sat} \approx 0.75$ (green curve). In Fig. 52 (c), sample #3 had almost full reversal giving $\Delta M/2M_{sat} \approx 1$.

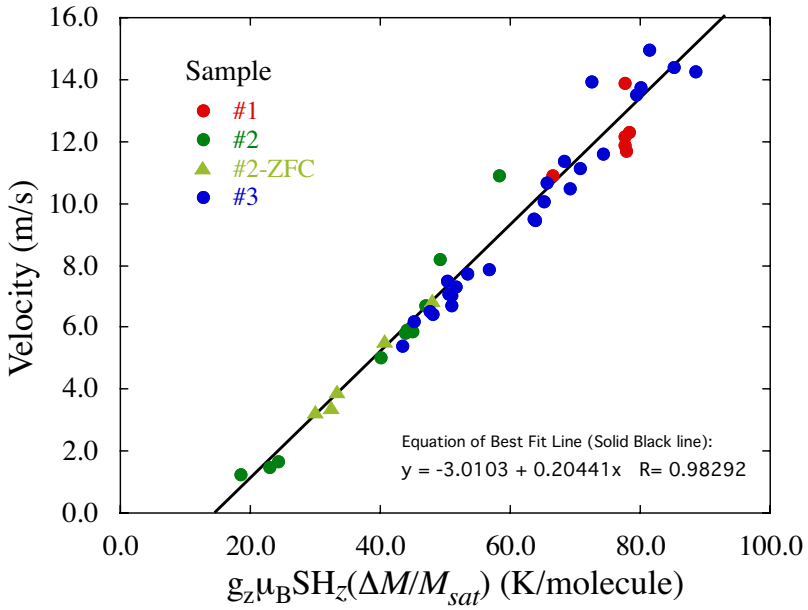

Figure 53: Velocity of propagation of avalanches versus released energy per molecule. Approximate collapse is obtained for all the data in Fig. 50 when plotted as a function of $g_z \mu_B HS(\Delta M/M_{sat})$. The best fit straight line is drawn to guide the eye.

$\Delta M/2M_{sat}$ indicates the fraction of molecules which reversed spin during the avalanche. Before the avalanche, each remaining molecule has stored potential Zeeman energy, $\Delta E(H_z) = 2g_z\mu_B S H_z$. The product yields

$$\Delta E_{Avalanche}(H_z) = g_z\mu_B S H_z \frac{\Delta M}{M_{sat}}\,, \tag{14}$$

the energy released per molecule during an avalanche (here $g_z = 1.94$ is the gyromagnetic factor in z, μ_B is the Bohr magneton, H_z is the longitudinal magnetic field at which an avalanche occurs, and $S = 10$ is the spin of the molecule).[35] Interestingly, as shown in Fig. 53, an approximate collapse is obtained for all the data in Fig. 50 when plotted as a function of the released energy per molecule, $\Delta E_{Avalanche}$. Thus, avalanches require the release of a threshold energy, above which they propagate with a speed that appears to be a linear function of the energy for the range investigated in these experiments.

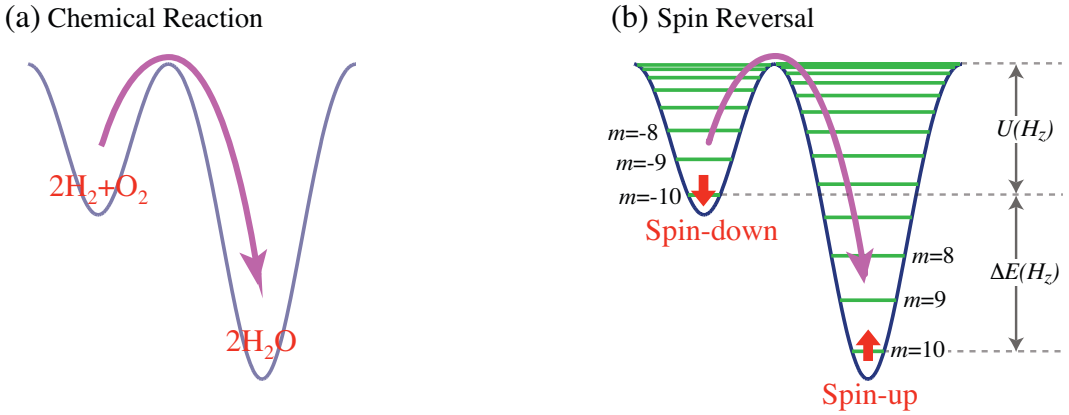

Figure 54: **(a)** A metastable state of a hydrogen and oxygen mixture can have a chemical reaction and produce the lower energy state of water with the difference in the chemical energy released. **(b)** The double well potential for the spin states of Mn_{12}-acetate with a longitudinal magnetic field, H_z. In this case, the spin flips from the metastable "spin-down" state to the stable "spin-up" state and the Zeeman energy, ΔE, is released.

Now, let us consider an appropriate model for this avalanche phenomenon in Mn_{12}-acetate. Our observations cannot be attributed to magnetization reversal asso-

[35] $\Delta E_{Avalanche}(H_z) = 2g_z\mu_B S H_z(\Delta M/2M_{sat}) = g_z\mu_B S H_z(\Delta M/M_{sat})$

ciated with domain wall motion, since there is no long-range order in our system.[36] E. M. Chudnovsley suggested that from a thermodynamic point of view, a crystal of Mn_{12} molecules placed in a magnetic field opposite to the magnetic moment is equivalent to a metastable (flammable) chemical substance [173]. In our case, the role of the chemical energy stored in a molecule is played by the difference in the Zeeman energy, $\Delta E(H_z) = 2g_z\mu_B S H_z$, for states of the Mn_{12}-acetate molecule that correspond to S parallel and antiparallel to H_z. For Mn_{12}-ac in a field of a few Tesla, $\Delta E(H_z)$ is below 0.01 eV, as is the energy barrier, $U(H_z)$, between spin-up and spin-down states due to the magnetic anisotropy. Thus, for the avalanches in Mn_{12}-acetate, both ΔE and U are two orders of magnitude smaller than typical energies of chemical reactions. However, our temperature range is also more than two orders of magnitude below room temperature, making the analogy rather close.

Fig. 54 shows a simple picture of the analogy. In Fig. 54 (a), a metastable state of a hydrogen and oxygen mixture can have a chemical reaction and produce the lower energy state of water with the difference in the chemical energy released. Fig. 54 (b) shows the double well potential for the spin states of Mn_{12}-acetate in a longitudinal magnetic field, H_z. In this case, the spin flips from the metastable "spin-down" state to the stable "spin-up" state, and the Zeeman energy, ΔE, is released. In both cases, the released energy induces the neighboring systems to go through the same process.

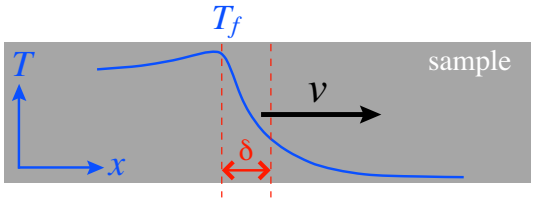

Figure 55: The propagation of the flame front with width, δ is illustrated. The simple theory of deflagration shows that the flame front approximately has the shape of $T = T_f \exp[-v(x - vt)/\kappa]$, which propagates with speed, v.

[36] Small dipolar long-range interactions between molecules might exists in Mn_{12}-acetate [175,176]. However, the strength is many orders of magnitude smaller than for the avalanches we observed.

A well-known mechanism for the release of energy by a metastable chemical substance is combustion or slow burning, technically referred to as deflagration [177]. It occurs as a flame of finite width, δ, propagates at a constant speed, v, small compared to the speed of sound. The parameter δ is determined by the distance, $\delta \sim \sqrt{\kappa\tau}$ through which the heat diffuses during the time of the chemical reaction τ. In our case

$$\tau(H_z) = \tau_0 \exp\left[\frac{U(H_z)}{k_B T_f}\right], \tag{15}$$

where $\tau_0 \sim 10^{-7}\,\mathrm{s}$ is the attempt time [34] and T_f is the temperature of the flame front. The dynamics of the flame are governed by the thermal diffusivity, κ, which obeys:

$$\frac{\partial T}{\partial t} = \kappa \nabla^2 T\,. \tag{16}$$

For κ independent of T, substituting $T = T(x - vt)$ a $x > vt$, one obtains $T = T_f \exp\left[-v(x - vt)/\kappa\right]$ in front of the interface, which yields $v\delta = \kappa$ (see Fig. 55). An interface thickness that is at most the distance between sensors, $\delta \sim 30\,\mu\mathrm{m}$, and the experimentally measured velocities of the order of $1 - 15\,\mathrm{m/s}$, yield an upper bound on κ in the range $10^{-5}\,\mathrm{m}^2/\mathrm{s}$ to $10^{-4}\,\mathrm{m}^2/\mathrm{s}$, consistent with heat pulse experiments.[37]

Combining $v\delta = \kappa$ with $\delta \sim \sqrt{\kappa\tau}$, one obtains:

$$v \sim \frac{\delta}{\tau} \sim \sqrt{\kappa/\tau} = \left(\frac{\kappa}{\tau_0}\right)^{1/2} \exp\left[-\frac{U(H_z)}{2k_B T_f}\right]. \tag{17}$$

The strongest dependence of v on H_z derives from the exponential, which contains the known dependence [165] of the energy barrier, $U(H_z)$, on the magnetic field.

It is of interest to estimate the temperature of the flame front, T_f, for these avalanches. We have estimated T_f by calculation using published results for the heat-capacity of Mn_{12}-acetate [152, 178–181].

$$C_{total} = C_{phonon} + C_{spin} + C_{hyperfine}\,. \tag{18}$$

[37] J. Tejada (private communication), A $10\,\mu\mathrm{s}$ heat pulse was found to travel a distance $d = 1\,\mathrm{mm}$ in a time $t \sim 20 - 50\,\mathrm{ms}$, yielding $\kappa \sim d^2/t \sim (2-5) \times 10^{-5}\,\mathrm{m}^2/s$.

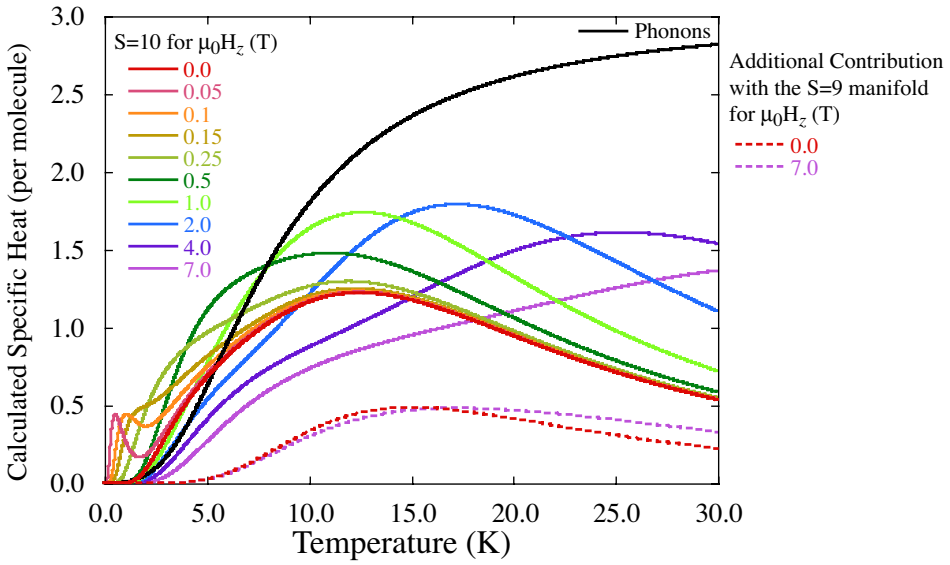

Figure 56: With the Debye temperature, $\Theta_D = 34\,\mathrm{K}$. the lattice heat capacity per molecule, $C_{phonon}(H_z)$ was calculated as the derivative of Eq. 19. The heat capacity per molecule due to spin, $C_{spin}(H_z)$, was calculated for different longitudinal magnetic fields from Eq. 21. For $C_{spin}(H_z)$ at small non-zero H_z, there is a peak below 3 K. This is because the ground state in the metastable well has slightly higher energy than the ground state in the stable well [178]. This behavior is quenched at very low temperatures, $>\sim 2\,\mathrm{K}$ due to the slow relaxation through the anisotropy energy barrier. At higher temperatures, $C_{spin}(H_z)$ has a Schottky behavior.

The hyperfine energy splittings are small, and their contribution is negligible above 0.3 K in our measurements. [182] The Debye temperature, $\Theta_D = 34\,\mathrm{K}$ [181] was used in the calculation for the Debye model.

$$\langle E_{phonon}(T)\rangle = 9T\left(\frac{T}{\Theta_D}\right)^3 \int_0^{\Theta_D/T} \frac{x^3}{e^x - 1} dx\,. \tag{19}$$

The temperature of the flame front is expected to reach close to the Debye temperature of 34 K. Therefore, it is important to use the full expression rather than the low temperature approximation. Taking the derivative of the internal energy, the lattice heat capacity per molecule, $C_{phonon}(T) = \frac{\partial\langle E_{phonon}(T)\rangle}{\partial T}$ (black solid curve) is shown as a function of temperature in Fig. 56.

[38]The values for T_f are different from the ones in Ref. [173], in which, T_f was calculated using the low temperature approximation for the Debye model instead of the full form of Eq. 19.

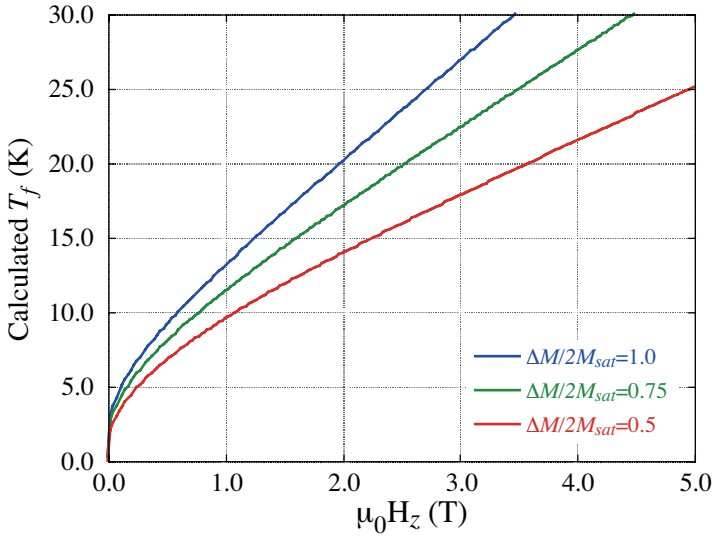

Figure 57: The spin and lattice temperature is calculated for a system starting at T=0.3 K assuming that 100% of the energy released per molecule during avalanche, $\Delta E_{Avalanche} = g_z \mu_B S H_z (\Delta M/M_{sat})$, is converted into thermal energy.[38] Eq. 22 was solved numerically for T_f with $\Delta M/2M_{sat} = 1.0$ (blue curve), 0.75 (green curve) and 0.5 (red curve) and is plotted as a function of H_z.

The Schottky magnetic energy contribution, $C_{spin}(H_z)$, was calculated for different magnetic fields, H_z, using the simplified spin Hamiltonian for $S = 10$,[39]

$$\mathcal{H} = -DS_z^2 - g_z \mu_B S_z H_z \,, \tag{20}$$

where $D = 0.65$ K and $g_z = 1.94$. The internal magnetic energy per molecule can be calculated as

$$\langle E_{spin}(H_z, T) \rangle = \frac{\sum\limits_m \Delta E_m(H_z) \exp(-E_m(H_z)/T)}{\sum\limits_m \exp(-E_m(H_z)/T)} \,, \tag{21}$$

where E_m are the 21-energy levels for $S = 10$ and ΔE_m are the energy spacings from the ground state. The spin heat capacity per molecule, $C_{spin}(H_z, T) = \frac{\partial \langle E_{spin}(H_z,T) \rangle}{\partial T}$, is plotted as a function of temperature in Fig. 56 for different longitudinal magnetic fields (solid colored curves) . At higher temperatures, the spin mixings (such as the $S = 9$ manifold) could play a role. The internal magnetic energy in the case of $S = 10$ with the $S = 9$ manifold was therefore also estimated. There has been no definitive

[39]The results using the Hamiltonian with the higher order, AS_z^4 yielded only small differences in the result.

determination of the energy levels of $S = 9$ for Mn_{12}-acetate.[40] We approximated this by using the measured parameters for the S=9 manifold for the similar system of Mn_{12}-BrAc; the energy levels of $S = 9$ lie at 40 K above $S = 10$ with the same spin Hamiltonian except with a somewhat smaller anisotropy of $D = 0.62\,\mathrm{K}$ [183]. The additional contribution to the spin heat capacity due to the S=9 manifold is plotted for $\mu_0 H_z = 0.0\,\mathrm{T}$ (dashed red curve) and $\mu_0 H_z = 7.0\,\mathrm{T}$ (dashed purple curve). This additional contribution did not make significant changes in the analysis of the propagation velocities so it was neglected in all the analysis.

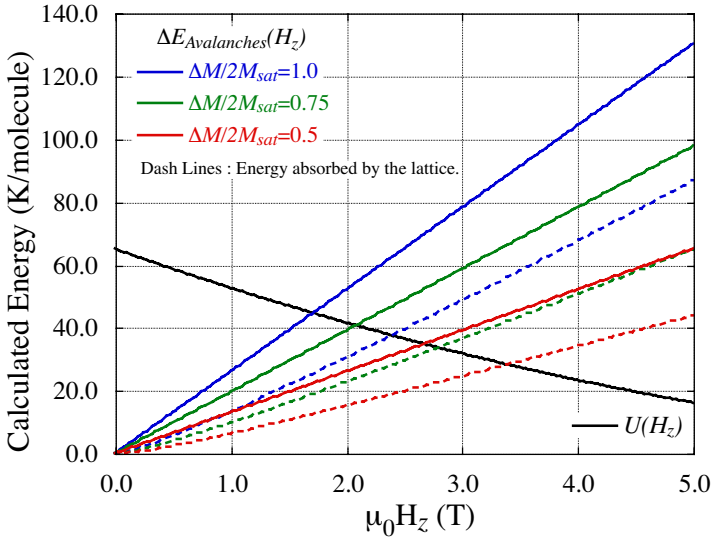

Figure 58: The classical energy barrier, $U(H_z)$ (see Fig. 54 and Eq. 23) was calculated and is plotted as a function of $\mu_0 H_z$ (solid black curve).[41] Also the energy released per molecule, $\Delta E_{Avalanche}(H_z) = \Delta E(H_z) \times \Delta M/2M_{sat}$ is shown for $\Delta M/2M_{sat} = 1.0$ (solid blue line), 0.75 (solid green line) and 0.5 (solid red line). $T_f(H_z)$, the flame front temperature (which would be raised by the released energy, $\Delta E_{Avalanche}(H_z)$) was solved for $\Delta M/2M_{sat} = 1.0$, 0.75 & 0.5 using Eq. 22 and is plotted in Fig. 57. The energy, $\langle E_{phonon}(T_f)\rangle$ in Eq. 22 was also solved and indicates the energy which is converted into phonons at the flame front and is plotted with dashed lines. The energy difference between the solid and dashed lines is $\langle E_{spin}(T_f)\rangle$ which should be absorbed by the spin at the flame front according to the calculation.

Before the occurrence of an avalanche, the temperature of the sample was stable at 0.3 K. At this temperature, all the molecules had spins in the lowest state of either

[40] Mn_{12}-acetate contains intrinsic molecular disorder [130] which makes the measurements for the energy levels of $S = 9$ more difficult.

[41] This energy barrier is lowered at tunneling resonances due to quantum tunneling.

the stable well or the metastable well, and the high anisotropy barrier prevented the spin from moving between them. $\langle E_{phonon}(T)\rangle$ is almost zero at $T = 0.3\,\mathrm{K}$. The Zeeman energy in the biased magnetic field is the only internal energy which is stored. Assuming that 100 % of the released energy per molecule during avalanche, $\Delta E_{Avalanche}(H_z) = g_z\mu_B S H_z(\Delta M/M_{sat})$, contributes to bringing the temperature of the spin and the lattice to $T_f(H_z)$ from 0.3 K,

$$g_z\mu_B S H_z(\Delta M/M_{sat}) = \langle E_{spin}(H_z, T_f(H_z))\rangle + \langle E_{phonon}(T_f(H_z))\rangle\,. \qquad (22)$$

This equation was numerically solved for $T_f(H_z)$ for different $\Delta M/2M_{sat}$. $T_f(H_z)$ is plotted as a function of $\mu_0 H_z$ in Fig. 57.

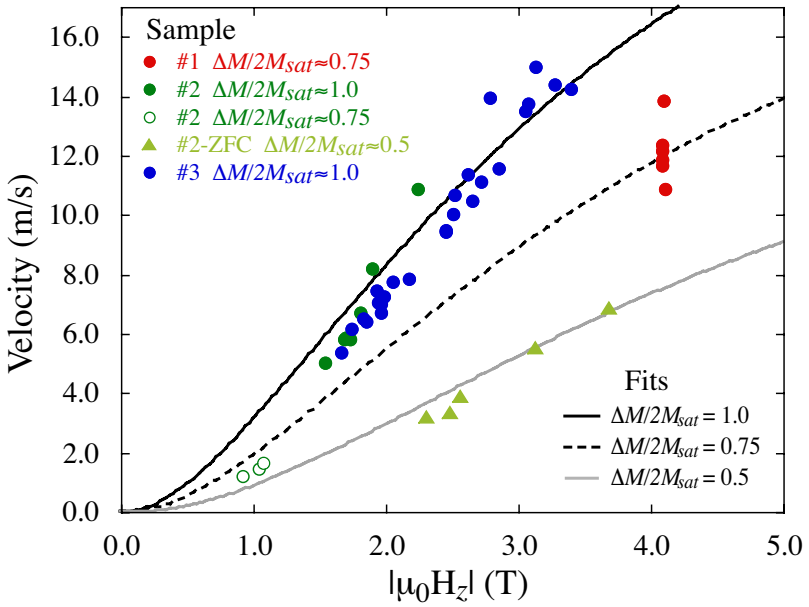

Figure 59: Velocity of propagation of avalanches versus longitudinal magnetic field at which the avalanches occurred (samples are identified by number).[42] ZFC denotes data obtained for the sample cooled in the absence of a magnetic field. From top to bottom, the curves are fits with Eq. 17 using $T_f(H_z)$ obtained from Eq. 22 for $\Delta M/2M_{sat} = 1.0$, 0.75, 0.5.

In Fig. 58, $\Delta E_{Avalanche}(H_z)$ for $\Delta M/2M_{sat} = 1.0$ (solid blue line), 0.75 (solid green line) and 0.5 (solid red line) is calculated and plotted as a function of $\mu_0 H_z$.

[42]The values of the velocity and T_f are different from those in Ref. [173], where T_f was calculated using the low temperature approximation for the Debye model instead of the full form of Eq. 19.

The calculated $\langle E_{phonon}(T_f)\rangle$ in Eq. 22 is also plotted with dashed lines. Using the Hamiltonian in Eq. 20, $U(H_z)$ (see Fig. 54), the classical energy barrier [165] can be calculated[43] as

$$U(H_z) = DS^2\left(1 - \frac{g_z\mu_B H_z}{2SD}\right)^2 . \tag{23}$$

In Fig. 58, $U(H_z)$ is plotted as a function of $\mu_0 H_z$ (solid black curve).

Also the energy released per molecule, $\Delta E_{Avalanche}(H_z) = \Delta E(H_z) \times \Delta M/2M_{sat}$ is shown for $\Delta M/2M_{sat} = 1.0$ (solid blue line), 0.75 (solid green line) and 0.5 (solid red line). $T_f(H_z)$, the flame front temperature (which would be raised by the released energy, $\Delta E_{Avalanche}(H_z)$) was solved for $\Delta M/2M_{sat} = 1.0$, 0.75 & 0.5 using Eq. 22 and is plotted in Fig. 57. The energy, $\langle E_{phonon}(T_f)\rangle$ in Eq. 22 was also solved and indicates the energy which is converted into phonons at the flame front and is plotted with dashed lines. The energy difference between the solid and dashed lines is $\langle E_{spin}(T_f)\rangle$ which should be absorbed by the spin at the flame front according to Eq. 22.

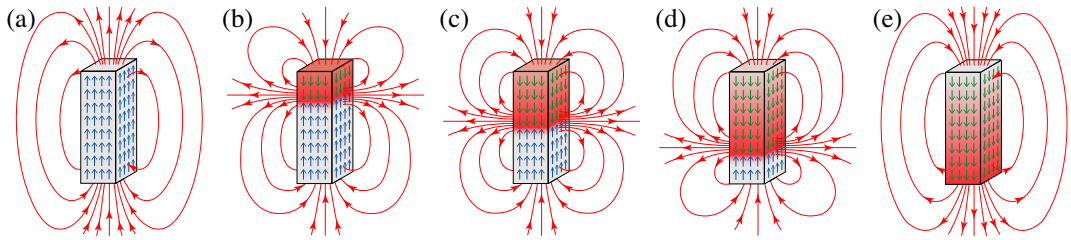

Figure 60: A simple demonstration of magnetic deflagration (slow burning) is shown. **(a)** The sample is magnetized upward, then the reversing magnetic field is applied. **(b)-(d)** The sample starts to flip its spin from the top as a "burning flame" front. The flame front propagates downward with constant speed. **(e)** As it finishes burning, the magnetization of the entire sample has reversed. This phenomenon is nondestructive as the spin simply flips up or down during the process.

We estimate that the released magnetic energy raises the temperature of the flame front to 13 K for an avalanche at 1 T and 27.5 K for an avalanche triggered at 4 T. Fits to Eq. 17 then yield the curves shown in Fig. 59, and reasonable values of κ and τ_0. For the best fit curves, 23.1, 17.7 and 12.4 were used for the prefactor of

[43] This energy barrier is lowered at tunneling resonances due to quantum tunneling.

Eq. 17, $\left(\frac{\kappa}{\tau_0}\right)^{1/2}$ for the avalanches with $\Delta M/2M_{sat} = 1.0$, 0.75 and 0.5 respectively.[44] Here we have used the simplest model of deflagration, a widely studied phenomenon that is known to be quite complex [184]. This crude model captures the overall behavior, and yields parameters that are quite reasonable in size. A more complete theory is needed to account for the apparent data collapse of Fig. 53.

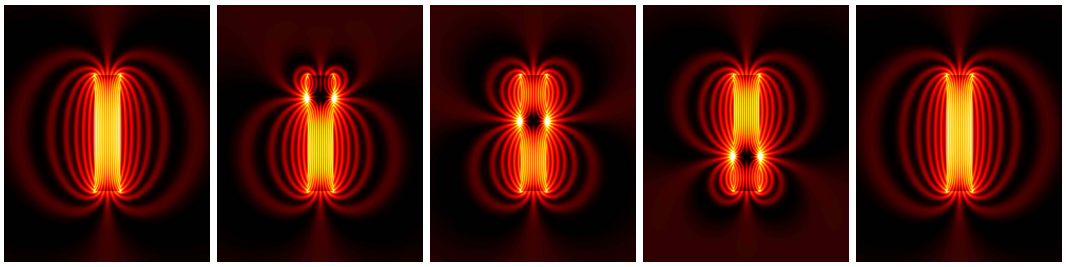

Figure 61: A simulation of an avalanche with calculated magnetic dipole field lines inside and outside of the sample is shown. In the same way as in Fig. 60, in the pictures from left to right, an avalanche starts at the top of the sample and propagate downward. The method for the calculation is shown in Section 4.4.2 in the appendix.

The strongest evidence that our observations are due to deflagration is the presence of a well defined propagating front requiring a threshold energy traveling at a subsonic velocity. It is also well known that deflagration of a flammable gas will not occur in a pipe of diameter, d small compared to the width of the flame front, δ. In our case, unless δ is small compared to the crystal diameter the heat generated will diffuse mostly through the sample walls and will not sustain the propagation of the interface. Indeed, avalanches tend occur in larger crystals with sufficiently large magnetization opposite to the direction of the field. The latter corresponds to the condition of "flammability" [184] needed to provide sufficient heating (that is, the large T_f) required for $\delta < d$. It is interesting to note that the few avalanches recorded around 1 T did not result in full reversal of the magnetization (see Fig. 52). At these

[44]The fitting procedure yielded a prefactor of two for different $\Delta M/2M_{sat}$, reflecting the fact that the prefactor is not well known within the theory. On the other hand, the exponential dependence is well captured by the model.

low fields the conditions for ignition are marginally satisfied, and the "flame" is extinguished before the process of magnetization reversal has been completed. This deflagration mechanism provides the condition needed for the avalanche to occur. In addition to available magnetic energy (flammability), the conditions for ignition may also depend on the shape and quality of the crystal, which may account for differences observed for different samples. The avalanches in the three samples, which we have measured, were triggered at the top edges of the samples and propagated downward.[45]

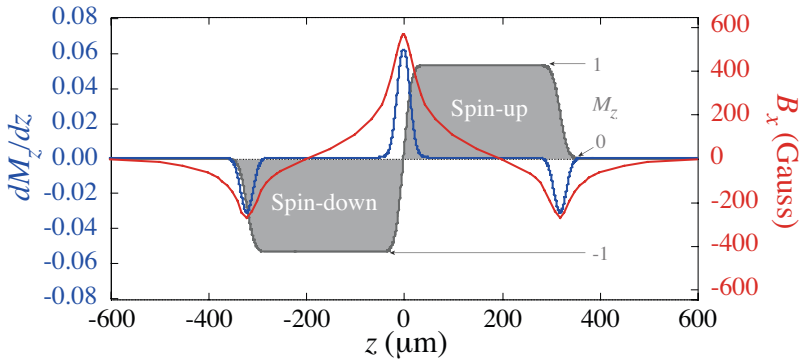

Figure 62: Using Eq. 12, values of B_x at different Hall sensor positions were calculated for the case of a sharp avalanche interface in the middle of the sample ($z = 1$) (red trace). The dimensions of sample #1, $a = 290\,\mu$m and $c = 640\,\mu$m (i.e. the sample's ends were located at $z = \pm\ 320\,\mu$m) and $d = 0.1\,\mu$m were used. $4\pi M_z$ for the full magnetization of Mn_{12}-acetate can be calculated as 1.29×10^3 Gauss (see Section 4.4.1). The ends and the interface of the sample in z-axis was simulated using a Gaussian function for $\partial M_z/\partial z$ (blue trace), resulting in an error function for M_z (gray shade). A large value of $30\,\mu$m for the Gaussian function was chosen for the full width at half maximum (FWHM) for illustrative purpose.

Slow burning at a subsonic speed (deflagration) is governed by the linear process of thermal conductivity. In addition to deflagration, unstable chemical substances also exhibit detonation, which can be caused by instability of the flame or by direct initiation other than through deflagration [184]. The initial stage of the detonation corresponds to a nonlinear supersonic shock wave [177,184]. Theory and experimental

[45]With sample #2 in a field cooled condition, an avalanche with neither distinct large peaks nor propagation of the peaks in the Hall sensor signals occurred occasionally. These data are not included in the analysis. These avalanches might have had the propagation direction perpendicular to the array of the Hall sensors. More investigation is needed.

studies of advanced stages of detonation are lacking. Based on the close analogy between unstable chemical substances and molecular magnets, the latter may well exhibit magnetic detonation under the right conditions.

In Fig. 60, a simple demonstration of magnetic deflagration (slow burning) is shown. In (a), the sample is magnetized upward, then the reversing magnetic field is applied. In (b)-(d), the sample starts to flip its spin from the top with a thin interface propagating downwards with constant speed, in analogy with a burning chemical "flame front". In (e), as it finishes burning, the magnetization of the entire sample has reversed. This phenomenon is nondestructive as the spin just flips up and down. "Ash" is the spin-down region while the remaining part is the spin-up region. Therefore, it can be reversible and can be repeated again and again. Also, the combustion energy can be tuned by the external magnetic field (see Fig. 54). In Fig. 61, a simulation of an avalanche with calculated magnetic dipole field lines inside and outside of the sample is shown. In the same way as in Fig. 60 in the pictures from left to right, an avalanche starts at the top of the sample and propagate downward.

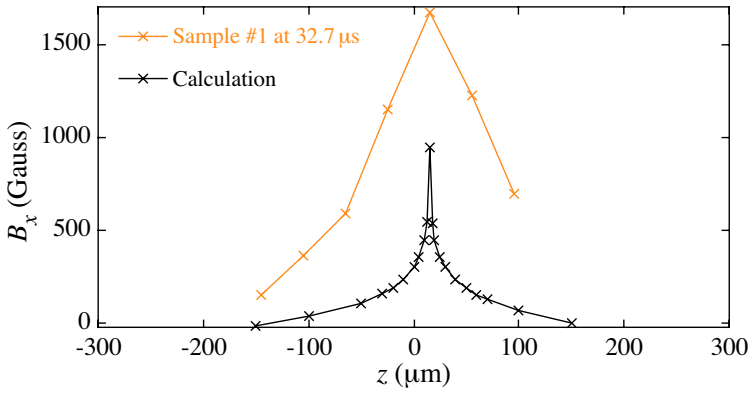

Figure 63: The measured values of B_x with the Hall sensors at seven different positions (at 32.7 μs in Fig. 48) for sample #1 are plotted (orange crosses). The black crosses are the calculation with Eq. 12 using the following parameters: a=470 μm, c=290 μm and d=0.1 μm. A Gaussian function with 5 μm for the FWHM was used as $\partial M_z/\partial z$ at the ends and the interface of the sample. For this avalanche (orange crosses), $M/2M_{sat}$ changed from -0.25 to 0.5 and $\Delta M/2M_{sat} = 0.75$ (see Fig. 52 (a)).

Using Eq. 12, values of B_x at different Hall sensor positions were calculated for

the case of an avalanche interface in the middle of the sample ($z = 1$) and are plotted in Fig. 62 (red trace). The dimensions of sample #1, $a = 290\,\mu$m and $c = 640\,\mu$m (i.e. the sample's ends were located at $z = \pm\ 320\,\mu$m) were used and $d = 0.1\,\mu$m was used. The ends and the interface of the sample in z-axis were simulated using a Gaussian functions for $\partial M_z/\partial z$ (blue trace), with a resulting error function for M_z (gray shade). A large value of $30\,\mu$m for the Gaussian function was chosen for the full width at half maximum (FWHM) for illustrative purpose.

In Fig. 63, the measured values of B_x with the Hall sensors at seven different positions (at $32.7\,\mu$s in Fig. 48) for sample #1 are plotted (orange crosses). The black crosses are the calculation with Eq. 12 using the following parameters: a=$470\,\mu$m, c=$290\,\mu$m and d=$0.1\,\mu$m. A Gaussian function with $5\,\mu$m for the FWHM was used as $\partial M_z/\partial z$ at the ends and the interface of the sample. There is a discrepancy in the amplitude of the peak. The measured amplitude is too large compare to the calculated value even with a very thin interface width. This might have been due to a miscalibration of the Hall sensors. Most likely, some kind of voltage induction across the signal wires due to the fast changing magnetic field from the sample could have mixed in with the Hall-voltage signals.[46] This effect can be separated from the Hall voltage by applying a different excitation current to the Hall sensors.

3.3.5 Discussion

Hernández-Mínguez, *et al.* have reported controlled ignition of avalanches by surface acoustic waves (SAWs) in a single crystal of Mn_{12}-acetate [156, 185, 186]. At temperature around 2 K, SAWs with frequencies 100 MHz to 1 GHz were used to heat the sample to trigger an avalanche in magnetic fields between 0.2 and 1.5 T. Ignition times were found to be 1 to 8 ms depending on magnetic field and the SAW power. The local magnetization was not measured. The total magnetization relaxed almost

[46]The fastest change in the magnetic field from the sample was near the avalanche interface. Therefore, in either case, there would have been no changes in the peak positions.

linearly with time after ignition and the linear relaxation continued for a time on the order of 1 ms. This relaxation was reproducible at fixed magnetic field, temperature and SAW output. Under the assumption that the avalanche originated at the end of the long axis and propagated at a constant speed to the other end [173], the velocity of propagation obtained as a function of magnetic fields was found to display maxima at the magnetic fields corresponding to the tunneling resonances. These authors attributed this to deflagration assisted by quantum tunneling: *quantum magnetic deflagration*.

According to the theory of deflagration, the velocity of propagation depends on the energy barrier, $U(H_z)$ as given in Eq. 17. As $U(H_z)$ is reduced, the velocity of propagation should be larger. Mn_{12}-acetate is known to exhibit quantum tunneling, effectively lowering the barrier $U(H_z)$ at the resonances. In our results shown in Fig. 59, we did not observe any significant peaks in the velocity of propagation. We find a velocity that increases approximately linearly with increasing magnetic field. Hernández-Mínguez, *et al.* found a similar linear increase of velocity with magnetic field except for the maxima at the tunneling resonances.[47] We may not have observed the maxima due to an insufficient number of data points and the noise associated with the stochastic triggering of avalanches in a swept magnetic field. We had only a few data points around 1 T in the range of magnetic field below 1.5 T where Hernández-Mínguez, *et al.* observed the maxima. We were not able to ignite the avalanche externally and avalanches did not occur spontaneously at low magnetic field, while Hernández-Mínguez, *et al.* were able to probe the velocity at lower magnetic fields since they triggered avalanche with SAWs. There were also other differences in experimental conditions: they performed the measurements at ~ 2 K in a ^{4}He exchange gas while we performed the measurements at 0.3 K in ^{3}He liquid. This difference in temperature makes little difference within the simple model of deflagration of Eq. 17

[47] Their values of velocity were smaller than those obtained in our measurements.

which we are applying, but may be important in a more exact theory. Further work is needed to clarify these issues.

It is difficult in any event to predict at which magnetic field we should expect the velocity to be maximum. As the flame front travels through the sample, each molecule experience a large change in temperature in a short time. It also experiences a large change in internal magnetic field. If the internal longitudinal magnetic field at saturation is $\sim 500\,\mathrm{Gauss}$, the internal field changes by approximately $1000\,\mathrm{Gauss}$ in $30\,\mu\mathrm{s}$, corresponding to a magnetic field sweep rate of $3000\,\mathrm{T/s}$. These rapid changes may have a strong influence on the dynamics of the avalanches [162].

Furthermore, as seen in Fig. 53, the velocities obtained for different $\Delta M/2M_{sat}$ seem to collapse when all the data from Fig. 50 are plotted as a function of $g_z\mu_B S H_z(\Delta M/M_{sat})$, the total energy released per molecule. In Eq. 17, v depends on two parameters, $U(H_z)$ and T_f, and other parameters are assumed to be constant. We can assume that T_f depends only on the total energy released per molecule. Therefore the scaling in Fig. 50 suggests that v does not depend on $U(H_z)$ at all for the large range of $H_z\Delta M/2M_{sat}$ used in the scaling varying from $0.5H_z$ to $1.0H_z$. $U(H_z)$ depends strongly on H_z which tunes the classical energy barrier (see Fig. 58) (neglecting the reduction of barrier due to tunneling resonances; with the tunneling effect, $U(H_z)$ should have minima at certain values of H_z). However, at different magnetic fields, v only depends on the total released energy per molecule. Consequently, the fit to the simple deflagration theory in Fig. 59 requires three different pre-factors for three different $\Delta M/2M_{sat}$.

There are many possible origins for this discrepancy. The model is overly simplified and makes many assumptions. For example, thehermal diffusivity, κ was assumed to be independent of temperature, while κ could be strongly temperature dependent in this temperature range. Also, we did not consider the sample shape and surroundings which have a strong effect on the temperature profile and how rapidly the

energy will diffulse away. A simple one-dimensional approximation was used, since the samples were long and thin.

One of the easiest ways to determine whether the velocity of propagation is enhanced at the tunneling resonances is by applying a large transverse magnetic field to the sample during an avalanche. This can be easily achieved by applying a magnetic field at a some known angle relative to the easy axis as in Section 3.2.3. By increasing the tunneling rate, a large the transverse magnetic field might increase the velocity of propagation. To study the importance of thermal diffusion with different boundary conditions, one can vary the cooling environment and the surrounding materials. For example, Webster, *et al.* studied the duration of avalanches for samples with thermal coupling to the environment that was weak (sample placed in a glass tube) or strong (in helium exchange gas) [187].

Developing an external triggering method would make measurements of the velocity of avalanche propagation much easier and more reproducible. It would be good to have a very local trigger so that the processes of triggering and propagation are distinguishable. Also, global heating should be avoided so that most of the heat comes from the sample itself. On the other hand, it would also be interesting to study how external heat applied globally triggers avalanches. For example, a slow (or faster) increase in temperature at a fix magnetic field could trigger avalanches. One expects that rapid increases in temperature will be more likely to trigger avalanches.

There is also the possibility of "detonation" or the occurrence of a "deflagration to detonation transition" in Mn_{12}-acetate under certain conditions. Detonation is explosive burning, while deflagration is non-explosive burning (slow burning). In detonation, the pressure wave (shock wave) propagates with supersonic speed, while in deflagration the flame front (temperature wave) propagates with subsonic speed. In chemical detonation, chemical decomposition occurs: decomposition produces higher pressure, and higher pressure creates additional decomposition. Chemical detonation

is a very violent event with high pressure and temperature. This causes chemical decomposition which also requires strong interaction. With magnetic avalanches, such a violent event is not expected to occur. However, a small lattice distortion is enough to deform the magnetic structure and symmetry of Mn_{12}-acetate.

In the case of magnetic detonation in Mn_{12}-acetate the magnetization interface of spin-up and spin-down would travel with a supersonic speed. Such waves, which are not limited by the speed of phonons, may be possible. As mentioned earlier in this section, during magnetic deflagration in which the spin-up&down front propagates at 10 m/s, the sample undergoes fast internal magnetic field changes of 3000 T/s. This fast magnetic field sweep is probably enough to produce additional relaxation by tunneling due to symmetry breaking, or by reducing the anisotropy barrier due to tension or torque to the lattice [162]. If the spin-up&down front were to propagate at 10000 m/s, as is typical for detonation, there would be fast internal magnetic field changes of 3 MT/s, which would deform the molecule's magnetic structure enough to erase their magnetization history.[48] This magnetostriction wave could propagate as a shock wave.

[48]The rate of change of the internal magnetic field also depends on the width of the the spin-up&down interface. The thinner the interface, the faster the change in the internal magnetization. Here, 300 μm was used for the calculation.

3.4 Thermometer Response during Avalanches

A ruthenium oxide thermometer (see Section 4.3.2) mounted directly on sample A as in Fig. 64, was used to monitor the temperature during magnetic field sweeps. In Fig. 65, the magnetization and the thermometer reading were measured simultaneously with a slow sampling rate of $\sim 1\,\mathrm{Hz}$. The magnetic field was swept upward and downward with a sweep rate of $10\,\mathrm{mT/s}$. The sample was completely immersed in a liquid ^{3}He bath and the sample was stabilized at the base temperature of $0.3\,\mathrm{K}$. The thermometer signal had slight magnetic field dependence in its response. The thermometer was calibrated only in the absence of magnetic field, and the small increase in resistance in a magnetic field (the temperature decrease by $\sim 20\,\mathrm{mK}$ at $\pm 5\,\mathrm{T}$) did not correspond to a real change in temperature. During the field sweeps in Fig. 65, the temperature of the surrounding was kept around $0.3\,\mathrm{K}$ (except at the tunneling resonances and during an avalanche where heat was released from the sample). Please also note that the strange structures and the peaks around zero field were due to superconductivity of some materials which were used in the system and not from the sample.[49]

For the magnetic field sweep-down in Fig. 65, temperature increases of up to $200\,\mathrm{mK}$ (magenta curve) were recorded during the resonances for controlled quantum tunneling of magnetization in the absence of an avalanche (light blue curve).[50] For the magnetic field sweep-up, an avalanche occurred at $3.3\,\mathrm{T}$ (dark blue curve). Since all the energy was released in a short time, the temperature increased rapidly and cooled back down to the base temperature quickly within a few hundred milliseconds. Due to the slow sampling rate of the measurement, the temperature failed to record a high value at $3.3\,\mathrm{T}$ (red curve) when the avalanche occurred.

In Fig. 66, a ruthenium oxide thermometer was directly mounted on sample #1

[49] These peaks around the zero magnetic field were observed even with an absence of samples.

[50] When the bath temperature was $0.6\,\mathrm{K}$, and $0.84\,\mathrm{K}$, the thermometer reading increased to $0.65\,\mathrm{K}$ and $0.86\,\mathrm{K}$ respectively during the tunneling resonances.

in the same manner as shown in Fig. 64 and was used to monitor the temperature during magnetic field sweeps. Sample #1 was a smaller crystal compared to Sample A. This time, the temperature was recorded with a sampling rate of 10 MHz during an avalanche. The local Hall sensor signals in Fig. 45 were also measured simultaneously with a sampling rate of 10 MHz (rainbow colored curves). The temperature (dark red curve) increased during an avalanche and had the peak value in about 100 μs which was the duration of the avalanche propagation.

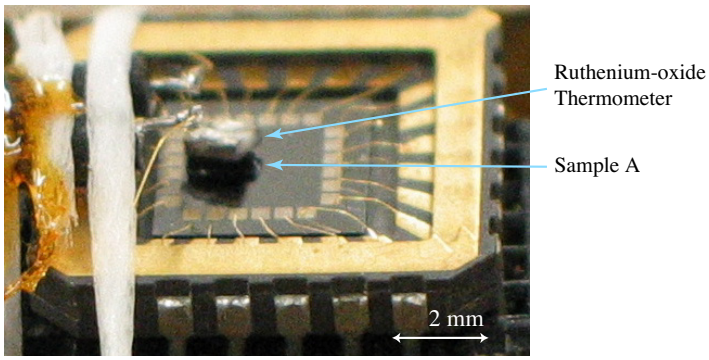

Figure 64: A ruthenium oxide thermometer (see Section 4.3.2) was mounted directly on a relatively large crystal, sample A.

In Fig. 67 (a), the same signals as in Fig. 66 were recorded at a slower sampling rate of 10 KHz for a longer recording period and a higher signal to noise ratio [188]. The monitored temperature was potted for a longer period of $\sim$ 100 ms. After the fast increase from 0.4 K to 1.8 K in 100 μs in Fig. 66, it cooled down partially on a slower time scale and was followed by another much wider peak which decayed with an even slower time scale of $\sim$60 ms. In (b), an avalanche occurred for very similar conditions with the same sample #1 except that the bath temperature was 0.7 K while the bath temperature in (a) was set at 0.3 K. The first peak was very similar to (a), but the second peak went up to a higher temperature and decayed more slowly compared to (a).

We can attribute the first peak to electromagnetic radiation emitted from the

sample during the avalanche. The ruthenium oxide thermometer can also act like a bolometer to some degree and absorb electromagnetic radiation which would increase the temperature of the thermometer. We attribute the second peak to heating by diffusion of phonons. The latter needed some time to reach the thermometer due to poor thermal connection between the sample and thermometer. For Fig. 67 (b), the sample was at 0.7 K and cooled by ^{3}He vapor. Therefore, it had a slower cooling rate compared to (a) where the sample was directly immersed in ^{3}He liquid at 0.3 K.

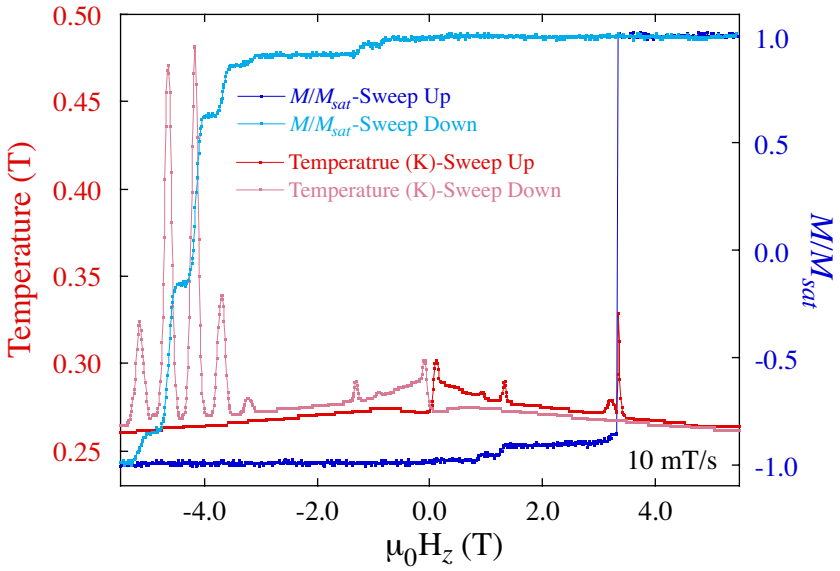

Figure 65: The magnetic field was swept upward and downward with a sweep rate of 10 mT/s. For the magnetic field sweep-down, temperature increases of up to 200 mK (magenta curve) were recorded during the resonances for controlled quantum tunneling of magnetization in the absence of an avalanche (light blue curve). For the magnetic field sweep-up, an avalanche occurred at 3.3 T (dark blue curve). Since all the energy was released in a short time, the temperature increased rapidly and cooled back down to the base temperature quickly within a few hundred milliseconds. Due to the slow sampling rate of the measurement, the thermometer failed to record a high temperature at 3.3 T (red curve) when the avalanche occurred.

For either (a) or (b), the measured temperature did not increase as high as predicted by the calculation for the temperature of the flame front in Fig. 57. The flame front temperature was expected to be 27.5 K for an avalanche at 4 T. The first sharp spike is probably associated with thermal radiation emitted by the propagating hot

flame front. The radiated temperature can not be determined from these data since we don't have spectral information and we don't know the precise optical properties of this material. For the second peak, the temperature did not reach as high because the thermometer and its setting have a larger thermal mass than the sample. This, as well as bad thermal contact between the sample and thermometer, probably result in most of the thermal energy diffusing elsewhere, leading to an erroneous thermometer reading.

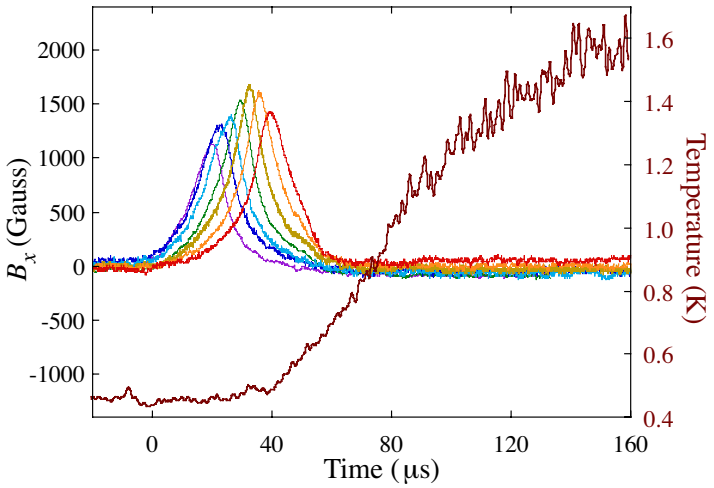

Figure 66: A ruthenium oxide thermometer was directly mounted also on sample #1 in the same manner as in Fig. 64 and was used to monitor the temperature during magnetic field sweeps. Sample #1 was a smaller crystal compare to sample A. This time, the temperature was recorded with a sampling rate of 10 MHz during an avalanche. The local Hall sensor signals in Fig. 45 were also measured simultaneously with a sampling rate of 10 MHz (rainbow colored curves). The thermometer data were digitally filtered by Fourier transformation with a low cut frequency of 1 MHz in order to improve the signal to noise ratio at higher temperatures, at which the detector had a small resolution. Please note that the ruthenium oxide thermometer has slower reaction time than the Hall sensors. The temperature (dark red curve) increased during avalanche and had the peak value in about 100 μs which was the duration of the avalanche.

Recent bolometer measurements of the radiation generated by a magnetic avalanche [154, 156, 164] (see also Fig. 13) gave puzzling results that can be understood within our model. One enigma was that the sample temperature measured by a thermometer directly following an avalanche was lower (< 6 K) than the temperature registered by the bolometer if one assumed thermal radiation. A second puzzle was that the

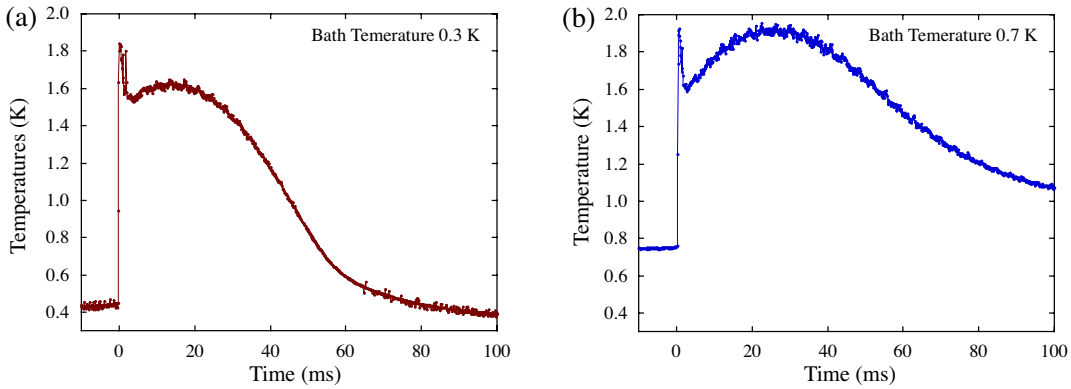

Figure 67: **(a)** The same signals in Fig. 66 was also recorded with a slower sampling rate of 10 KHz for a longer recording period and a higher signal to noise ratio. The monitored temperature was potted for a longer period of ~ 100 ms. After the fast increase from 0.4 K to 1.8 K in 100 μs in Fig. 66, it cooled down on a slower time scale and was followed by another much wider peak which decayed with an even slower time scale of $\sim$60 ms. **(b)** An avalanche occurred in very similar conditions with the same sample #1 except at a bath temperature of 0.7 K where the sample was cooled by ^{3}He vapor while the bath temperature in (a) was set at 0.3 K in ^{3}He liquid.

reversal of the magnetization during the avalanche occured on a much shorter time scale than the cooling of the sample following the avalanche [156]. We suggest that the radiation observed during avalanches is generated by the narrow hot interface (flame) that propagates through the crystal. The temperature of the bulk of the crystal (including the ash left behind the interface) is always significantly lower than the temperature of the interface itself. The time of the magnetization reversal is determined by the time $t = l/v$ needed for the interface to sweep the sample of length l. In our case $t \sim 100\,\mu$s, while the time needed for the ash to reach equilibrium with the thermal bath can be much longer.

4 General Experimental Techniques

In this chapter, some of the experimental techniques which were used for the measurements in Section 3 and some measurements in Section 2.2 are described. This chapter also supplements the earlier chapters where detailed descriptions of experimental techniques were skipped in order to maintain the flow of the text. Schematic diagrams and photographs are used as much as possible to supplement the text, since a picture is worth a thousand words.

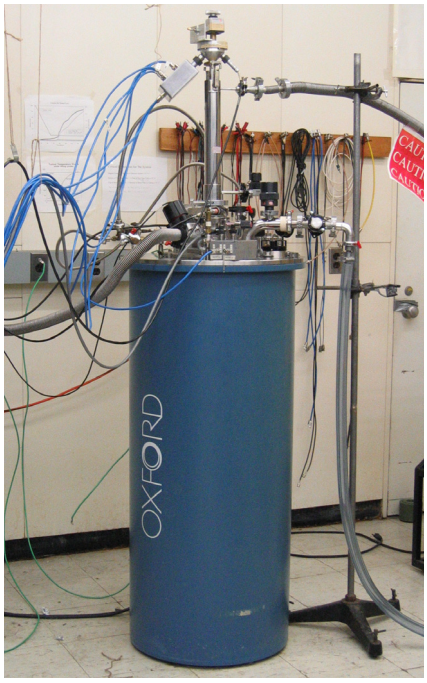

Figure 68: A commercial Oxford top-load ^{3}He cryostat was used to do most of the measurements. This side view photograph of the ^{3}He cryostat shows the system with the probe in the *"down"* position (see also Fig. 70).

4.1 ^{3}He Cryostat

A commercially made Oxford top-loading ^{3}He Cryostat (Helox^{TL} system) was used for most of the measurements to achieve the low temperature required. This system can reach temperatures as low as 250 mK with relatively high cooling power and

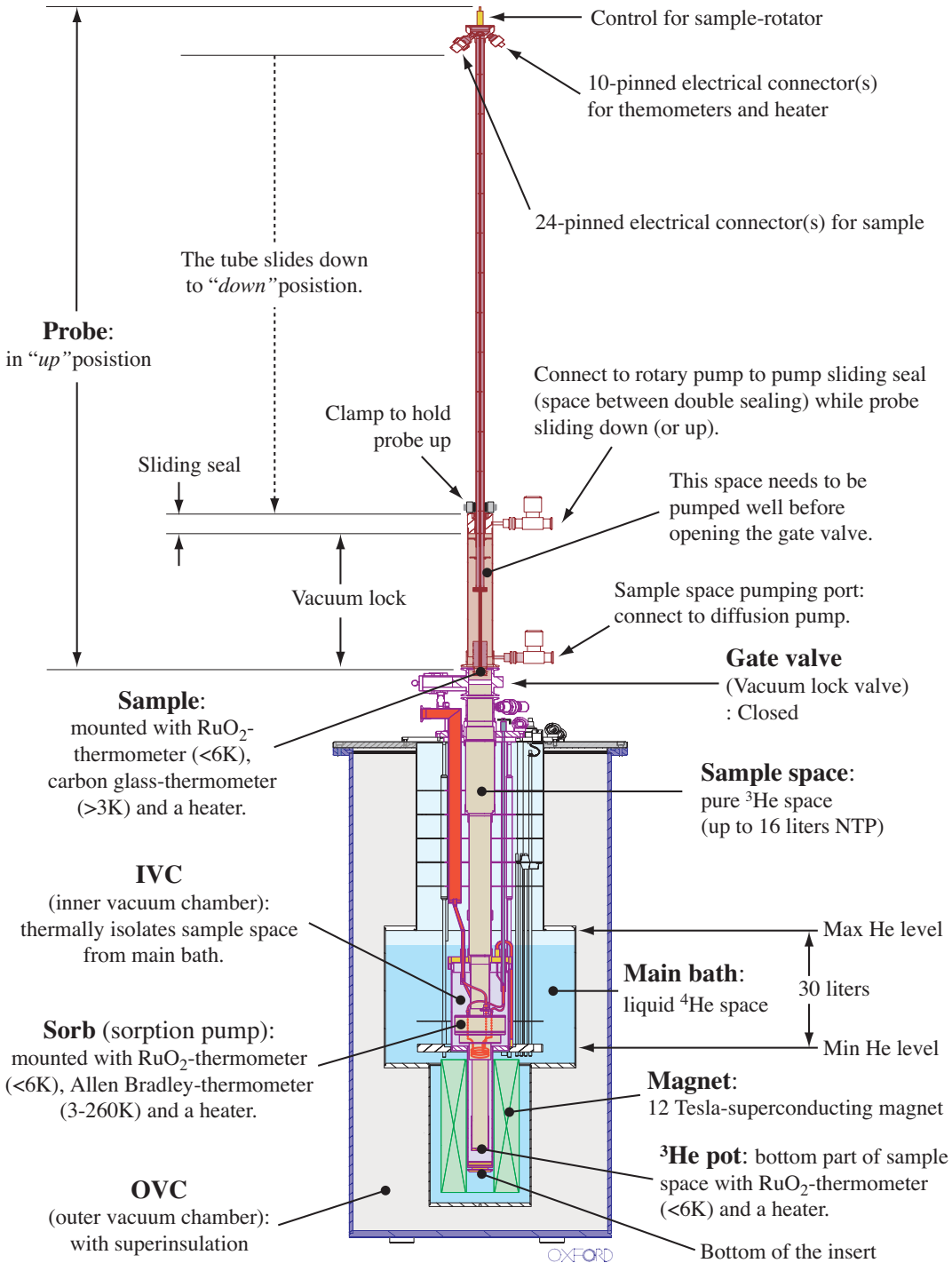

Figure 69: A schematic diagram for ^{3}He cryostat with the probe in *"up"* position (see text).

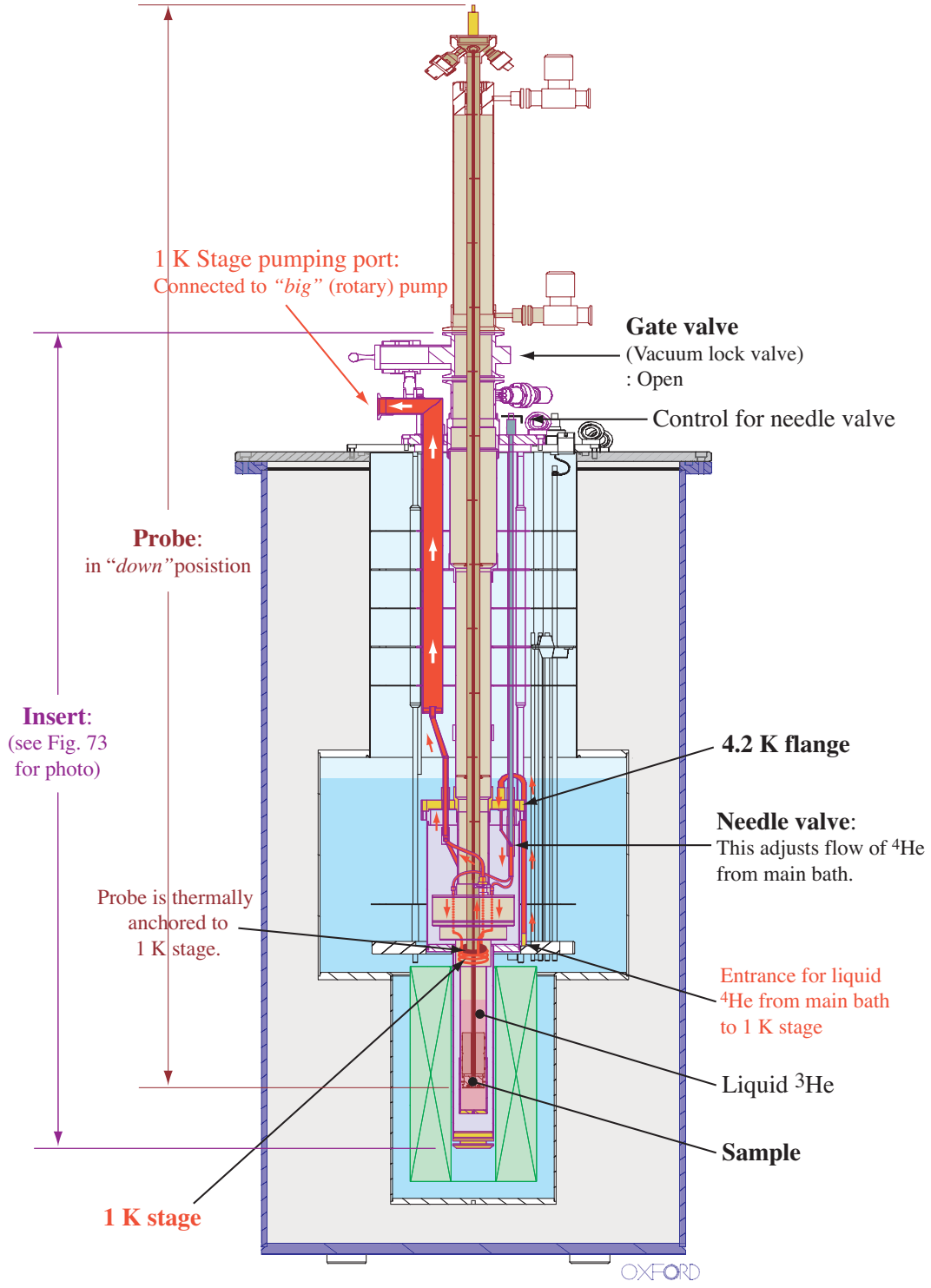

Figure 70: A schematic diagram for ^{3}He cryostat with the probe in *"down"* position (see text).

thermal conduction with the sample directly immersed in liquid ^{3}He. Cooling down below 1.4 K is done via a one-shot cycle which ends when all the accumulated liquid ^{3}He has evaporated. The holding time can be more than 10 hours at the base temperature depending on the heat-load of the measurement. The top-loading capability allows us to change samples in a few hours, while the system is kept at liquid helium temperature.[51]

Fig. 68 shows a photograph and Fig. 70 shows a schematic of the ^{3}He cryostat with the probe in the *"down"* position. With this probe position, the sample is inside the cryostat and is ready for measurements. The blue cables shown on the left of the cryostat in Fig. 68 and on the right of the cryostat in Fig. 35 are shielded twisted pairs ("blue hose") that connect the amplifiers to the twisted pairs of constantan wires inside the cryostat. The constantan wires connect directly to the Hall sensor. Some pumping lines are connected in the right side of the probe. Fig. 69 shows the schematic for the system before lowering the probe. The probe (the upper part with brown outlines) is attached on the top of the system in the *"up"* position. The long inner tube (filled with darker reddish brown) slides down to the *"down"* position as shown in Fig. 70.

In both Fig. 69 and Fig. 70, the probe is shown with brown outlines, and the insert (see right side of the photograph in Fig. 73) is traced with purple outlines. In Fig. 69, the gate valve is still closed; the vacuum lock (space above the gate valve, shown in dark brown in the schematic) and the sample space (space below the gate valve, shown in light brown in the schematic) are separated. In Fig. 70, the gate valve is open and the probe has been lowered. The vacuum lock and the sample space are now connected and shown with light brown in the schematic. This chamber contains high purity ^{3}He.

[51] It takes two days to cool the cryostat from room temperature to 4.2 K. It takes about five days for the cryostat to naturally warm up from 4.2 K (starting with the liquid ^{4}He level at 0 %) to room temperature.

During the cooling cycle (see Fig. 71), liquid ^{3}He (shown in magenta in the schematic) accumulates at the bottom of the ^{3}He pot. The sample space is thermally isolated from the ^{4}He main bath by the inner vacuum chamber (IVC). The main bath is shown in light blue in the schematic. The IVC is shown in light purple. The outer vacuum chamber (OVC) with superinsulation (layers of material cooled by ^{4}He gas from the main bath)[52] thermally isolates the main bath from room temperature. The pumping line for the 1 K stage is shown in red in the schematic. In Fig. 70, red (or white) arrows show the direction of the pumping flow of ^{4}He from the main bath to the *"big"* pump. Fig. 75 shows the photographs of the 1 K-stage pumping line and red arrows indicate the direction of the flow of ^{4}He.

Fig. 71 shows schematic diagrams for the cooling cycle in the sample space. By pumping ^{4}He, the 1 K stage (red) can achieve 1.4 K continuously. At 1.4 K, the sorb can absorb up to 16 liters of ^{3}He (gas at atmospheric pressure). Cooling down below 1.4 K requires two steps. Fig. 71 (a) shows the first step. During this time, the sorb is warmed by an electric heater to $21 \sim 36$ K. At this temperature, the sorb releases most of the ^{3}He (magenta arrows) which will condense at the cold surface of the 1 K stage (1.4 K) and liquid ^{3}He (magenta) drops down to the bottom of the sample space, the ^{3}He pot. In the second step as in Fig. 71 (b), the heater at the sorb is turned off, and then the sorb starts to absorb ^{3}He (magenta arrows). As more ^{3}He is evaporated at the surface, the temperature of the remaining condensation in the ^{3}He pot goes down to the base temperature of 250 mK.

Fig. 72 shows the photograph of the top view of the ^{3}He cryostat. Fig. 73 shows the side view of the ^{3}He cryostat when we pulled the insert out for repair.[53] The insert is mounted in the main bath and is traced in purple in the schematic in Fig. 69

[52]This system is a vapor shielded dewar and does not have a nitrogen jacket. Nitrogen liquid is needed only for the initial cooling of the cryostat from room temperature.

[53]There was a small leak between the sample space and IVC. It was successfully repaired by ourselves.

and Fig. 70.

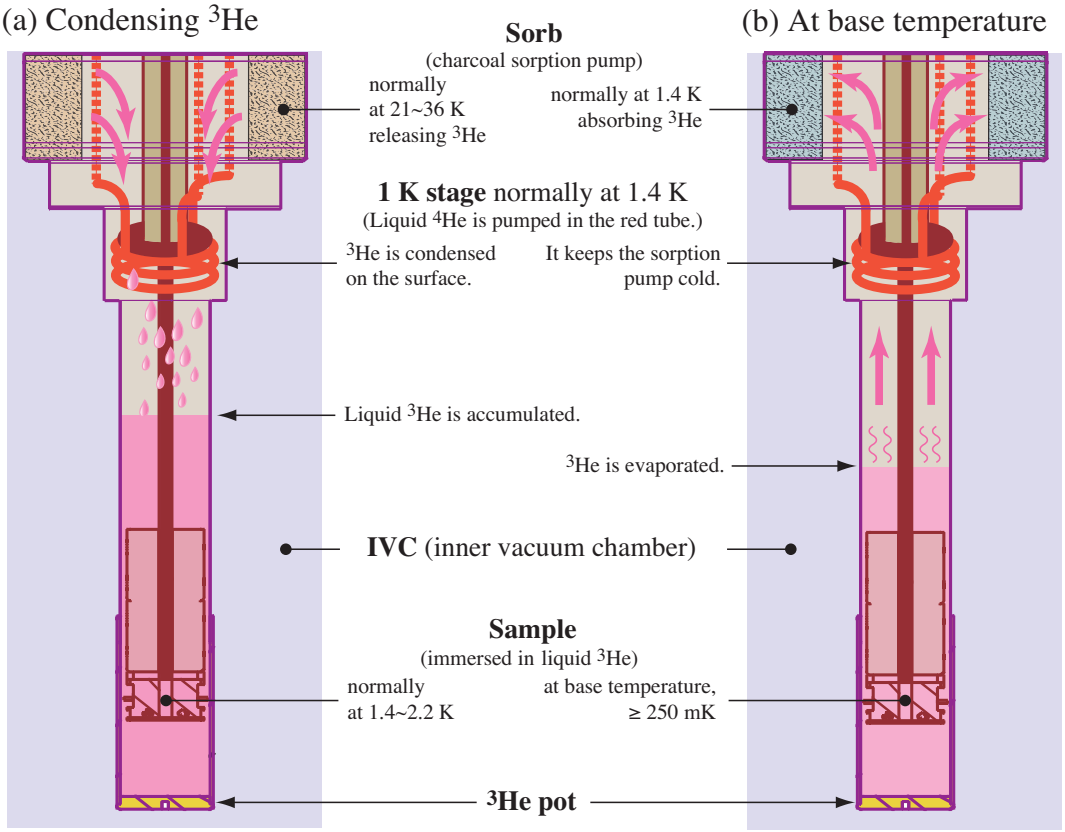

Figure 71: Schematic diagrams for cooling cycle in the sample space (pure ^{3}He space) are shown. By pumping ^{4}He, the 1 K stage (red) can achieve temperatures as low as 1.4 K continuously. At 1.4 K, The sorb can absorb up to 16 liters of ^{3}He (gas at atmospheric pressure). Cooling down below 1.4 K requires two steps: Step 1 (part **a** of figure), the sorb is warmed by an electric heater to $21 \sim 36$ K. At this temperature, the sorb releases most of the ^{3}He (magenta arrows) which will condense at the cold surface of the 1 K stage (1.4 K) and liquid ^{3}He (magenta) will drop down to the bottom of the sample space (^{3}He pot).[54] It normally takes about 30 minutes until the accumulation of liquid ^{3}He stops. Step 2 (part **b** of figure), the heater at the sorb is turned off and the sorb starts to absorb ^{3}He (magenta arrows). As more ^{3}He is evaporated from the surface of the ^{3}He liquid at the bottom, the temperature of the remaining condensation in the ^{3}He pot goes down to the base temperature of 250 mK. During this period, the lower the temperature of the sorb, the faster the sorb absorbs ^{3}He. For the base temperature, the sorb is cooled down to 1.4 K by the 1 K stage. When the measurements are performed at temperatures above 0.3 K (but still below 1.4 K), the temperature of the 1 K stage is raised or the sorb heater was turned on so that the sorb remains at a higher temperature (see also Ref. [189] Section 2.5).

[54] Normally, liquid ^{3}He starts to accumulate when the temperature of the ^{3}He pot goes down to 2.2 K.

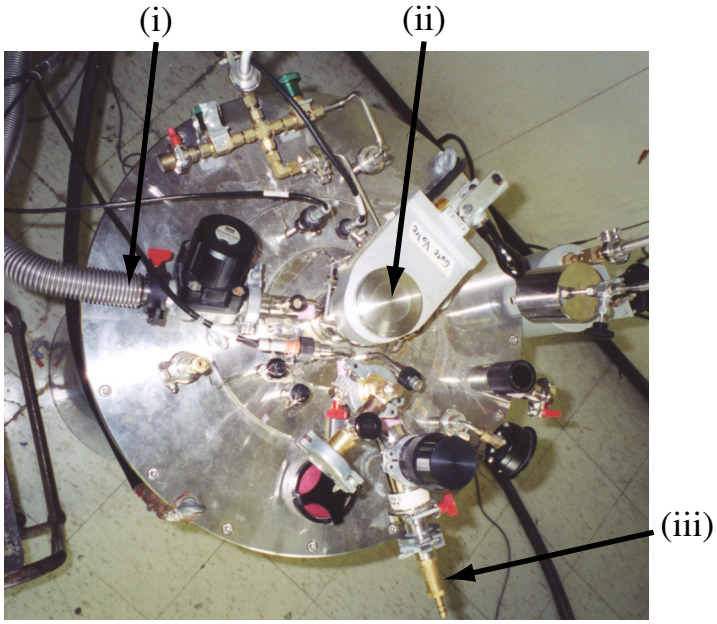

Figure 72: The top view of the ^{3}He cryostat. Label **(i)** indicates the 1 K stage pumping line which is connected to the *"big"* pump. Label **(ii)** indicates the top of the gate valve (vacuum lock valve). This is where the probe is inserted. Label **(iii)** indicates the one-way release valve for the main bath.

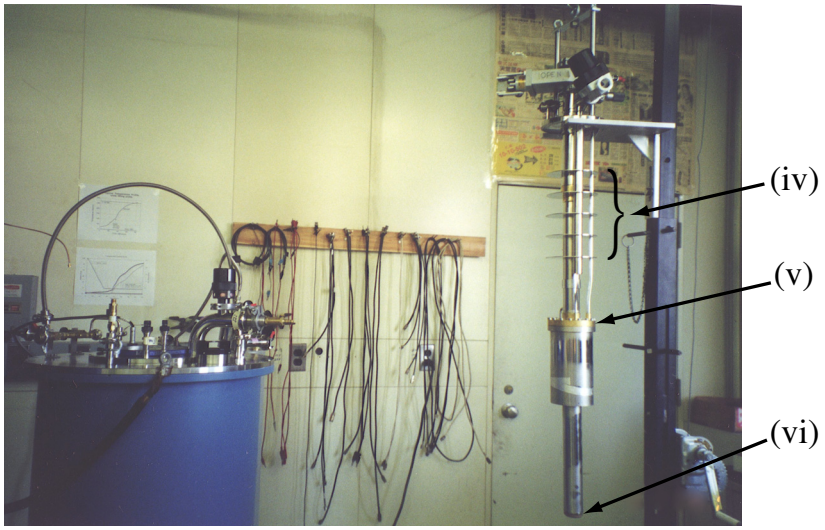

Figure 73: The side view of the ^{3}He cryostat with the insert pulled out. The insert (traced in purple in Fig. 70) is mounted in the main bath. Label **(iv)** indicates the location of the radiation baffles. Label **(v)** indicates the location of the 4.2 K flange. Label **(vi)** points to the bottom of the insert.

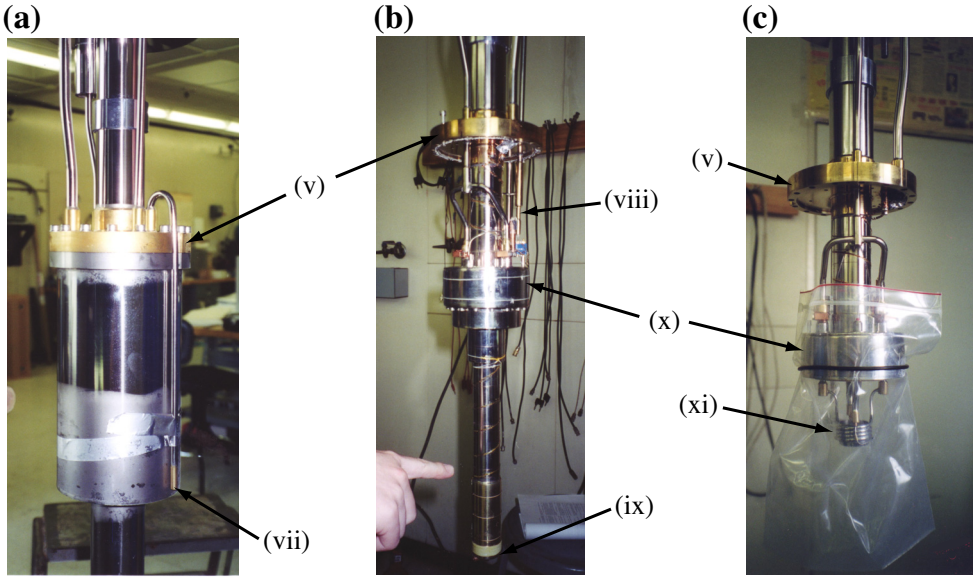

Figure 74: The indicated parts are: **(v)** - the 4.2 K flange; **(vii)** - the entrance for liquid ^{4}He from the main bath to the 1 K stage line; **(viii)** - needle valve; **(ix)** - bottom of the ^{3}He pot; **(x)** - sorb; and **(xi)** - 1 K stage. In part **(a)**, the middle part of the insert is shown. Below the brass 4.2 K flange, there is a layer (traced in purple below the 4.2 K flange in Fig. 70) which forms part of the outer wall of the IVC. In part **(b)**, the inside of the IVC is shown after the outer wall of the IVC is taken off. There is another smaller tail (^{3}He pot) inside the IVC. The interior of the ^{3}He pot forms the sample place and the bottom of this chamber is where ^{3}He accumulates (see Fig. 71). In part **(c)**, the 1 K stage is shown after the ^{3}He pot was taken off. The sample space was exposed to air and a plastic cover was placed over the sorb to limit the amount of moisture accumulation.

The photographs in Fig. 74 and Fig. 75 were also taken during the repair. Fig. 74 (a) shows the middle part of the insert. Below the brass (4.2 K) flange, there is a layer (traced in purple below the 4.2 K flange in Fig. 70) which is also the outer wall for the IVC. (b) shows what is inside the IVC.[55] Inside the IVC, there is another smaller tail. Inside of this is the sample place. The bottom part is the ^{3}He pot where ^{3}He condenses (see Fig. 71). (c) shows the 1 K stage after removing the tail shown in (b).

Fig. 75 shows precisely how the ^{4}He flows from the entrance in the main bath (vii) through the 4.2 K flange (v) into the IVC. Once inside the IVC, the flow is regulated by a needle valve (viii) before entering the 1 K stage (xi). Before entering and after leaving the 1 K stage, the ^{4}He travels through the sorb which provides the

[55] Indium was used for all the inner vacuum seals.

sorb with cooling power. The ^{4}He then travels back through the 4.2 K flange and out of the system entirely to the *"big"* pump.

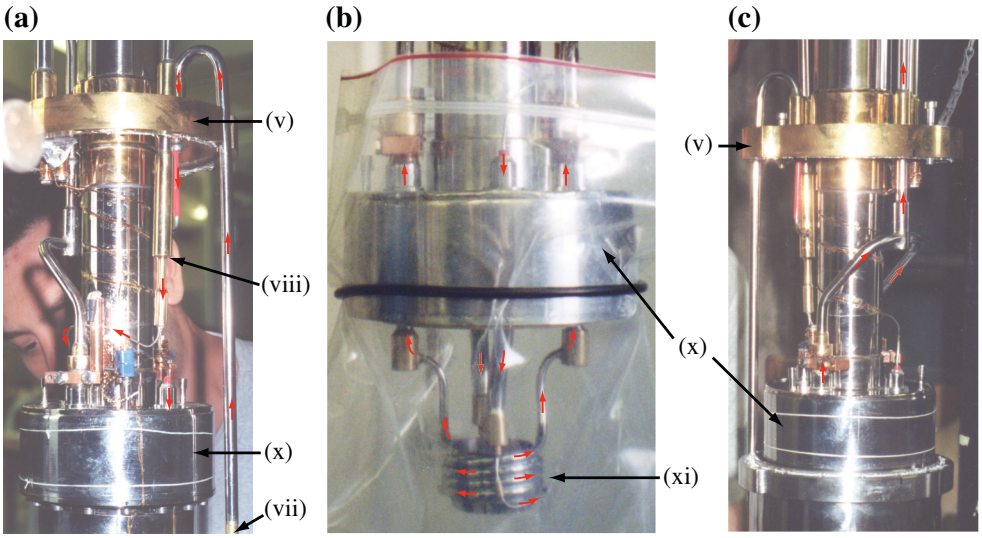

Figure 75: These three photographs show precisely how the 1 K stage pumping line is arranged and liquid ^{4}He is pumped out from the main bath through the IVC to the *"big"* pump. The red arrows shows the direction of ^{4}He flow. The labeled parts are: **(v)** - 4.2 K flange; **(vii)** - filtered entrance for liquid ^{4}He from the main bath to the 1 K stage; **(viii)** - needle valve; **(x)** - Sorb; and **(xi)** - 1 K stage. Part **(a)** shows the ^{4}He flow from the main bath **(vii)** through the 4.2 K flange **(v)** into the IVC. Once inside the IVC, the flow splits below **(viii)** before entering the sorb **(x)**. Part**(b)** shows the ^{4}He flow through the sorb**(x)** and 1 K stage **(xi)**. Below the sorb, the two tubes circle around a couple of times making a coil which acts as the 1 K stage. During the condensing stage, ^{3}He condenses on the surface of the coil and drips off the knife edge formed at the bottom of the 1 K stage. Part **(c)** shows the ^{4}He flow out of the sorb where it is rejoined into one tube before exiting the IVC through the 4.2 K flange and out through the the pumping port to the *"big"* pump (see Fig. 70).

4.2 Hall Sensors

Micro Hall sensor-arrays were used to probe the local magnetization of samples. Using GaAs wafers grown by H. Shtrikman, the Hall sensors were fabricated and provided by N. Avraham, Y. Myasoedov and Y. Paltiel of Eli Zeldov's group at the Weizmann Institute of Science, Israel. They have the technology to manufacture the arrays in various sizes and configurations. These sensors enable us to probe the locally varying magnetization of the samples with high resolution in the time-domain. Chang, *et al.* first applied such small Hall bars as local field sensors for their scanning Hall probe microscope [190].

4.2.1 Configuration

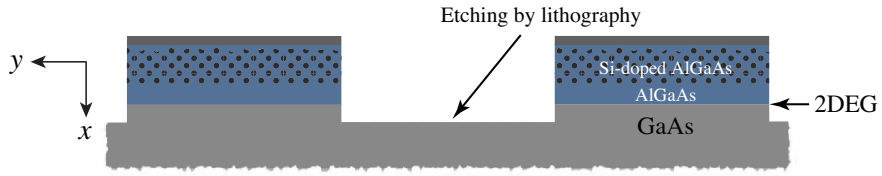

Figure 76: The array of Hall sensors were fabricated by lithography on GaAs/AlGaAs heterostructures which forms a two-dimentional electron gas (2DEG) at the interface. Using molecular beam epitaxy, a thin layer (10 nm) of undoped $Al_{0.3}Ga_{0.7}As$ was grown on the (001) oriented undoped GaAs substrate, followed by a Si-doped $Al_{0.3}Ga_{0.7}As$ layer which provides the carriers for the 2DEG.

The array of Hall sensors were fabricated by lithography on GaAs/AlGaAs heterostructures which form a two-dimentional electron gas (2DEG) at the interface (see Fig. 76). Using molecular beam epitaxy, a thin layer (10 nm) of undoped $Al_{0.3}Ga_{0.7}As$ was grown on the (001) oriented undoped GaAs substrate, followed by a Si-doped $Al_{0.3}Ga_{0.7}As$ which provides the carriers for the 2DEG [191, 192]. Fig. 77 shows a photograph of the top view of the Hall sensor array. The 2DEG is oriented in the yz-plane. The excitation current, I_{exc} was applied parallel to the z-axis. The Hall sensors are insensitive to magnetic fields parallel to the yz-plane. In the detailed view,

the shaded areas designate the Hall sensors. The Hall voltage, V_H is proportional to the perpendicular component of the magnetic field, B_x under the assumption that B_x is uniform over the Hall sensor. In these photographs, relatively large sensors ($30 \times 30\,\mu m^2$ with the $50\,\mu m$ interval) are shown.

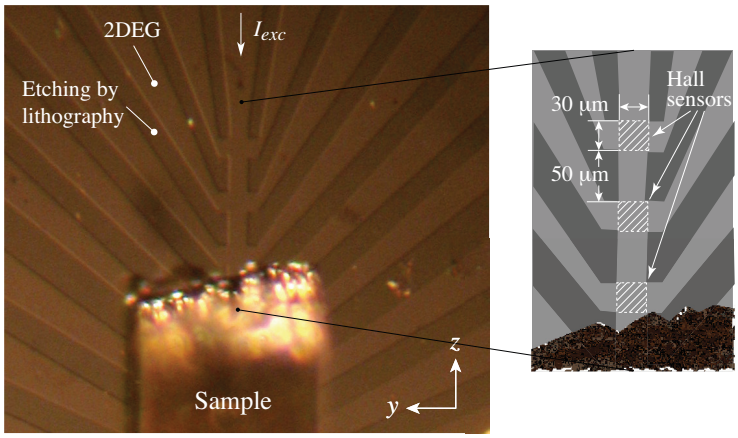

Figure 77: A photograph of the top view of the Hall sensor array with relatively large sensors ($30 \times 30\,\mu m^2$ with a $50\,\mu m$ interval) is shown. The 2DEG is oriented in the yz-plane. The excitation current, I_{exc} was applied parallel to the z-axis. The Hall voltage, V_H is proportional to the perpendicular magnetic field, B_x. Each sensor probes the approximately uniform magnetic field, B_x in each shaded area (as shown in the detailed view).

The electric resistance of the Hall sensor array is typically a few $\mathrm{k}\,\Omega$. The Hall mobility of the 2DEG at low temperature is about $1 \times 10^5\,\mathrm{cm^2V^{-1}s^{-1}}$ and the carrier concentration is about $6.25 \times 10^{11}\,\mathrm{cm^{-2}}$ which gives 0.1 Ω/Gauss for the Hall coefficient [193, 194]. The Hall voltage, V_H, is related to the external field, B_x, by

$$V_H = B_x R_H I_{exc}\,, \tag{24}$$

where R_H is the Hall coefficient and I_{exc} is the excitation current. There is almost no temperature dependence of R_H in the measurement temperature regime between 0.3 K to 15 K (see also Ref. [189] Section 2.6). R_H is independent of I_{exc} up to 0.1 mA. At low temperatures due to the quantum Hall effect, the linearity of the Eq. 24 deviates at $B_x > 5000$ Gauss. The sample was mounted approximately $0.1\,\mu$m above the 2DEG.

Fig. 78 shows a photograph of the top view of the Hall sensor chip. The array of 21 Hall-sensors of $30 \times 30\,\mu m^2$ with $50\,\mu m$ interval is placed in the middle of the chip along the z-axis. Each terminal is connected to the ohmic contact pad at the edge of the chip. The Hall-sensor chip was mounted on the chip carrier with 24 connections (see Fig. 79). Only every other sensor is connected by gold lead bonding to an ohmic contact pad due to the limited number of connectors on the chip carrier. In the detailed schematic at the right, V_1, V_2,....., V_{11} label each Hall sensor. The Hall sensor array is oriented along the z-axis and provides the local magnetization variation.

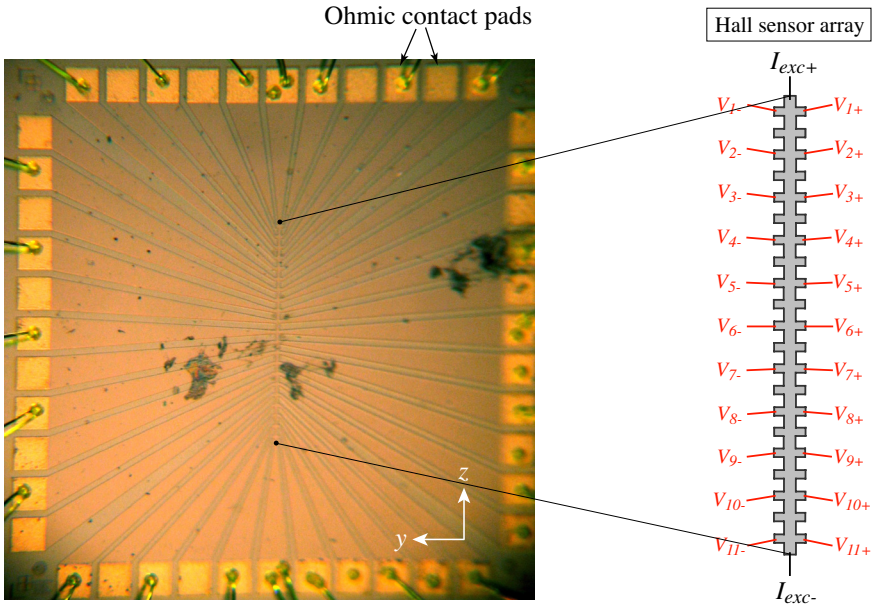

Figure 78: A photograph of the top view of the Hall-sensor chip is shown. The array of 21 Hall-sensors of $30 \times 30\,\mu m^2$ with $50\,\mu m$ interval is placed in the middle of the chip along the z-axis. Each terminal is connected to an ohmic contact pad at the edge of the chip. Only every other sensor is connected by gold lead bonding to the ohmic contact pads (see also Fig. 79). The right hand side shows the sensor designations, V_1, V_2,....., V_{11} used to label the local Hall-sensor responses at the different positions along the z-axis.

Fig. 80 (a) shows the sample space at the bottom of the probe with only the connector for the Hall-sensor chip carrier mounted. (b) shows the Hall sensor chip carrier (with a sample and a thermometer) mounted on the the connector. The ex-

ternal magnetic field, H_{ext} is applied vertically (along the z-axis as shown in Fig. 78). The Hall sensors are insensitive to the parallel magnetic field. Therefore, the signal primarily comes from the sample. The rotator can rotate the sensors around the y-axis (see Fig. 78) which provides the means to achieve even more perfect alignment ($\theta = 0$ in Fig. 81 (a)) between the Hall sensors and the external magnetic field. Please note with external magnetic field as large as 6 T, even very small misalignment will lead to the situation where the Hall voltage due to the external field easily exceeds the one from the sample. This precise rotational adjustment eliminates the background signal from the external field (for more details see Section 4.2.2). For the case of $\theta \neq 0$, the Hall sensors will detect the external magnetic field as well as the sample signal. In (c), the Hall sensor was rotated by 90° relative to the position in (b).

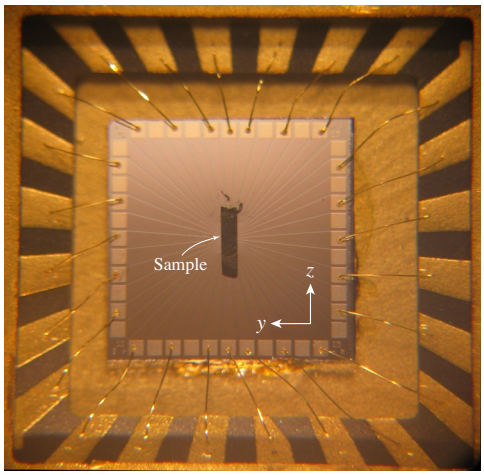

Figure 79: The Hall-sensor chip was mounted on the chip carrier with 24 connections. 11 Hall-sensors and the excitation current contacts were connected by gold lead bonding to the chip carrier. A Mn_{12}-acetate crystal was mounted on the Hall sensor array with the easy axis along the z-axis.

In Fig. 81 (a), the direction of rotation for the Hall-sensor chip relative to the external magnetic field is shown when the chip is mounted on the probe as in Fig. 80 (a)-(c). The rotation axis for the Hall-sensor chip is the y-axis. The rotator is used to align the Hall sensor chip parallel to the external magnetic field, H_{ext} so that $\theta = 0$.

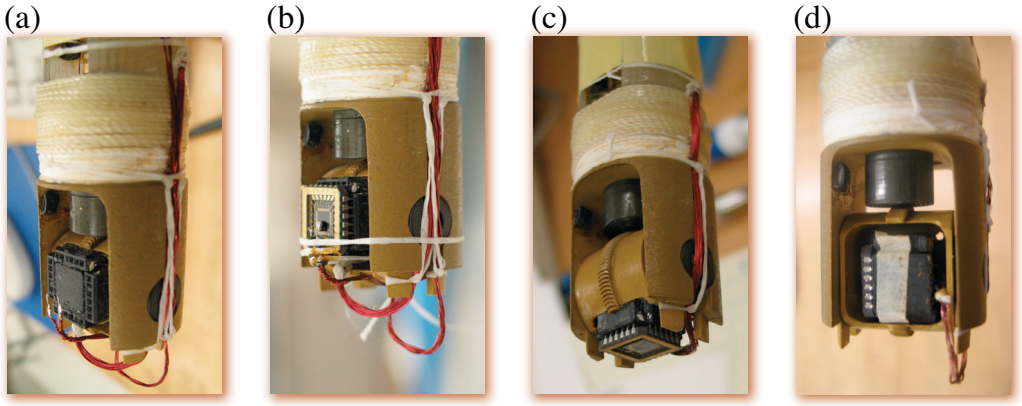

Figure 80: **(a)** The sample space at the bottom part of the probe is shown with the connector for the Hall-sensor chip carrier. **(b)** The Hall sensors with the sample mounted on the the connector. The external magnetic field is applied vertically (along the z-axis in Fig. 78). **(c)** The Hall sensor was rotated by 90° relative to the position in (b). **(d)** The alternative way of mounting the Hall-sensor chip.

Otherwise the Hall sensors would detect the external magnetic field as well as the sample signal. Then Hall voltage is given by,

$$V_H = R_H I_{exc}(B_{x,sample} + \mu_0 H_{ext} \sin\theta)\,. \tag{25}$$

As in Fig. 79, a Mn_{12}-acetate crystal was mounted on the Hall sensor with the easy axis parallel to the Hall sensor surface. Since the sample is mounted with its easy axis flush to the surface of the Hall sensor and parallel to the z-axis, then as long as the Hall sensor is aligned along the external field, the easy axis will also be aligned.[56] This configuration only works for studying the longitudinal magnetic field dependence. When the transverse magnetic field needs to be applied to the sample (as is the case of the measurements in Section 3.2.3), the Hall sensors should be mounted on the probe so that the x-axis is the rotation axis. Fig. 81 (b) shows the alternative direction of rotation when the Hall-sensor chip is mounted as shown in Fig. 80 (d) with $\theta \approx 0$[57]. It is mounted on the probe so that the rotation axis for the Hall-sensor

[56]The easy axis of the sample was aligned along the z-axis by eye.

[57]One of the disadvantages in this method is that misalignment in θ can not be completely removed. However, normally the sample signal doesn't contain a linear component. Therefore, it is easy to subtract the the second term in Eq. 25 (see Ref. [189] Section 2.7).

chip is along the x-axis. In this way, the orientation of the external magentic field changes within the yz-plane. The rotational dependence of ϕ on the sample can be studied without losing the sensitivity of the sample signal. This method was used for the measurements in Section 3.2.3.

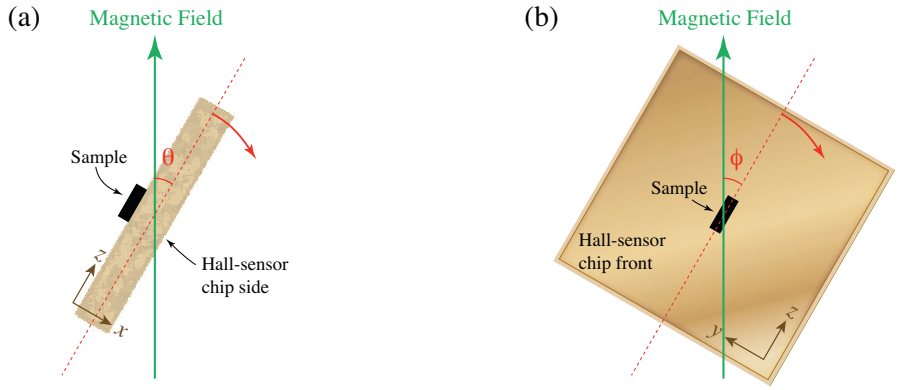

Figure 81: **(a)** The direction of rotation for the Hall sensor chip relative to the external magnetic field is shown. The chip was mounted on the probe as in Fig. 80 (a)-(c). The rotation axis for the Hall sensor chip is the y-axis. **(b)** The alternative direction of rotation is shown when the Hall-sensor chip is mounted as in Fig. 80 (d) with $\theta \approx 0$. The rotation axis for the Hall-sensor chip is the x-axis. In this way, the orientation of the external magentic field changes within the yz-plane.

4.2.2 Calibration and Background

Without any sample mounted, Hall voltages of the top two Hall sensors in the sensor array ($30 \times 30\,\mu m^2$ with $50\,\mu m$ interval) in Fig. 78 were measured and are plotted as a function of the external magnetic field in Fig. 82. The sensors were mounted in the position shown in Fig. 80 (c) with the external magnetic field oriented along the vertical direction. Therefore, the direction of the external magnetic field was perpendicular to the Hall sensors, i.e. $\theta = 90°$ (see Fig. 81). From the slope of the best linear fit, it was determined that, $R_H = 0.1087\ \Omega$/Gauss.[58]

[58]The offsets of the linear fits most likely came from the longitudinal resistance which arose from the relative vertical misalignments of the position of V_+ and V_-. The longitudinal resistance does not depend on the magnetic field. Therefore, it appears as a constant offset in the magnetic field sweeps.

In Fig. 83 with the sensor orientation at $\theta \approx 9.4°$ as shown in Fig. 81 (a), the Hall voltage was measured while the external magnetic field was swept from zero to 5 T with $I_{exc} = 50\,\mu$A. The values were subtracted by the best fit line and the non-linear component is plotted in the inset (blue curve). This non-linear component was mostly due to the electromagnetic induction from the change in the external magnetic field (see Fig. 84). Remanent or dipole magnetic fields by the magnetized surrounding materials also contributes to the non-linear component.

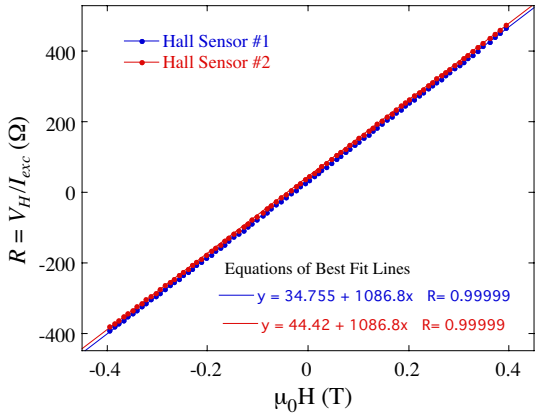

Figure 82: Without any sample mounted, Hall voltages of the top two Hall sensors in the sensor array ($30 \times 30\,\mu m^2$ with $50\,\mu m$ interval) as shown in Fig. 78 were measured and are plotted as a function of the external magnetic field. The sensors were mounted in the position shown in Fig. 80 (c) with the external magnetic field oriented in the vertical direction. Therefore, the direction of the external magnetic field was perpendicular to the Hall sensors, i.e. $\theta = 90°$ (see Fig. 81 (a)). From the slope of the best linear fit, $R_H = 0.1087\ \Omega$/Gauss.

With the sensor orientation at $\theta \approx 4.2°$ as shown in Fig. 81 (a), Fig. 84 shows the measured Hall voltage while the external magnetic field was swept from -6 T to 6 T and 6 T to -6 T (field sweep direction is shown by blue arrows) with external magnetic sweep rates of 10 , 20, 30 and 40 mT/s. In these measurements, $I_{exc} = 1.0\,\mu$A. The values were subtracted by the best fit line and the non-linear components are plotted in the inset (with the field sweep direction indicated by red arrows). When the magnetic field was swept upward (downward), the measured voltages were shifted down (up) by constant values which are larger for larger magnetic field sweep rate.

This effect originates from the electromagnetic induction due to the time rate of change in the external magnetic field. The voltage shifts depend only on the magnetic field sweep rate and not on I_{exc}. Since V_H is proportional to I_{exc} the voltage shifts become negligible compared to V_H when I_{exc} is large. When small I_{exc} was used, the constant shift was subtracted from the data.

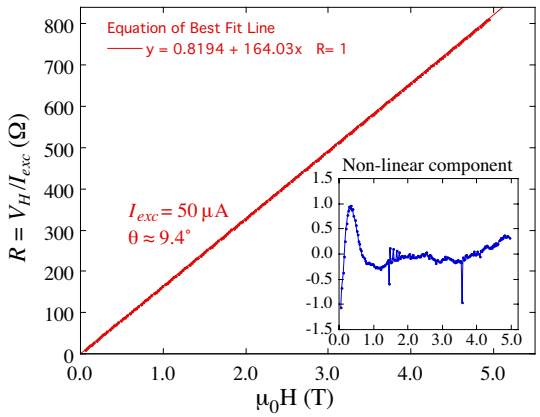

Figure 83: With the sensor orientation at $\theta \approx 9.4°$ as shown in Fig. 81 (a), the Hall voltage was measured while the external magnetic field was swept from zero to 5 T with $I_{exc} = 50\,\mu$A. The values were subtracted by the best fit line, and the non-linear component is plotted in the inset (blue curve).

In Fig. 85, the temperature increases of the sample relative to the bath temperature when the bath was held at the base temperature of ~ 0.3 K is plotted as a function of excitation current of the Hall-sensor array. The sample temperature was measured as in Fig. 64. The Hall sensor-array with 21 $10 \times 10\,\mu m^2$ sensors with $10\,\mu m$ interval was used. The total length of the array was $210\,\mu$m. The total resistance of the array and its contacts was 2.7 K Ω. The calculation shows that a current of 1, 10, 30 and $50\,\mu$A would produce 2.7 nW, 270 nW, 2.43 μW and 6.75 μW for heat respectively. Since the sample was mounted directly on the sensor array, some parts of it might have experienced higher temperature than what was measured in Fig. 85. For the measurements on the normal magnetization curves with Mn_{12}-acetate, the hyteresis curves show no temperature dependence below 0.6 K since all the relaxations proceed

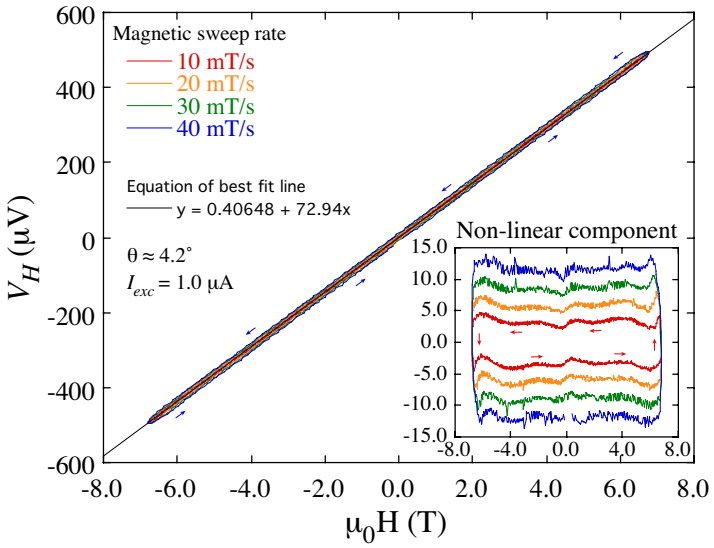

Figure 84: With the sensor orientation at $\theta \approx 4.2°$ as shown in Fig. 81 (a), the Hall voltage was measured while the external magnetic field was swept from -6 T to 6 T and 6 T to -6 T (with the field sweep direction indicated by blue arrows) with different external magnetic sweep rates. In these measurements, $I_{exc} = 1.0\,\mu$A. The measured values were subtracted by the best fit line and the non-linear components are plotted in the inset (with the field sweep direction indicated by red arrows).

from the ground state.[59] In this case, a larger current was used to take advantage of the larger signal-to-noise ratio. However, for the measurements with avalanches, a smaller current was used since the mechanism for triggering avalanches was unknown and there is possibility that heating from the excitation current in the Hall sensor might have played a role.

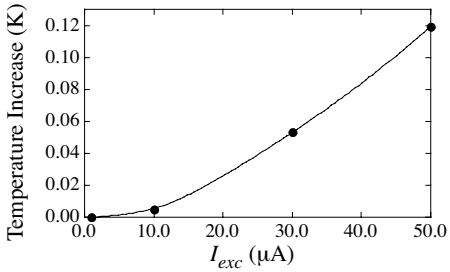

Figure 85: The temperature increases of the sample relative to the bath temperature when the bath was held at the base temperature of ~ 0.3 K are plotted as a function of excitation current of the Hall-sensor array. The sample temperature was measured as illustrated in Fig. 64.

[59] This was confirmed with a small excitation current.

4.3 Other Techniques

4.3.1 Samples and Preparation

Samples were grown and provided by N. E. Chakov in the group of G. Christou at the University of Florida at Gainesville as well as E. M. Rumberger in the group of D. Hendrickson at the University of California at San Diego. Mn_{12}-acetate was first synthesized by Lis [3]. Later, relatively larger single crystals of Mn_{12}-acetate became available. Fig. 86 (a) shows a relatively large crystal of Mn_{12}-acetate. The Mn_{12}-acetate has tetragonal symmetry (see Section 2.1) and crystalizes into a rather long rectangular shape. The magnetic easy axis (blue arrow) is along the long crystal c_c-axis; a_c and b_c are equivalent to each other by symmetry. The $a_c c_c$-plane and the $b_c c_c$-plane are perpendicular to each other. Fig. 86 (b) shows a crystal of Fe_8. The magnetic easy axis (blue arrow) lies 0.7° away from the $a_c b_c$-plane and 16° away from the a_c-axis in the $a_c b_c$-plane. [195]

Figure 86: **(a)** A relatively large crystal of Mn_{12}-acetate is shown. The Mn_{12}-acetate has tetragonal symmetry (see Section 2.1) and crystalizes into a rather long rectangular shape. The magnetic easy axis (blue arrow) is along the long crystal c_c-axis. **(b)** A crystal of Fe_8 is shown. The magnetic easy axis (blue arrow) lies 0.7° away from the $a_c b_c$-plane and 16° away from the a_c-axis in the $a_c b_c$-plane. [195]

As in Fig. 87 (a), normally the sample was directly mounted on the Hall-sensor chip. The white chunk in the left side of the picture is Eicosene (a kind of bee's wax) which melts at a temperature a little higher than room temperature. A small amount of it was applied next to the sample and was heated up by a light bulb for

Figure 87: **(a)** The sample was normally directly mounted on the Hall-sensor chip (see Fig. 78). The white chunk in the left side of the picture is Eicosene (a kind of bee's wax). which melts at a temperature a little higher than room temperature. A small amount of it was applied next to the sample and was heated up by a light bulb for a short time until it was melted. **(b)** Once the Eicosene melts, it surrounds the sample and holds it fixed to the sensor.

a short time until it melted and surrounded the crystal as in Fig. 87 (b). After that it was cooled down to the measurement temperature. Eicosene was used to hold the sample in place and also to protect the crystal from losing its solvents. Many other substances such as grease, paraffin, Stycast and other kind of waxes and oils were also used instead of Eicosene. The choice of glue was made by considering the desirability of certain conditions of the sample during the measurements such as good thermal conductivity, higher stresses or adhesiveness.

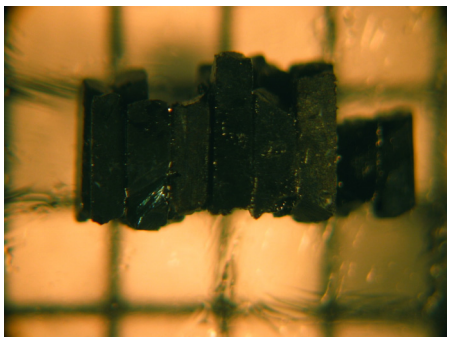

Figure 88: Many crystals of Mn_{12}-acetate were carefully chosen, oriented along the easy axis and glued together with Stycast 1266A one by one for optical measurements which require larger sample size. The grid ($1 \times 1\,mm^2$) drawn behind the glass plate was used as an alignment guide. There was a layer of grease between the glass plate and the sample so that samples would not be glued to the glass plate.

In Fig. 88, many crystals of Mn_{12}-acetate were carefully chosen, oriented and

glued together with Stycast 1266A one by one for optical measurements which require larger sample size. This procedure was continued until it made a $(1 \times 1)\,\mathrm{cm}^2$ cross section in the hard plane. Thesis large assemblies of crystals were used for optical measurements.

4.3.2 Thermometer

The temperature of the samples was measured by a ruthenium oxide thermometer (see Fig. 89) which was directly mounted on the sample as in Fig. 64. Its resistance has a small magnetic field dependence and has high sensitivity between 0.05 K and 200 K. This bare chip model has a faster response time and a smaller mass compared to the other forms.

Figure 89: The dimensions for bare chip model of ruthenium oxide thermometer (RX-102A-BR by Lake Shore) are shown. The active surface (thick film) was directly mounted on the sample to measure the temperature as shown in Fig. 64.

4.3.3 Electronics for Fast Measurements

For the measurements in Section 3.3, electronics needed to be prepared for the measurement of signals varying as fast as $\sim 1\,\mathrm{MHz}$ with μV precision. Fig. 90 shows the electronics circuit design for a precision DC current source using **REF102** (a 10 V voltage reference) from Texas Instruments. The 9 V batteries were used to power both the **REF102** voltage reference and **OPA227** op-amp. For the measurements in Section 3.3, $R = 5\,\mathrm{M}\,\Omega$ was used to produce $I_{exc} = 2\,\mu\mathrm{A}$ for the Hall-sensor array. For the ruthenium oxide thermometer, $R = 20\,\mathrm{M}\,\Omega$ was used to get $I_{exc} = 0.5\,\mu\mathrm{A}$.

In Fig. 91, the electronics circuit design for a signal amplifier is shown. The 9 V batteries with $0.1\,\mu$F decoupling capacitors were used as very quiet and stable power for all **OPA228** (high precision and low noise op-amp). The **OPA228** has higher

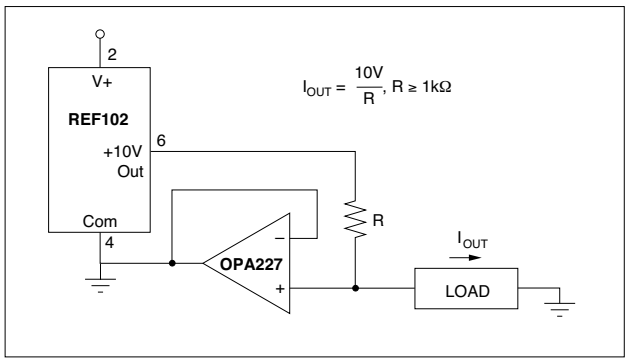

Figure 90: The electronics circuit design for a precision DC current source using a **REF102** 10 V voltage reference from Texas Instruments is shown. 9 V batteries were used to power both the **REF102** voltage reference and the **OPA227** op-amp.

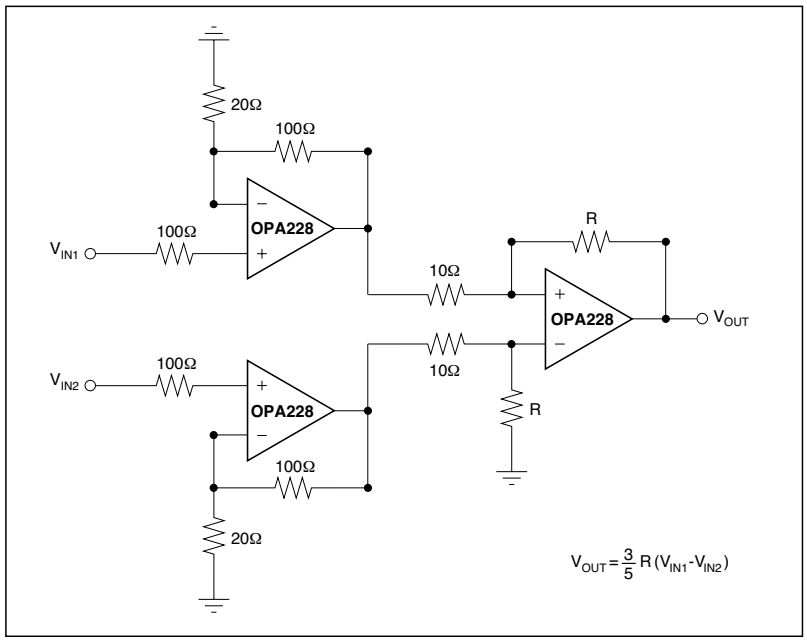

Figure 91: The electronics circuit design for a signal amplifier is shown. 9 V batteries with 0.1 μF decoupling capacitors were used as very quiet and stable power supply for all **OPA228** high precision, low noise op-amps. In this circuit, the sample signals, V_{IN1} and V_{IN2} were first amplified separately with standard non-inverting amplifiers each with a gain of $G = 6$ and connected to a differential amplifier with gain of $R/10$. [196]

speed with a slew rate of 10 V/μs and a bandwidth of 33 MHz. It is optimized for closed-loop gains of five or greater. In this circuit, the sample signals, V_{IN1} and V_{IN2} were first amplified separately with standard non-inverting amplifiers, each with a gain of $G = 6$, and connected to a differential amplifier with gain $R/10$. [196]

For the measurements in Section 3.3, $R = 2\,\mathrm{K}\,\Omega$ was used to produce the total gain of 1200 for the Hall sensors. The constant reliable gain of this amplifier circuit was tested for the input signal ranging from $1\,\mu$V to $300\,\mu$V. It performed well in spite of its relatively lower common-mode rejection ratio (CMRR)[60], as shown in Fig. 92. The linearity (constant gain) was also tested with the Hall voltage, various I_{exc} and the external magnetic fields. In order to take full advantage of the high gain band width of **OPA228**, the signal was amplified in two stages. The amplified signals had a delay time of $\sim 1\,\mu$s. The entire measurement setup (including the Hall sensors, cables, amplifiers and digital scopes) registered a total delay time of $\sim 2\,\mu$s.

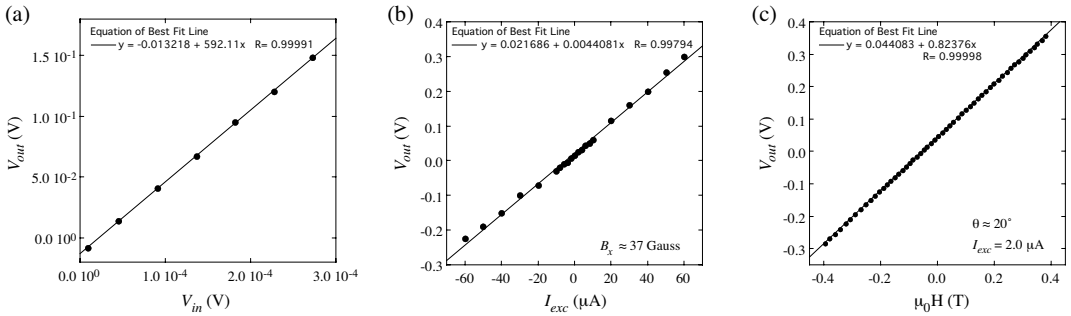

Figure 92: (a) The amplifier output, V_{out} plotted as a function of a small known DC voltage, V_{in} at room temperature. $R = 1\,\mathrm{K}\,\Omega$ was used for the circuit in Fig. 91 to produce a total gain of $G = 600$. (b) Different values of I_{exc} were applied to the Hall sensor in the cryostat at $\sim 7\,\mathrm{K}$. A magnetic field of $\sim 37\,\mathrm{Gauss}$ was applied parallel to the Hall sensor. The Hall voltage was amplified 1200 times. (c) Amplified Hall voltage as a function of external magnetic field with the Hall sensor oriented at $\theta = 20°$. The quality of the linear fit proves the linearity of both the Hall sensor and the amplifier.

The electric circuit was built on a breadboard in Fig. 93. The Hall sensor signals were connected to the amplifier through twisted-pair wires with shielded twin-ax cables. Twisted-pair wires can carry electric signals as fast as a few MHz. The whole

[60]Before this design, more ideal instrumentation amplifiers with very high CMRR were built and performed well for testing. However, when they were connected to the Hall-sensor array, there was unintentional resonance or feedback which built up once in a while and produced large noise of a few KHz. While it was probably associated with the bias current, after many attempts and efforts in vain (such as using different op-amps, placing different capacitors in appropriate places and using different circuit boards including one with photolithography) to eliminate this, this design was abandoned and replaced with the one in Fig. 91.

circuit and the battery power were embedded in a cast aluminum box to isolate the amplifiers from electrical noise. The signal outputs were connected to digital scopes and a data acquisition card by coax cables. The typical background noise with 1 MHz bandwidth after amplification was $v_n \approx 10\,\mathrm{nV}/\sqrt{\mathrm{Hz}}$.

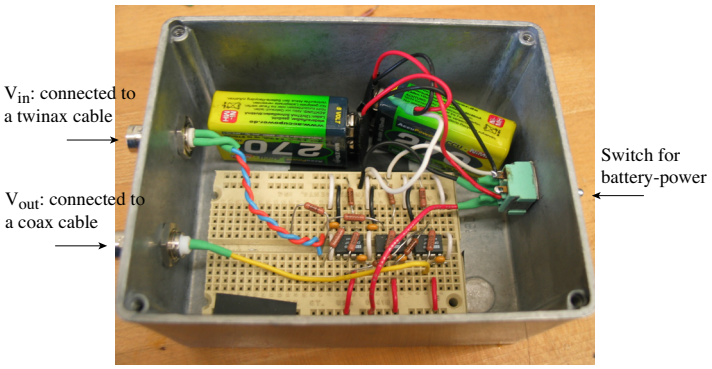

Figure 93: A picture of a signal amplifier with schematic circuit diagram shown in Fig. 91.

4.3.4 Data Acquisition

For the measurements in Section 3.3, the signals were recorded on three different time scales. The data acquisition card sampled all eight channels as fast as 10 KHz. It takes 40 minutes to measure the hysteresis curves (-6 T to 6 T and 6 T to -6 T) with a sweep rate of 10 mT/s as shown in Fig. 44. Without an avalanche event, averaged signals for 500 readings at 10 KHz sampling rate were recorded only every second in order to reduce the number of data points. The sampling rate of 1 Hz is enough to capture the magnetization relaxation with quantum tunneling. When an avalanche event occurred (such as the one at $\pm$ 4.2 T in Fig. 44), the data acquisition card was triggered to record the amplifier output voltages at a sampling rate of 10 KHz for one full second. One of the eight channels of the data acquisition card recorded the thermometer while the other seven recorded Hall voltages. Since heat diffusion after an avalanche was a rather slow process, this sampling rate and the recording time captured the temperature change after the avalanche well as can be seen in Fig. 67. It also recorded a more precise value of the external magnetic field at which

an avalanche occurred. Within the accuracy of the $100\,\mu$s averaging window, this corresponds to a field accuracy of $\sim 10^{-6}$ T. The 10 KHz sampling rate was not fast enough to capture an avalanche since the avalanche event occurred within $100\,\mu$s (the full width of each peak was about $60\,\mu$s as can be seen in Fig. 45). The same eight signals were also sampled by digital scopes at the higher sampling rate. The avalanche event triggered the scopes to record 2500 readings (or more depending on the ability of different scopes) with a typical sampling rate of 10 MHz (see Fig. 45 and Fig. 66).

4.4 Appendix

4.4.1 Magnetization Calculation for Mn_{12}-acetate

The saturated magnetization for S=10 in Mn_{12}-acetate was calculated, and this value was used for comparison with the measured values in Section 3.3.2. The magnetic moment of S=10 is:

$\mu = 2S\mu_B = 1.1577 \times 10^{-3}$ eV/T= 1.8548×10^{-22} J/T.

The saturation magnetization of Mn_{12}-acetate is:

$M = 2S\mu_B \times 2/a_L b_L c_L = 1.024 \times 10^5$ A/m, and $4\pi M = 1.29 \times 10^3$ Gauss, where $a_L = b_L = 1.73 \times 10^{-9}$ m and $c_L = 1.21 \times 10^{-9}$ m are the lattice constants for the body centered tetragonal lattice for Mn_{12}-acetate.

4.4.2 Calculation for Field Line Images

For illustrative purposes as shown in Fig. 61, the magnetic field lines for Mn_{12}-acetate can be calculated under a set of simplifying assumptions. For the case of avalanches, the marrow interface of the spin-up region and the spin-down region is approximate by the step function like two regions of oppositely polarized uniform magnetization. When calculating the vector potential, $\vec{A}(\vec{r})$, for a box shaped region, only the surface current terms are present, $\vec{A}(\vec{r}) = \oint_S \frac{\vec{M}(\vec{x'}) \times \vec{n}'}{|\vec{x} - \vec{x'}|} da'$. For a region with the magnetization oriented along the z-axis and a coordinate system chosen so that the yz-plane passes through the center of the region and is parallel to one of the surfaces of the region, then from symmetry considerations, only surface currents that run perpendicular to the $x = 0$ plane will contribute to the field in the $x = 0$ plane. For such a surface current running in the $\hat{x}$ direction, the vector potential is given by:

$$\vec{A}(x,y,z) =$$

$$\begin{bmatrix} -(y-y_0)\arctan\left[((x-x_i)(z-z_i))/((y-y_0)R_{ii})\right] \\ +(y-y_0)\arctan\left[((x-x_f)(z-z_i))/((y-y_0)R_{fi})\right] \\ +(y-y_0)\arctan\left[((x-x_i)(z-z_f))/((y-y_0)R_{if})\right] \\ -(y-y_0)\arctan\left[((x-x_f)(z-z_f))/((y-y_0)R_{ff})\right] \\ +(z-z_i)\log\left[x-x_i+R_{ii}\right]-(z-z_i)\log\left[x-x_f+R_{fi}\right] \\ +(x-x_i)\log\left[z-z_i+R_{ii}\right]-(x-x_i)\log\left[z-z_f+R_{if}\right] \\ +(z-z_f)\log\left[x-x_f+R_{ff}\right]-(z-z_f)\log\left[x-x_i+R_{if}\right] \\ +(x-x_f)\log\left[z-z_f+R_{ff}\right]-(x-x_f)\log\left[z-z_i+R_{fi}\right] \end{bmatrix} \times M\hat{x},$$

where $R_{ab} = \sqrt{(x-x_a)^2+(y-y_0)^2+(z-z_b)^2}$, y_0 is the location of the current sheet along the y-axis, and (x_i, z_i), (z_i, x_f), (x_f, z_i), and (z_f, x_f) demark the four corners of the current sheet. The magnetic field components in the $x = 0$ plane are given by: $B_x(0,y,z) = 0$, $B_y(0,y,z) = \partial A_x/\partial z$, and $B_z(0,y,z) = -\partial A_x/\partial y$. The field generated by a sample is then the sum of pairs of surface currents, one pair for each box shaped region of uniform magnetization.

To generate the field line images, the following intensity formula was used: $I(0,y,z) = I_0[|\vec{B}|(0,y,z) + s + 1 + \cos(\rho|\vec{A}|(0,y,z))]$, where $\rho = 19.5$ is the the field line density, $s = -2$ for points inside the sample, $s = 0$ for points outside the sample, and $I_0 = 9.0$ is a normalization constant that determines the brightness of the image. The intensity for each point in the $x = 0$ plane was then used to generate a false colored image for the field lines. The idea behind this method is that where the field strength is high, the brightness will be high. The field lines appear as a modulation of the intensity due to the $1 + \cos(\rho A_T(0,y,z))$ term. The false color function used in the images is given by:

$r = 0,\ g = 0,\ b = 0,$	$\{I^P < 0\}$	(black)
$r = 4I^P,\ g = 0,\ b = 0,$	$\{0 \le I^P < 1/4\}$	(black-red)
$r = 1,\ g = 4*(I^P - 1/4)/2,\ b = 0,$	$\{1/4 \le I^P < 3/4\}$	(red-yellow)
$r = 1,\ g = 1,\ b = 4*(I^P - 3/4)/2,$	$\{3/4 \le I^P \le 1\}$	(yellow-white)
$r = 1,\ g = 1,\ b = 1,$	$\{I^P > 1\}$	(white),

where r, g, b are the red, green and blue components of the color, I is the intensity given by the intensity formula, and P is a constant that determines the sharpness of the field lines. In the images appearing here, $P = 2$.

5 Conclusions

The aim of this thesis was to investigate magnetic avalanches in molecular magnets, a process that involves the abrupt and full reversal of the magnetization of a sample from one direction to the other in a very short time. Magnetic avalanches entail two distinct processes: nucleation (the triggering of an avalanche) and propagation (the dynamics of a self-sustaining avalanche). Here we summarize our findings regarding both processes.

We began our investigations by studying the magnetic fields and temperatures at which avalanches were triggered in response to a swept magnetic field applied along the easy (c-axis) of a single crystal of Mn_{12}-acetate . Avalanches were found to occur stochastically between 1.0 T and 4.5 T at temperatures below 0.82 K. No apparent dependence was found on temperature except that no avalanches were recorded above 0.82 K for the samples used in these studies. About half the avalanches occurred below the field (3.5 T) at which appreciable relaxation proceeds by ground state tunneling. There is evidence that the probability for the occurrence of an avalanche is reduced between ground-state tunneling resonant magnetic fields above 3.5 T. This suggests that above 3.5 T, the probability for triggering an avalanche is enhanced by relaxation through ground-state tunneling. Moreover, no avalanches were detected between 1.0 T and 1.5 T. The magnetization of the second species, present in all Mn_{12}-acetate samples, saturates around 1.5 T; the avalanches around 1.0 T may have been triggered by the relaxation of the second species (and are therefore not relevant to our investigations).

The main results of this thesis, contained in Section 3.3, were obtained by time-resolved measurements of the local magnetization using micron-size Hall bars. Avalanches were found to propagate with a constant velocity that depends on the magnetic field at which the avalanche is triggered. The speed of propagation is sur-

prisingly slow (about two orders of magnitude smaller than typical sound velocities in solids).

We have suggested that avalanches in the magnetization reversal of sufficiently large crystals of magnetic molecules are very similar to flame propagation (deflagration) through a metastable chemical substance. The analogy between the two systems derives from the field-induced metastability of magnetically bistable molecular nanomagnets. Our observation of magnetic deflagration offers a potentially important new way to investigate the phenomenon of flame propagation (and, possibly detonation). In contrast to deflagration in flammable chemical substances, the analogous process of magnetic deflagration in molecular nanomagnets is non-destructive, reversible, and much easier to control.

Below, we suggest future experiments that could expand and deepen our understanding of magnetic avalanches and magnetic deflagration.

Subsequent to our findings, Hernández-Mínguez, *et al.* reported the controlled ignition of magnetic avalanches by surface acoustic waves (SAWs) in Mn_{12}-acetate [156, 185, 186]. Obtained from analysis of measurements of the global (non-local) measurements of the magnetization, the speed of propagation was found to display maxima at the magnetic field corresponding to tunneling resonances. These authors attributed this to deflagration assisted by quantum tunneling: *quantum magnetic deflagration*. We did not observe such maxima at the tunneling resonances in our data, due perhaps to the fact that our method did not provide controlled ignition at closely spaced intervals of magnetic field. One of the easiest ways to determine whether the velocity of propagation is enhanced by tunneling resonances is by applying large transverse magnetic field to the sample during an avalanche. The large transverse magnetic field increases the tunneling rate. Therefore, the larger the transverse magnetic field is, the larger the velocity of propagation.

For further studies of the velocity of avalanche propagation, a more precise description of the evolution of avalanches in three dimensions can be obtained by using more accurate thermal boundary conditions. A measurement of the temperature dependence of thermal diffusivity would be useful in the calculation. Also, it is interesting to measure the local-time evolution of the temperature and compare it to magnetic measurements. To see the importance of the boundary conditions of the sample on thermal diffusion, the cooling environment and the materials of the surrounding can be changed.

Developing an external triggering method is also important. It would be good to have very local triggering so that the process of triggering and propagation would be distinguishable. Also, global heating should be avoided so that most of the heat comes from the sample itself. Heating by a focused laser is reccomended. It is also interesting to study how external heat can trigger avalanches. One should also be able to trigger avalanches by global heating. For example, at a fixed magnetic field, the bath temperature could be increased slowly (or faster) and at some point, avalanches would be triggered. Faster increases in temperature will be more likely to trigger avalanches.

For self-triggering studies, the effect of the presence of defects should be studied. Our preliminary results show avalanches are more likely to occur in samples with more defects. The defects work favorably for avalanches in two possible ways. One is that molecules with defects have larger symmetry breaking, therefore, smaller metastability. Relaxation of molecules with defects can be used as an ignition point, "hot spots", [170, 171]. The other reason is that large defects or high concentration of defects would make thermal diffusivity smaller. Therefore, heat is more easily trapped and would trigger an avalanche. Dependence on sample size and shape also can be studied.

Bibliography

[1] S. M. J. Aubin, M. W. Wemple, D. M. Adams, H.-L. Tsai, G. Christou, and D. N. Hendrickson, *J. Am. Chem. Soc.*, **118**, 7746–7754 (1996).

[2] G. Aromi, S. M. J. Aubin, M. A. Bolcar, G. Christou, H. J. Eppley, K. Folting, D. N. Hendrickson, J. C. Huffman, R. C. Squire, H. L. Tsai, S. Wang, and M. W. Wemple, *Polyhedron*, **17**, 3005–3020 (1998).

[3] T. Lis, *Acta Cryst. B*, **36**, 2042 (1980).

[4] A. Caneschi, D. Gatteschi, R. Sessoli, A.-L. Barra, L.-C. Brunel, and M. Guillot, *J. Am. Chem. Soc.*, **113**, 5873–5874 (1991).

[5] R. Sessoli, D. Gatteschi, A. Caneschi, and M. A. Novak, *Nature*, **365**, 141–143 (1993).

[6] R. Sessoli, H.-L.Tsai, A. R. Schake, S. Wang, J. B. Vincent, K. Folting, D. Gatteschi, G. Christou, and D. N. Hendrickson, *J. Am. Chem. Soc.*, **115**, 1804–1816 (1993).

[7] K. Wieghardt, K. Pohl, I. Jibril, and G. Huttner, *Angew. Chem. Int. Ed. Engl.*, **23**, 77–78 (1984).

[8] C. Sangregorio, T. Ohm, C. Paulsen, R. Sessoli, and D. Gatteschi, *Phys. Rev. Lett.*, **78**, 4645 (1997).

[9] B. J. Suh, D. Procissi, J. K. Jung, S. Bud'ko, W. S. Jeon, Y. J. Kim, and D.-Y. Jung, *J. Appl. Phys.*, **93**, 7098–7100 (2003).

[10] S. M. J. Aubin, N. R. Dilley, M. W. Wemple, M. B. Maple, G. Christou, and D. N. Hendrickson, *J. Am. Chem. Soc.*, **120**, 839 (1998).

[11] S. M. J. Aubin, N. R. Dilley, L. Pardi, J. Krzystek, M. W. Wemple, L.-C. Brunel, M. B. Maple, G. Christou, and D. N. Hendrickson, *J. Am. Chem. Soc.*, **120**, 4991–5004 (1998).

[12] K. H. Han, B. J. Kim, B. J. Suh, M. Belesi, D. Moon, K. Lee, and M. S. Lah, *J. Appl. Phys.*, **99**, 08J507 (2006).

[13] O. Waldmann, S. Carretta, P. Santini, R. Koch, A. G. M. Jansen, G. Amoretti, R. Caciuffo, L. Zhao, and L. K. Thompson, *Phys. Rev. Lett.*, **92**, 096403 (2004).

[14] O. Waldmann, L. Zhao, and L. K. Thompson, *Phys. Rev. Lett.*, **88**, 066401 (2002).

[15] T. Guidi, S. Carretta, P. Santini, E. Liviotti, N. Magnani, C. Mondelli, O. Waldmann, L. K. Thompson, L. Zhao, C. D. Frost, G. Amoretti, and R. Caciuffo, *Phys. Rev. B*, **69**, 104432 (2004).

[16] E. K. Brechin, C. Boskovic, W. Wernsdorfer, J. Yoo, A. Yamaguchi, E. C. Sañudo, T. R. Concolino, A. L. Rheingold, H. Ishimoto, D. N. Hendrickson, and G. Christou, *J. Am. Chem. Soc.*, **124**, 9710–9711 (2002).

[17] M. Soler, E. Rumberger, K. Folting, D. N. Hendrickson, and G. Christou, *Polyhedron*, **20**, 1365–1369 (2001).

[18] W. Wernsdorfer, N. Aliaga-Alcalde, D. N. Hendrickson, and G. Christou, *Nature*, **416**, 406–409 (2002).

[19] D. Gatteschi, L. Pardi, A.-L. Barra, A. Müller, and J. Döring, *Nature*, **354**, 463–465 (1991).

[20] I. Chiorescu, W. Wernsdorfer, A. Müller, H. Bögge, and B. Barbara, *Phys. Rev. Lett.*, **84**, 3454 (2000).

[21] J. R. Galan-Mascaros, J. R. Gomez-Garcia, J. J. Borras-Amernar, and E. Coronado, *Advanced Materials*, **6**, 221 (1994).

[22] R. S. Edwards, S. Maccagnano, E.-C. Yang, S. Hill, W. Wernsdorfer, D. Hendrickson, and G. Christou, *J. Appl. Phys.*, **93**, 7807 (2003).

[23] A. Wilson, J. Lawrence, E-C. Yang, M. Nakano, D. N. Hendrickson, and S. Hill, *Phys. Rev. B*, **74**, 140403 (2006).

[24] A. Müller, E. Krickemeyer, J. Meyer, H. Bögge, F. Peters, W. Plass, E. Diemann, S. Dillinger, F. Nonnenbruch, M. Randerath, and C. Menke, *Angew. Chem. Int. Ed. Engl.*, **34**, 2122–2124 (1995).

[25] A. Müller, E. Krickemeyer, H. Bögge, M. Schmidtmann, C. Beugholt, P. Kögerler, and C. Lu, *Angew. Chem. Int. Ed. Engl.*, **37**, 1220–1223 (1998).

[26] A. Müller, P. Kögerler, and A. W. M. Dress, *Coord. Chem. Rev.*, **222**, 193 (2001).

[27] A. Müller and S. Roy, *Russ. Chem. Rev.*, **71**, 981 (2002).

[28] W. Liu and H. H. Thorp, *Inorg. Chem.*, **32**, 4102 (1993).

[29] A. J. Tasiopoulos, A. Vinslava, W. Wernsdorfer, K. A. Abboud, and G. Christou, *Angew. Chem. Int. Ed.*, **43**, 2117–2121 (2004).

[30] A. J. Leggett, S. Chakravarty, A. T. Dorsey, M. P. A. Fisher, A. Garg, and W. Zwerger, *Rev. Mod. Phys.*, **59**, 1–85 (1987).

[31] E. M. Chudnovsky and L. Gunther, *Phys. Rev. Lett.*, **60**, 661–664 (1988).

[32] D. Gatteschi, A. Caneschi, L. Pardi, and R. Sessoli, *Science*, **265**, 1054–1058 (1994).

[33] B. Barbara, L. Thomas, F. Lionti, I. Chiorescu, and A. Sulpice, *J. Magn. Magn. Mater.*, **200**, 167–181 (1999).

[34] J. R. Friedman, M. P. Sarachik, J. Tejada, and R. Ziolo, *Phys. Rev. Lett.*, **76**, 3830–3833 (1996).

[35] L. Thomas, F. Lionti, R Ballou, D. Gatteschi, R. Sessoli, and B. Barbara, *Nature*, **383**, 145–147 (1996).

[36] J. M. Hernandez, X. X. Zhang, F. Luis, J. Tejada, J. R. Friedman, M. P. Sarachik, and R. Ziolo, *Phys. Rev. B*, **55**, 5858–5865 (1997).

[37] H. Andres, R. Basler, A. J. Blake, C. Cadiou, G. Chaboussant, C. M. Grant, H.-U. Gdel, M. Murrie, S. Parsons, C. Paulsen, F. Semadini, V. Villar, W. Wernsdorfer, and R. E. P. Winpenny, *Chem. Eur. J.*, **8**, 4867 (2002).

[38] W. Wernsdorfer and R. Sessoli, *Science*, **284**, 133–135 (1999).

[39] W. Wernsdorfer, I. Chiorescu, R. Sessoli, D. Gatteschi, and D. Mailly, *Physica B*, **284-288**, 1231–1232 (2000).

[40] A. O. Caldeira and A. J. Leggett, *Phys. Rev. Lett.*, **46**, 211–214 (1981).

[41] A. Garg and G.-H. Kim, *Phys. Rev. Lett.*, **63**, 2512–2515 (1989).

[42] A. Garg, *Phys. Rev. Lett.*, **70**, 1541–1544 (1993).

[43] J. Villain, F. Hartman-Boutron, R. Sessoli, and A. Rettori, *Europhys. Lett.*, **27**(2), 159–164 (1994).

[44] A. Garg, *Phys. Rev. B*, **51**, 15592–15595 (1995).

[45] P. Politi, A. Rettori, F. Hartmann-Boutron, and J. Villain, *Phys. Rev. Lett.*, **75**, 537–540 (1995).

[46] D. A. Garanin and E. M. Chudnovsky, *Phys. Rev. B*, **56**, 11102–11118 (1997).

[47] J. R. Friedman, M. P. Sarachik, and R. Ziolo, *Phys. Rev. B*, **58**(22), R14729–R14732 (1998).

[48] D. A. Garanin, E. M. Chudnovsky, and R. Schilling, *Phys. Rev. B*, **61**, 12204–12208 (2000).

[49] N. V. Prokof'ev and P. C. E. Stamp, *J. Low Temp. Phys.*, **104**, 143 (1996).

[50] N. V. Prokof'ev and P. C. E. Stamp, *Phys. Rev. Lett.*, **80**, 5794–5797 (1998).

[51] L. Gunther and B. Barbara, *Quantum Tunneling of Magnetization - QTM'94*, Kluwer, Dordrecht, Netherlands, 1995.

[52] E. M. Chudnovsky and J. Tejada, *Macroscopic Quantum Tunneling of the Magnetic Moments*, Cambridge University Press, 1998.

[53] D. Gatteschi and R. Sessoli, "Magnetic Properties of Large Clusters", in *Magnetism: Molecules to Materials III*, edited by J. S. Miller and M. Drillon, pages 63–108, Wiley, 2002.

[54] W. Wernsdorfer, *Classical and quantum magnetization reversal studied in nanometer-sized particles and clusters*, John Wiley & Sons, 2002.

[55] D. Gatteschi and R. Sessoli, *Angew. Chem. Int. Ed.*, **42**, 268–297 (2003).

[56] E. del Barco, A. D. Kent, S. Hill, J. M. North, N. S. Dalal, E. Rumberger, D. N. Hendrikson, N. Chakov, and G. Christou, *J. Low Temp. Phys*, **140**, 119 (2005).

[57] A. D. Kent, Y. Zhong, L. Bokacheva, D. Ruiz, D. N. Hendrickson, and M. P. Sarachik, *Europhys. Lett.*, **49**, 521 (2000).

[58] A. D. Kent, Y. Zhong, L. Bokacheva, D. Ruiz, D. N. Hendrickson, and M. P. Sarachik, *J. Appl. Phys.*, **87**, 5493 (2000).

[59] L. Bokacheva, A. D.Kent, and M. A. Walters, *Phys. Rev. Lett.*, **85**, 4803 (2000).

[60] K. M. Mertes, Y. Zhong, M. P. Sarachik, Y. Paltiel, H. Shtrikman, E. Zeldov, E. Rumberger, D. N. Hendrickson, and G. Christou, *Europhys. Lett.*, **55**, 874–879 (2001).

[61] A. A. Mukhin, V. D. Travkin, A. K. Zvezdin, A. Caneschi, D. Gatteschi, and R. Sessoli, *Physica B*, **284-288**, 1221 (2000).

[62] A. L. Barra, P. Debrunner, D. Gatteschi, Ch. E. Schulz, and R. Sessoli, *Europhys. Lett.*, **35**, 133 (1996).

[63] T. Ohm, C. Sangregorio, and C. Paulsen, *Eur. Phys. J. B*, **6**, 195 (1998).

[64] R. Caciuffo, G. Amoretti, A. Murani, R. Sessoli, A. Caneschi, and D. Gatteschi, *Phys. Rev. Lett.*, **81**, 4744 (1998).

[65] E. del Barco, N. Vernier, J. M. Hernandez, J. Tejada, E. M. Chudnovsky, E. Molins, and G. Bellessa, *Europhys. Lett.*, **47**, 722 (1999).

[66] W. Wernsdorfer, T. Ohm, C. Sangregorio, R. Sessoli, D. Mailly, and C. Paulsen, *Phys. Rev. Lett.*, **82**, 3903–3906 (1999).

[67] Yicheng Zhong, M. P. Sarachik, J. R. Friedman, R. A. Robinson, T. M. Kelley, H. Nakotte, A. C. Christianson, F. Trouw, S. M. J. Aubin, and D. N. Hendrickson, *J. Appl. Phys.*, **85**, 5636 (1999).

[68] M. Hennion, L. Pardi, I. Mirebeau, E. Suard, R. Sessoli, and A. Caneschi, *Phys. Rev. B*, **56**, 8819 (1997).

[69] I. Mirebeau, M. Hennion, H. Casalta, H. Andres, H. U. Gudel, A. V. Irodova, and A. Caneschi, *Phys. Rev. Lett.*, **83**, 628–631 (1999).

[70] G. Amoretti, R. Caciuffo, J. Combet, A. Murani, and A. Caneschi, *Phys. Rev. B*, **62**, 3022 (2000).

[71] R. Sessoli, *Mol. Cryst. Liq. Cryst.*, **274**, 145–157 (1995).

[72] A. L. Barra, A. Caneschi, D. Gatteschi, and R. Sessoli, *J. Am. Chem. Soc.*, **117**, 8855–8856 (1995).

[73] A. L. Barra, D. Gatteschi, and R. Sessoli, *Phys. Rev. B*, **56**(13), 8192–8198 (1997).

[74] S. Hill, J. A. A. J. Perenboom, N. S. Dalal, T. Hathaway, T. Stalcup, and J. S. Brooks, *Phys. Rev. Lett.*, **80**, 2453–2456 (1998).

[75] S. Hill, S. Maccagnano, Kyungwha Park, R. M. Achey, J. M. North, and N. S. Dalal, *Phys. Rev. B*, **65**, 224410 (2002).

[76] Y. Furukawa, K. Watanabe, K. Kumagai, Z. H. Jang, A. Lascialfari, F. Borsa, and D. Gatteschi, *Phys. Rev. B*, **62**, 14246 (2001).

[77] Y. Furukawa, K. Watanabe, K. Kumagai, F. Borsa, T. Sasaki, N. Kobayashi, and D. Gatteschi, *Phys. Rev. B*, **64**, 104401 (2001).

[78] Y. Furukawa, K. Kumagai, A. Lascialfari, S. Aldrovandi, F. Borsa, R. Sessoli, and D. Gatteschi, *Phys. Rev. B*, **64**, 094439 (2001).

[79] Y. Furukawa, K. Watanabe, K. Kumagai, F. Borsa, T. Sasaki, N. Kobayashi, and D. Gatteschi, *Phys. Rev. B*, **67**, 064426 (2003).

[80] A. Lascialfari, D. Gatteschi, F. Borsa, and A. Cornia, *Phys. Rev. B*, **55**, 14341 (1997).

[81] P. Santini, S. Carretta, E. Liviotti, G. Amoretti, P. Carretta, M. Filibian, A. Lascialfari, and E. Micotti, *Phys. Rev. Lett.*, **94**, 077203 (2005).

[82] T. Goto, T. Koshiba, T. Kubo, and K. Awaga, *Phys. Rev. B*, **67**, 104408 (2003).

[83] T. Kubo, T. Goto, T. Koshiba, K. Takeda, and K. Awaga, *Phys. Rev. B*, **65**, 224425 (2002).

[84] A. Lascialfari, F. Borsa, P. Carretta, Z. H. Jang, D. Gatteschi, L. Ninci, C. Sangregorio, J. Lord, and C. A. Scott, *Appl. Mag. Res.*, page 19 (2000).

[85] A. Lascialfari, P. Carretta, D. Gatteschi, C. Sangregorio, J. Lord, and C. A. Scott, *Physica B*, **110**, 289 (2000).

[86] P. Ghigna, A. Campana, A. Lascialfari, A. Caneschi, D. Gatteschi, A. Tagliaferri, and F. Borgatti, *Phys. Rev. B*, **64**, 132413 (2001).

[87] R. Moroni, Ch. Cartier dit Moulin, G. Champion, M.-A. Arrio, Ph. Sainctavit, M. Verdaguer, and D. Gatteschi, *Phys. Rev. B*, **68**, 064407 (2003).

[88] N. Domingo, B. E. Williamson, J. Gómez-Segura, Ph. Gerbier, D. Ruiz-Molina, D. B. Amabilino, J. Veciana, and J. Tejada, *Phys. Rev. B*, **69**, 052405 (2004).

[89] B. Parks, J. Loomis, E. Rumberger, D. N. Hendrickson, and G. Christou, *Phys. Rev. B*, **64**, 184426 (2001).

[90] A. B. Sushkov, B. R. Jones, J. L. Musfeldt, Y. J. Wang, R. M. Achey, and N. S. Dalal, *Phys. Rev. B*, **63**, 214408 (2001).

[91] S. M. Oppenheimer, A. B. Sushkov, J. L. Musfeldt, R. M. Achey, and N. S. Dalal, *Phys. Rev. B*, **65**, 054419 (2002).

[92] A. B. Sushkov, J. L. Musfeldt, Y. J. Wang, R. M. Achey, and N. S. Dalal, *Phys. Rev. B*, **66**, 144430 (2002).

[93] J. van Slageren, A. Mukhin, B. Gorshunov, and M. Dressel, *Phys. Rev. B*, **69**, 104410 (2004).

[94] J. van Slageren, S. Vongtragool, A. Mukhin, B. Gorshunov, and M. Dressel, *Phys. Rev. B*, **72**, 020401 (2005).

[95] A. A. Mukhin, V. D. Travkin, A. K. Zvezdin, S. P. Lebedev, A. Caneschi, and D. Gatteschi, *Europhys. Lett.*, **44**, 778 (1998).

[96] B. Barbara and E. M. Chudnovsky, *Phys. Rev. Lett.*, **A145**, 205 (1990).

[97] S. Miyashita, *J. Phys. Soc. Jpn.*, **64**, 3207–3214 (1995).

[98] V. V. Dobrovitski and A. K. Zvezdin, *Europhys. Lett.*, **38**, 377 (1997).

[99] L. Gunther, *Europhys. Lett.*, **39**, 1 (1997).

[100] G. Rose and P. C. E. Stamp, *J. Low Temp. Phys.*, **113**, 1153 (1998).

[101] S. Carretta, E. Liviotti, N. Magnani, P. Santini, and G. Amoretti, *Phys. Rev. Lett.*, **92**, 207205 (2004).

[102] S. E. Barnes, R. Ballou, B. Barbara, and J. Strelen, *Phys. Rev. Lett.*, **79**, 289 (1997).

[103] GwangHee Kim and Tae-Suk Kim, *Europhys. Lett.*, **92**, 137203 (2004).

[104] C. Calero, E. M. Chudnovsky, and D. A Garanin, *Phys. Rev. B*, **74**, 094428 (2006).

[105] M. R. Pederon and S. N. Khanna, *Phys. Rev. B*, **59**, R693–R696 (1999).

[106] M. R. Pederon and S. N. Khanna, *Phys. Rev. B*, **60**, 9566–9572 (1999).

[107] Kyungwha Park, M. A. Novotny, N. S. Dalal, S. Hill, and P. A. Rikvold, *Phys. Rev. B*, **65**(1), 014426 (2002).

[108] Julio F. Fernández and Juan J. Alonso, *Phys. Rev. Lett.*, **91**, 047202 (2003).

[109] Juan J. Alonso and Julio F. Fernández, *Phys. Rev. Lett.*, **87**, 097205 (2001).

[110] W. Wernsdorfer, N. E. Chakov, and G. Christou, *Phys. Rev. Lett.*, **95**, 037203 (2005).

[111] S. Hill, N. Anderson, A. Wilson, S. Takahashi, K. Petukhov, N. E. Chakov, M. Murugesu, J. M. North, E. del Barco, A. D. Kent, N. S. Dalal, and G. Christou, *Polyhedron*, **24**, 2284–2292 (2005).

[112] N. E. Chakov, S.-C. Lee, A. G. Harter, P. L. Kuhns, A. P. Reyes, S. O. Hill, N. S. Dalal, W. Wernsdorfer, K. A. Abboud, and G. Christou, *J. Am. Chem. Soc.*, **128**, 6975–6989 (2006).

[113] W. Wernsdorfer, M. Murugesu, and G. Christou, *Phys. Rev. Lett.*, **96**, 057208 (2006).

[114] M. Clemente-León, H. Soyer, E. Coronado, C. Mingotaud, C. J. Gómez-García, and P. Delhaès, *Angew. Chem. Int. Ed.*, **37**, 2842–2845 (1998).

[115] D. Ruiz-Molina, M. Mas-Torrent, J. Gomez, I. Balana, N. Domingo, J. Tejada, M. T. Martines, C. Rovira, and J. Veciana, *Adv. Mater.*, **15**, 42 (2003).

[116] A. Cornia, A. C. Fabretti, M. Pacchioni, L. Zobbi, D. Bonacchi, A. Caneschi, D. Gatteschi, R. Biagi, U. Del Pennino, V. De Renzi, L. Gurevich, and H. S. J. Van der Zant, *Angew. Chem. Int. Ed.*, **42**, 1645–1648 (2003).

[117] M. Cavallini, F. Biscarini, J. Gomez-Segura, D. Ruiz, and J. Vaciana, *Nano Lett.*, **3**, 1645 (2003).

[118] Soohyon Phark, Zheong G. Khim, Beom Jin Kim, Byoung Jin Suh, Seokwon Yoon, Jinkwon Kim, Jin Mook Lim, and Youngkyu Do, *Jpn. J. Appl. Phys.*, **43**, 8273 (2004).

[119] D. Deutsch, *Proc. Roy. Soc. A*, **400**, 97–117 (1985).

[120] M. N. Leuenberger and D. Loss, *Nature*, **410**, 789–793 (2001).

[121] L. Sorace, W. Wernsdorfer, C. Thirion, A.-L. Barra, M. Pacchioni, D. Mailly, and B. Barbara, *Phys. Rev. B*, **68**, 220407 (2003).

[122] M. Bal, Jonathan R. Friedman, Yoko Suzuki, K. M. Mertes, E. M. Rumberger, D. N. Hendrickson, Y. Myasoedov, H. Shtrikman, N. Avraham, and E. Zeldov, *Phys. Rev. B*, **70**, 100408(R) (2004).

[123] E. del Barco, A. D. Kent, E. C. Yang, and D. N. Hendrickson, *Phys. Rev. Lett.*, **93**, 157202 (2004).

[124] M. Bal, Jonathan R. Friedman, Y. Suzuki, E. M. Rumberger, D. N. Hendrickson, N. Avraham, Y. Myasoedov, H. Shtrikman, and E. Zeldov, *Europhys. Lett.*, **71**, 110 (2005).

[125] W. Wernsdorfer, A. Mller, D. Mailly, and B. Barbara, *Europhys. Lett.*, **66**, 861 (2004).

[126] C. Paulsen and J. G. Park, "Evidence for Quantum Tunneling of the Magnetization in $Mn_{12}Ac$", in *Quantum Tunneling of Magnetization - QTM'94*, edited by L. Gunther and B. Barbara, pages 189–207, Kluwer, Dordrecht, Netherlands, 1995.

[127] E. del Barco, J. M. Hernandez, M. Sales, J. Tejada, H. Rakoto, J. M. Broto, and E. M. Chudnovsky, *Phys. Rev. B*, **60**, 11 898 (1999).

[128] C. Paulsen, J. G. Park, B. Barbara, R. Sessoli, and A. Caneschi, *J. Magn. Magn. Mater.*, **140-144**, 379–380 (1995).

[129] M. A. Novak and R. Sessoli, in *Quantum Tunneling of Magnetization - QTM'94*, edited by L. Gunther and B. Barbara, pages 171–188, Kluwer, Dordrecht, Netherlands, 1995.

[130] A. Cornia, R. Sessoli, L Sorace, D Gatteschi, A. L. Barra, and C. Daiguebonne, *Phys. Rev. Lett.*, **89**, 257201 (2002).

[131] E. M. Chudnovsky and D. A. Garanin, *Phys. Rev. Lett.*, **87**, 187203 (2001).

[132] D. A. Garanin and E. M. Chudnovsky, *Phys. Rev. B*, **65**, 094423 (2002).

[133] K. M. Mertes, Yoko Suzuki, M. P. Sarachik, Y. Paltiel, H. Shtrikman, E. Zeldov, E. M. Rumberger, D. N. Hendrickson, and G. Christou, *Phys. Rev. Lett.*, **87**, 7205 (2001).

[134] E. del Barco, A. D. Kent, E. Rumberger, D. N. Hendrikson, and G. Christou, *Phys. Rev. Lett.*, **91**, 047203 (2003).

[135] S. Hill, R. S. Edwards, S. I. Jones, N. S. Dalal, and J. M. North, *Phys. Rev. Lett.*, **90**, 217204 (2003).

[136] L. D. Landau, *Phys. Z. Sowjetunion*, **2**, 46 (1932).

[137] C. Zener, *Proc. R. Soc. London A*, **137**, 696 (1932).

[138] E. C. G. Stueckelberg, *Helv. Phys. Acta*, **5**, 370–422 (1932).

[139] M. N. Leuenberger and D. Loss, *Phys. Rev. B*, **61**, 12200–12203 (2000).

[140] Jonathan R. Friedman, *Ph.D. Thesis, The City University of New York, New York, NY* (1996).

[141] W. Wernsdorfer, R. Sessoli, and D. Gatteschi, *Europhys. Lett.*, **47**, 254–259 (1999).

[142] F. Luis, J. Bartolomé, J. F. Fernández, J. Tejada, J. M. Hernández, X. X. Zhang, and R. Ziolo, *Phys. Rev. B*, **55**, 11448–11456 (1997).

[143] I. Chiorescu, R. Giraud, A. G. M. Jansen, A. Caneschi, and B. Barbara, *Phys. Rev. Lett.*, **85**(22), 4807–4810 (2000).

[144] J. A. A. J. Perenboom, J. S. Brooks, S. Hill, T. Hathaway, and N. S. Dalal, *Phys. Rev. B*, **58**, 330–338 (1998).

[145] E. M. Rumberger, E. del Barco, J. Lawrence, S. Hill, A. D. Kent, L. N. Zakharov, A. L. Rheingold, and D. N. Hendrickson, *Polyhedron*, **24**, 2557 (2005).

[146] S. M. J. Aubin, Ziming Sun, I. A. Guzei, A. L. Rheingold, G. Christou, and D. N. Hndrickson, *Chem. Commun.*, page 2239 (1997).

[147] Z. Sun, D. Ruiz, E. Rumberger, C. D. Incarvito, K. Folting, A. L. Rheingold, and G. Christou, *Inorg. Chem.*, **37**, 4758–4759 (1998).

[148] J. M. Hernández, X. X. Zhang, F. Luis, J. Bartoloné, J. Tejada, and R. Ziolo, *Europhys. Lett.*, **35**, 301–306 (1996).

[149] C. Paulsen, J.-G. Park, B. Barbara, R. Sessoli, and A. Caneschi, *J. Magn. Magn. Mater.*, **140-144**, 379–380 (1995).

[150] M. A. Novak, R. Sessoli, A. Caneschi, and D. Gatteschi, *J. Magn. Magn. Mater.*, **146**, 211–213 (1995).

[151] P. Bak and M. Paczuski, *Physics World*, **6-12**, 39–43 (1993).

[152] F. Fominaya, J. Villain, P. Gandit, J. Chaussy, and A. Caneschi, *Phys. Rev. Lett.*, **79**, 1126 (1997).

[153] E. M. Chudnovsky and D. A. Garanin, *Phys. Rev. Lett.*, **89**, 157201 (2002).

[154] J. Tejada, E. M. Chudnovsky, J. M. Hernandez, and R. Amigo, *Appl. Phys. Lett.*, **84**, 2373 (2004).

[155] M. Bal, Jonathan R. Friedman, K. Mertes, W. Chen, E. M. Rumberger, D. N. Hendrickson, N. Avraham, Y. Myasoedov, H. Shtrikman, and E. Zeldov, *Phys. Rev. B*, **70**, 140403(R) (2004).

[156] A. Hernández-Mínguez, A. Jordi, R. Amigó, A. García-Santiago, J. M. Hernandez, and J. Tejada, *Europhys. Lett.*, **69**, 270–276 (2005).

[157] R. H Dicke, *Phys. Rev.*, **93**, 99 (1954).

[158] M. Gross and S. Haroche, *Phys. Rep.*, **93**, 301 (1982).

[159] L. I. Men'shikov, *Sov. Physics - Uspekhi*, **42**, 109 (1999).

[160] Collin L. Joseph, Carlos Calero, and Eugene M. Chudnovsky, *Phys. Rev. B*, **70**, 174416 (2004).

[161] M. Jordi, A. Hernandez-Mínguez, J. M. Hernandez, J. Tejada, S. Stroobants, J. Vanacken, and V. V. Moshchalkov, *Europhys. Lett.*, **68**, 888–893 (2004).

[162] J. Vanacken, S. Stroobants, M. Malfait, V. V. Moshchalkov, M. Jordi, J. Tehada, R. Amigo, E. M. Chudnovsky, and D. A. Garanin, *Phys. Rev. B*, **70**, 220401 (2004).

[163] W. Wernsdorfer, *cond-mat/0405014* (2004).

[164] Yoko Suzuki, K. M. Mertes, J. J. Tu, M. P. Sarachik, L. Mihaly, G. L. Carr, N. Avraham, Y. Myasoedov, H. Shtrikman, E. Zeldov, E. M. Rumberger, H. Hendrickson, and G. Christou, *Bull. Am. Phys. Soc.*, **49**, 191 (2004).

[165] J. R. Friedman, *Phys. Rev. B*, **57**, 10 291 (1998).

[166] J. R. Friedman, M. P. Sarachik, J. M. Hernandez, X. X. Zhang, J. Tejada, and E. Molins, *J. Appl. Phys.*, **81**, 3978 (1997).

[167] L. Bokacheva, A. D. Kent, and M. A. Walters, *Polyhedron*, **20**, 1717 (2001).

[168] Per Bak, Chao Tang, and Kurt Wiesenfeld, *Phys. Rev. Lett.*, **59**, 381 (1987).

[169] P. Bak, K. Chen, and C. Tang, *Phys. Rev. A*, **147**, 297 (1990).

[170] F. P. Bowden and Y. D. Yoffe, *Initiation and Growth of Explosion in Liquids and Solids*, Cambridge University Press, London, 1952.

[171] M. A. Cook, *Science of High Explosives*, Reinhold Publishing Corporation, New York, 1958.

[172] M. M. Kuklja and A. B. Kunz, *J. Appl. Phys.*, **86**, 4428 (1999).

[173] Yoko Suzuki, M. P. Sarachik, E. M. Chudnovsky, S. McHugh, R. Gonzalez-Rubio, Nurit Avraham, Y. Myasoedov, H. Shtrikman, E. Zeldov, N. E. Chakov, and G. Christou, *Phys. Rev. Lett.*, **95**, 147201 (2005).

[174] Nurit Avraham, Ady Stern, Yoko Suzuki, K. M. Mertes, M. P. Sarachik, E. Zeldov, Myasoedov Y, H. Shtrikman, E. M. Rumberger, D. N. Hendrickson, N. E. Chakov, and G. Christou, *Phys. Rev. B*, **72**, 144428 (2005).

[175] F. Luis, J. Campo, J. Gómez, G. J. McIntyre, J. Luzón, and D. Ruiz-Molina, *Phys. Rev. Lett.*, **95**, 227202 (2005).

[176] Julio F. Fernández and Juan J. Alonso, *Phys. Rev. Lett.*, **73**, 024412 (2006).

[177] L. D. Landau and E. M. Lifshitz, *Fluid Dynamics*, Pergamon, 1987.

[178] M. A. Novak, A. M. Gomes, and R. E. Rapp, *J. Appl. Phys.*, **83**, 6943 (1998).

[179] A. M. Gomes, M. A. Novak, R. Sessoli, A. Caneschi, and D. Gatteschi, *Phys. Rev. B*, **57**, 5021 (1998).

[180] F. Fominaya, J. Villain, T. Fournier, P. Gandit, J. Chaussy, A. Fort, and A. Caneschi, *Phys. Rev. B*, **59**, 519 (1999).

[181] A. M. Gomes, M. A. Novak, W. C. Nunes, and R. E. Rapp, *J. Magn. Magn. Mater.*, **226-230**, 2015 (2001).

[182] Y. Duan, *Chem. Phys.*, **238**, 407 (1998).

[183] K. Petukhov, S. Hill, N. E. Chakov, K. A. Abboud, and G. Christou, *Phys. Rev. B*, **70**, 054426 (2004).

[184] I. Glassman, *Combustion*, Academic Press, New York, 1996.

[185] J. M. Hernandez, P. V. Santos, F. Macià, A. García-Santiago, and J. Tejada, *Appl. Phys. Lett.*, **88**, 012503 (2006).

[186] A. Hernández-Mínguez, F. Macià, J. M. Hernansez, J. Tejada, and P. V. Santos, *cond-mat/0609429* (2006).

[187] C. H. Webster, O. Kazakova, A. Ya. Tzalenchuk, J. C. Gallop, P. W. Josephs-Franks, and A. Hernández-Mínguez, *cond-mat/0609586* (2006).

[188] Yoko Suzuki, S. McHugh, R. Gonzalez-Rubio, D. Graybill, M. P. Sarachik, N. Avraham, Y. Myasoedov, H. Shtrikman, E. Zeldov, E. M. Rumberger, H. Hendrickson, N. E. Chakov, and G. Christou, *Bull. Am. Phys. Soc.*, **50**, 1304 (2005).

[189] K. M. Mertes, *Ph.D. Thesis, The City University of New York, New York, NY* (2002).

[190] A. M. Chang, H. D. Hallen, L. Harriott, H. F. Hess, H. L. Kao, J. Kwo, R. E. Miller, R. Wolfe, J. van der Ziel, and T. Y. Chang, *Appl. Phys. Lett.*, **61**, 1974 (1992).

[191] D. Majer, E. Zeldov, H. Shtrikman, and M. Konczykowski, in *World Scientific*, edited by G. Deutscher and A. Revcolevschi, pages 271–296, World Scientific, Singapore, 1996.

[192] J. W. Guikema, *Ph.D. Thesis, Stanford University, Stanford, CA* (2004).

[193] D. Majer, *Ph.D. Thesis, The Weizmann Institute of Science, Rehovot, Islael* (1997).

[194] Nurit Avraham, *M.Sc. Thesis, The Weizmann Institute of Science, Rehovot, Islael* (2000).

[195] M. Ueda, S. Maegawa, H. Miyasaka, and S. Kitagawa, *J. Phys. Soc. Jpn.*, **70**, 3084 (2001).

[196] P. Horowitz and W. Hill, *The Art of Electronics*, Cambridge university Press, 1980.